CHARACTERIZATION OF A NICKEL-BASE SUPERALLOY THROUGH ELECTRICAL RESISTIVITY—MICROSTRUCTURE RELATIONSHIPS FACILITATED BY SMALL ANGLE SCATTERING

A Thesis
Presented to
The Academic Faculty

by

Ricky L. Whelchel

In Partial Fulfillment
of the Requirements for the Degree
Master of Science in the
School of Materials Science and Engineering

Georgia Institute of Technology
August 2011

CHARACTERIZATION OF A NICKEL-BASE SUPERALLOY THROUGH ELECTRICAL RESISTIVITY—MICROSTRUCTURE RELATIONSHIPS FACILITATED BY SMALL ANGLE SCATTERING

Approved by:

Dr. Rosario A. Gerhardt, Advisor
School of Materials Science and Engineering
Georgia Institute of Technology

Dr. Arun M. Gokhale
School of Materials Science and Engineering
Georgia Institute of Technology

Dr. Richard W. Neu
School of Mechanical Engineering
Georgia Institute of Technology

Date Approved: 3 June 2011

ACKNOWLEDGEMENTS

I would like to acknowledge my thesis advisor Dr. Rosario A. Gerhardt for her guidance and support throughout my tenure on this project. I also wish to thank Dr. V. Siva Kumar G. Kelekanjeri, whose PhD work was invaluable towards my own continued work on this project. Dr. Kelekanjeri is also acknowledged for the SEM and EDS data for samples given cumulative heat treatments.

I wish to acknowledge the primary source of funding for this research provided by the U.S. Department of Energy under grant number DE-FG 02-03-ER 46035, awarded to Professor Gerhardt. Portions of this project were also funded by a President's Undergraduate Research Award (PURA) provided by the Georgia Institute of Technology while I was an undergraduate student. Use of both the Advanced Photon Source at Argonne National Laboratory and the High Flux Isotope Reactor at Oak Ridge National Laboratory are also greatly appreciated. Use of the Advanced Photon Source was supported by the U.S. Department of Energy, Office of Science, Office of Basic Energy Sciences, under Contract No. DE-AC02-06CH11357. The High Flux Isotope Reactor was sponsored by the Scientific User Facilities Division, Office of Basic Energy Sciences, U.S. Department of Energy.

Small angle scattering data formed a significant portion of this thesis, and I wish to acknowledge the efforts of Dr. Jan Ilavsky and Dr. Ken Littrell for their help in both obtaining the data and in the later data analysis. I am very appreciative of my committee members–Dr.'s Gokhale and Neu for their commitments to serve. Finally I wish to thank my group members, friends, and family for their support.

TABLE OF CONTENTS

LIST OF TABLES

LIST OF FIGURES

SUMMARY

Gas turbine engine components are manufactured from nickel-base superalloys, such as Waspaloy, that obtain their superior high temperature mechanical properties through the formation of the γ' precipitate phase within the γ matrix phase via heat treatment. The γ' precipitate microstructure can evolve with both processing and high temperature exposure in the gas turbine engine, resulting in evolving mechanical properties. In order to assess this change in mechanical properties, it is desirable to develop non-destructive testing methods for characterizing the evolution in the underlying precipitate microstructure due to heat treatment. This project focuses on the use of electrical resistivity measurements as such a non-destructive testing method for detection of the evolution of the γ' precipitate phase size and distribution in Waspaloy. In order to relate the evolving volume distribution of precipitates to the electrical response, volumetric small angle scattering (SAS) measurements such as small angle neutron scattering (SANS) and ultra small angle X-ray scattering (USAXS) measurements were both performed. Standard microscopy techniques and X-ray diffraction were also performed to complement these measurements.

In order to assess which type of radiation (X-rays versus neutrons) was best for these specimens, a comparative study between SANS and USAXS was performed for similarly heat treated specimens. It was found that the USAXS measurements were more sensitive to a secondary precipitate size population that formed due to cyclic heat treatment. For cases where non-cyclic heat treatment was used, SANS measurements were more accurate. SANS samples can be of much greater thickness than the USAXS specimens, allowing for more statistically significant results; however, USAXS measurements can give lower measureable scattering angles, resulting in the detection of larger precipitates. In order to assess the effects of quenching samples from room temperature, an in-situ SANS measurement was performed at 725°C. This data was compared to SANS measurements on specimens given

ex-situ heat treatment at the same temperature. These studies showed a similar microstructural response whether the data was taken from in-situ or ex-situ specimens.

The electrical resistivity due to γ' precipitation involved the fast increase to a peak, due to the initial nucleation of the finely-spaced precipitates. As the precipitates increase in size and spacing, conduction electron scattering from precipitates is expected to become less frequent. This resulted in a slower decrease after the initial peak. This decreasing region is also due to removal of precipitate forming solute, as the precipitate volume fraction increases. Once the equilibrium volume fraction of γ' was reached, the resistivity reached a minimum value and formed a plateau with increasing aging time. This plateau occurred at similar aging times to the maximum in hardness. For the case of cyclically heat treated specimens, a fluctuating behavior was noted in the resistivity due to the presence of a smaller, secondary precipitate size population fluctuating in and out of solution in the matrix.

The initial resistivity maximum was fit with a Johnson-Mehl-Avrami (JMA) type equation for Waspaloy specimens heat treated at 600, 625, and 650°C. The fitted model showed an excellent agreement with the measured electrical response, implying that this model is valid for describing the initial nucleation of γ' in Waspaloy. The evolution of the rate constants with temperature revealed an activation energy of 398 kJ/mol. The resistivity maximum can be attributed to the initial volume fraction of the nucleated precipitates, whereby the volume fraction and resistivity both increased similarly with aging time.

For aging times past the initial peak in resistivity, the JMA model fails to capture the electrical response. For this regime, where growth and coarsening were the dominant precipitation mechanisms, a microstructural model designated as η' was created. This model accounts for conduction electron scattering from both precipitates and solute atoms, such that the electrical response due to precipitation can be modeled for a wide range of aging times. This model effectively fits a volume distribution of precipitates to the measured electrical response. Excellent fits to the electrical resistivity were obtained using this η' model, implying that it is valid for predicting the electrical response due to the γ' precipitate population during the growth and coarsening stages. If the effects of dislocations on the

electrical response were added to this model, then it might be possible to use electrical resistivity testing to monitor the evolution of the γ' precipitate distribution for in-service gas turbine engine components, which could lead to better lifetime prediction.

CHAPTER 1

INTRODUCTION

Nickel-base superalloys are an important material used primarily in the hot sections of both land and air-based gas turbine engines. Nickel-base superalloys have excellent high temperature strength, creep resistance, and corrosion resistance, allowing them to withstand the extreme temperature and corrosive environment within the gas turbine engine for long periods of time. The enhanced mechanical properties of gas turbine engine components manufactured from nickel-base superalloys are induced primarily through the formation of precipitate phases within the nickel-rich γ matrix phase. The material of interest for this project is Waspaloy - a polycrystalline nickel-base superalloy used in disc rotors. In Waspaloy, the precipitate phase is designated as γ' and has the chemical formula Ni_3(Al, Ti).

The formation of γ' via heat treatment strengthens the material by impeding dislocation motion; however, the strengthening ability of the precipitate phase is highly dependent on the induced microstructure. The precipitate size, spacing, volume fraction, and distribution all have significant effects on the mechanical properties of superalloys [1]. During service, gas turbine engine components are exposed to high temperatures that can enable further microstructural evolution of the previously induced precipitate phases. This evolution in the precipitate microstructure would result in a corresponding evolution in the mechanical properties of the component. It is also to be expected that the components will have a degree of variability during the initial processing stages. In order to track the mechanical properties of gas turbine engine components during service and to test for the degree of variability in the initial component microstructure, it would be desirable to develop a non-destructive testing methodology to monitor the precipitate phases in nickel-base superalloys.

Electrical resistivity testing is one method by which the precipitation process may be monitored in nickel-base superalloys [2–11]. Electrical resistivity is sensitive to crystal defects (such as dislocations, point defects, and precipitates), as well as the solute content in

metallic alloys [12]. The electrical response is thus affected by the increase in conduction electron scattering caused by the formation of the precipitate phase and also by the decrease in conduction electron scattering caused by the removal of precipitate forming solute from the matrix phase. Electrical resistivity measurements are thus sensitive to the initial nucleation of the precipitate phase, as well as their eventual growth and coarsening. If the electrical response due to precipitation is coupled with the evolution in the precipitate microstructure, then electrical resistivity testing could be used as a metric for both the evolving microstructure and the mechanical properties.

Small angle scattering (SAS) is one method by which the precipitate microstructure may be quantified in nickel-base superalloys [7, 9–11, 13–27]. SAS is an ideal characterization method, since the measurements are taken throughout the sample volume - yielding statistically significant results [28]. SAS is especially useful for deriving volume distributions of the nanometer-scale precipitates. Calculating particle size distributions for such small precipitates via traditional microscopy methods requires extensive sample preparation and is subject to large errors.

1.1 Objectives of the Thesis

In this project, electrical resistivity measurements were used to non-destructively track the changes in the γ' precipitate phase in Waspaloy due to heat treatment. The microstructure was obtained through volumetric ultra small angle X-ray scattering (USAXS) and small angle neutron scattering (SANS) measurements. Of particular interest were the effects of precipitate size, spacing, volume fraction, and distribution on the electrical response, as these are the key microstructural features that affect the mechanical properties in superalloys [1]. Standard microscopy and X-ray diffraction (XRD) experiments were performed to provide supporting evidence for the evolving precipitate microstructure. A microstructural model for the electrical response due to precipitation is proposed. It is believed that some form of this microstructural model could be used to track the evolution in the precipitate microstructure in superalloys, and thus give a metric for the evolving mechanical properties of gas turbine engine components due to thermal exposure.

A brief introduction to the following chapters will be given here. Chapter 2 will present the background on precipitation hardening, superalloys, and characterization of superalloys using electrical resistivity and small angle scattering. The experimental procedure will be given by Chapter 3. The next chapter (Chapter 4) will discuss the differences between USAXS and SANS measurements for heat treated Waspaloy samples, showing that certain radiation and instrument types are better suited to certain heat treatment conditions. Chapter 5 will also discuss the proper use of small angle scattering (SAS) measurements through analyzing the differences between in-situ and ex-situ heat treatment on the SAS data. After these two preliminary chapters, Chapter 6 will give an overview of the mechanical and electrical properties of Waspaloy as they evolve with heat treatment. The subsequent chapters will focus on quantifying the electrical response shown in Chapter 6 to the Waspaloy microstructure. Chapter 7 will present a model for the electrical resistivity in the nucleation regime, which uses a JMA type model. Chapters 8 and 9 will present a model for the electrical resistivity in the growth and coarsening stages, where the effects of matrix solute content will play an important role in the resulting model. The final model (to be presented in Chapter 9) has the ability to model a distribution of precipitates to the measured electrical response.

CHAPTER 2

BACKGROUND

2.1 Precipitation Hardenable Alloys

Precipitation hardenable alloys, such as nickel-base superalloys, are two phase materials, with a precipitate phase formed within the solute rich matrix phase via heat treatment. These heat treatments are shown schematically by Figure 1. The left side of Figure 1 is a hypothetical phase diagram in terms of temperature and composition of solute for a precipitation hardenable system. At temperatures above the solvus, only a single matrix phase is stable. The matrix is denoted as γ for nickel-base superalloys. At temperatures below the solvus, the precipitate phase (denoted as γ' for superalloys) is also stable. The heat treatments necessary to form the precipitate phase within the matrix phase are thus schematically shown by the right side of Figure 1 in terms of temperature versus time. The material is first heat treated to a temperature above the solvus followed by a rapid quench to room temperature. This forms a single matrix phase with all elements in solution and is known as the solution treatment. The material is then heat treated to temperatures below the solvus (followed again by quenching) to form the precipitate phase within the matrix. This is known as the aging treatment. By varying the time and temperature of the aging treatment, the kinetics of the precipitation reaction as well as the volume fraction of precipitates can be changed [1].

In precipitation hardened alloys, the precipitates increase the strength or hardness of the material by inhibiting dislocation motion. The trends in the strength or hardness of such materials is shown schematically by Figure 2. The initially nucleated precipitate microstructure is finely spaced, requiring dislocations to shear through the precipitates to move throughout the material. The stress required to shear the precipitates resists such dislocation motion. As the precipitate volume fraction increases, this resistance to shearing also increases. As the precipitate phase evolves with growth and coarsening, the size and

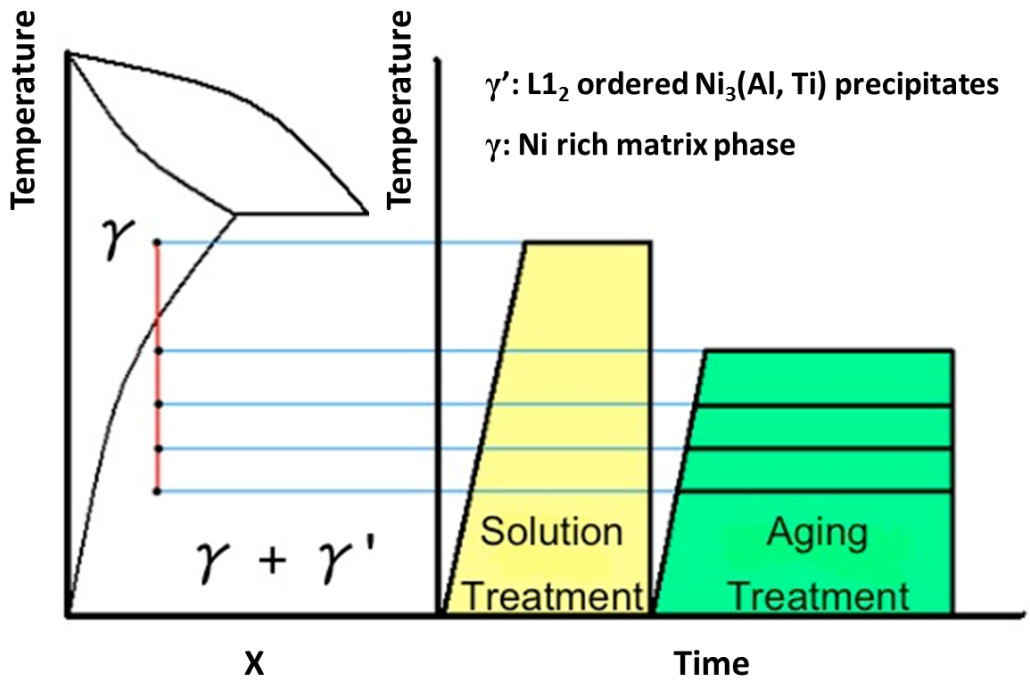

Figure 1: Schematic phase diagram and heating schedule for precipitation hardening systems. For nickel-base superalloys the matrix and precipitate phases are known as γ and γ' respectively.

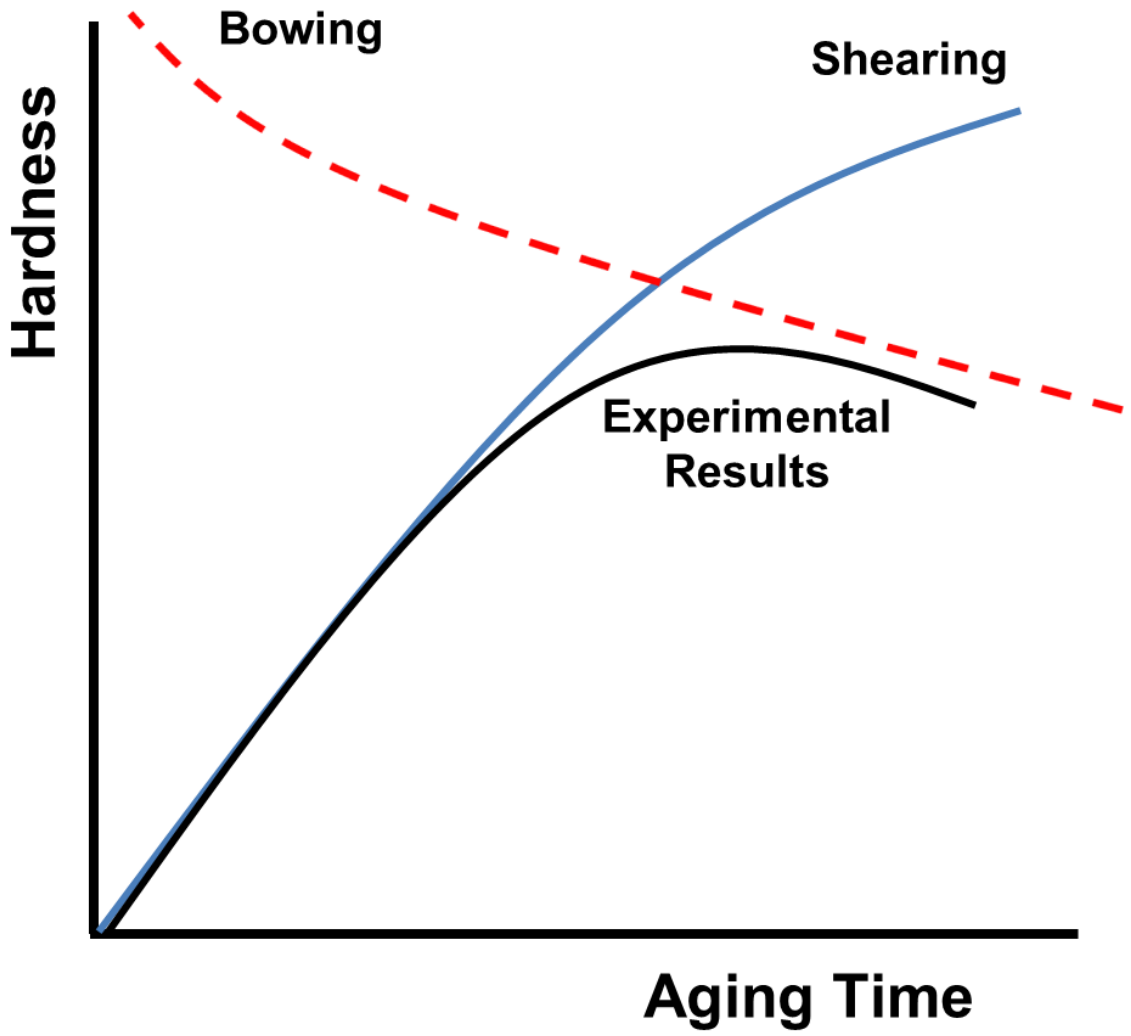

Figure 2: Schematic of the ideal precipitation hardening behavior due to precipitate shearing and bowing by dislocations

spacing of the precipitates also increases. Eventually the precipitates become so widely spaced that dislocations may bow around the precipitates, rather than shearing through them. This process is known as Orowan bowing, and results in a decreased resistance to dislocation motion as precipitate spacing increases [1]. The competing mechanisms of shearing and Orowan bowing result in a peaked behavior for the strength or hardness of precipitation hardened materials, whereby aging times after the peak in hardness are known as the over-aged regime.

2.2 Microstructural Evolution in Superalloys

2.2.1 Overview of Superalloy Microstructure

Gas turbine engine components have demanding mechanical property requirements, where high strength (or hardness), corrosion resistance, and creep resistance must be maintained at temperatures greater than 60% of the alloy melting point [1]. The creep resistance of nickel-base superalloys is induced by engineering of the matrix grains. For the turbine blades, creep resistance is of such paramount importance that either directionally solidified grains or single crystals are used. Creep resistance is not as important for the disc rotor materials such as Waspaloy. For these materials, the competing requirements of high strength (resultant from small grains) and creep resistance (resultant from large grains) must both be accounted for. Due to these two competing requirements, grains sizes between 30μm and 50μm are chosen for industrial polycrystalline nickel-base superalloy components [1]. For this project, polycrystalline Waspaloy samples were used, with all samples given a common solution treatment. It has been shown that this solution treatment yields grain sizes of approximately 85μm for these Waspaloy specimens [5, 7].

To further increase the creep resistance of polycrystalline superalloys, carbide phases are often produced at the grain boundaries [1]. These phases act to pin the grain boundaries, increasing the material resistance to grain boundary motion at high temperature. While some degree of carbide formation is expected in Waspaloy, these phases were not a subject of the present electrical resistivity studies. Since all specimens were given a common solution treatment, the extent of carbide formation should be constant and unchanging for the heat treatment conditions used in this project. In addition, these carbides have sizes on the order of microns, making their contribution to the electrical response negligible compared to the nanometer scale microstructural objects in the Waspaloy microstructure [7].

The primary source of strengthening in nickel-base superalloys is due to the formation of ordered precipitate phases within the FCC matrix phase via heat treatment. In Waspaloy these precipitates are known as γ' and have the ordered $L1_2$ crystal structure. Ideally these precipitates have a Ni_3(Al, Ti) chemical formula; however, in reality all alloying elements in superalloys partition into the precipitate and matrix phases [29, 30]. The γ' precipitates

greatly increase the strength or hardness of superalloys by inhibiting dislocation motion as described in Section 2.1. Since the precipitates are ordered in nickel-base superalloys, the sheared precipitates create high energy anti-phase boundaries (APB's) with the matrix phase [1]. The stress required to form these high energy APB's further resists dislocation shearing.

The relationships between the strength or hardness of superalloys and the precipitate microstructure are well known. The most relevant microstructural parameters that affect the mechanical properties of a given superalloy are the precipitate size, volume fraction, and mean free path [1]; therefore, these are the parameters of interest when non-destructively characterizing the γ' phase in Waspaloy. The relationships between the precipitate microstructure and the mechanical properties are not the primary focus of this project; however, hardness data is presented in some instances, and Appendix A discusses a method of quantifying the hardness in the over-aged regime.

2.2.2 Evolution in Precipitate Volume Fraction (JMA Model)

The increase in the precipitate volume fraction (f_V) to that of the equilibrium volume fraction ($f_{V,eq}$) is characterized by an "S" shaped behavior with the aging time [31]. This behavior is shown schematically by Figure 3. During the nucleation stage, the precipitate volume fraction increases very little. This is followed by the growth stage, whereby the volume fraction increases at a much higher rate. This continues until the precipitates begin to impinge on each other, thus slowing down the precipitation reaction until $f_{V,eq}$ is reached. For a precipitation reaction this impingement is not true "hard impingement", whereby the precipitates physically come in contact with one another. Instead, the diffusion fields from nearby precipitates overlap, resulting in competition for precipitate forming solute in the matrix. As the matrix becomes depleted of solute, this slows down the reaction, resulting in "soft impingement" [31].

The evolution in the precipitate volume fraction with time (t) has been quantified through the work of Johnson and Mehl [32] and Avrami [33], whereby the increase is expected to obey a form given by equation 1. In equation 1, the variables k and n are

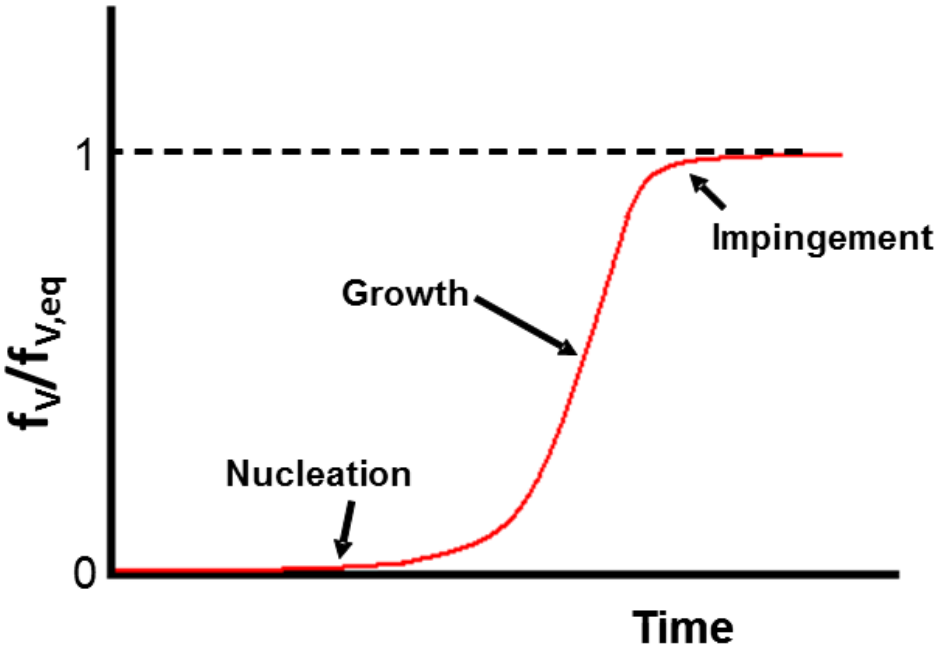

Figure 3: Schematic behavior of the evolution in the precipitate volume fraction with aging time. This behavior can be modeled with a Johnson-Mehl-Avrami type equation.

constants that depend on the temperature at which the reaction is taking place.

$$\frac{f_V}{f_{V,eq}} = 1 - exp\left[-(kt)^n\right] \tag{1}$$

2.2.3 Evolution in Precipitate Size and Spacing (Growth and Coarsening)

Diffusion controlled growth and coarsening are characterized by $t^{1/2}$ and $t^{1/3}$ rate laws respectively for the increase in the precipitate radius (r) [31]. During both processes the precipitates increase in size dramatically compared to the initially nucleated phase. During coarsening, the precipitate mean free path also increases due to the preferential removal of the smallest precipitates. By removing the smallest precipitates, the surface area of the precipitate phase is reduced, allowing for the total energy of the system to decrease [31].

The most widely used coarsening theory for particles undergoing diffusion controlled coarsening is that derived by Lifshitz and Slyozov [34] and Wagner [35]. This theory is referred to as LSW theory, and it is given by equation 2. The variables D, γ, V_m, and C_e are the diffusion coefficient for the particle forming solute, interfacial energy, molar

volume of particles, and the matrix solute concentration that is in equilibrium with the particles respectively. The variables R and T take their normal meanings as the universal gas constant and the absolute temperature, and k and t are the coarsening rate constant and time respectively. Equation 2 displays the expected $t^{1/3}$ behavior for diffusion controlled coarsening, with the rate constant k considered to be constant.

$$r^3 - r_0^3 = kt = \left(\frac{8D\gamma V_m^2 C_e}{9RT}\right) t \tag{2}$$

The coarsening of γ' has been modeled with the LSW model to some success [36]. Ardell and Nicholson [36] showed an excellent agreement with the LSW theory for γ' coarsening in Ni-Al alloys. This was somewhat surprising to the authors, as the γ' system is not an ideal LSW coarsening system. The derivation of LSW theory relies on the following assumptions: the particles are spherical, the volume fraction of particles is near zero, and the particle-matrix coherency strain is negligible [34, 35]. All three of these assumptions are not satisfied in superalloy specimens. Precipitates in superalloys display a variety of morphologies other than spheroids [37], can have very large volume fractions [1], and can also have large lattice mismatches [38, 39]. In fact, Rastogi and Ardell [40] observed a deviation from the LSW theory for γ' coarsening in a Ni-Si alloy, due to a loss of coherency with the matrix. It has also been shown that an effective diffusivity (D_{eff}) should be used in equation 2 due to the various constraints on the γ' precipitates [41].

The requirement of spherical particles is not as important as the other two, since it has been shown that the half edge length can replace the radius for diffusion controlled coarsening of cuboidal particles in superalloys [26, 42–45]. The effects of the precipitate volume fraction and the interfacial strain are not negligible on the coarsening behavior and have been the subject of extensive studies [46, 47]. All of these studies continue to show the expected $t^{1/3}$ behavior for the radius; however, the coarsening rate constant is different than that described by LSW theory, with the value often varying during the coarsening process itself.

The effects of volume fraction on coarsening were described by Ardell [48], whereby an increased volume fraction increases the probability of both hard impingement and soft

impingement from nearby precipitates. This in turn causes the coarsening rate constant to increase as the volume fraction of particles increases. Further studies on the effects of a finite volume fraction on particle coarsening have been performed by Voorhees and Glicksman [49, 50], whereby every particle is assumed to behave as a finite source or sink for solute atoms. Through computer simulation studies, the authors were also able to calculate an increasing rate constant with volume fraction of particles. In addition to the effects of volume fraction, Thornton et al. [51, 52] have modeled the effects of strain on the coarsening behavior. Through computer modeling, it was shown that the rate constant increased with interfacial strain, similarly to the volume fraction [51, 52]. There exist many theories designed to describe the coarsening behavior of non-ideal systems; however, there is no real agreement between the theories, and there does not exist a single theory which accurately describes coarsening for all systems [46, 47].

2.3 Electrical Resistivity

2.3.1 Role of Microstructure on Resistivity

Electrical resistivity has shown sensitivity to the precipitation process for several metallic alloys [2–11, 53–70]. Due to Matthiessen's rule, increases in a metallic alloy's solute content or defect density result in corresponding resistivity increases due to an increase in conduction electron scattering from these objects [12]. The density of defects within the superalloy microstructure (such as vacancies, dislocations, and the precipitates themselves) can evolve with processing or service within the gas turbine engine, making the effects of these defects on the resistivity important to quantify. In addition, the solute content of the matrix phase will vary as the precipitate volume fraction changes, making the composition of the matrix important to quantify as well.

The reason for the resistivity changes due to these microstructural influences may be explained through the use of the conductivity (σ) equation, given by equation 3, where the conductivity is the inverse of the resistivity. Both the charge and mass of an electron (e and m_e respectively) are constants, and the density of electrons (n) is also constant for metals. Therefore, changes to the resistivity in superalloys are controlled by changes to

the mean time between conduction electron collisions (τ). The time between collisions is in turn controlled by the conduction electron mean free path, which will change as the solute content and defect density evolve.

$$\sigma = \left(\frac{e^2}{m_e}\right) n\tau \tag{3}$$

During precipitation, the initial nucleation of the fine precipitate phase results in a fast resistivity increase to a maximum. This maximum can be attributed to the decreased conduction electron mean free path associated with forming these scattering centers within the matrix phase [53–57]. As the precipitates undergo growth and coarsening, the initial fine precipitate phase evolves into a more widely-spaced phase. Conduction electrons are thus more likely to collide with solute atoms than the coarse precipitates. After the maximum, the resistivity thus begins to decrease due to the growth and coarsening of the precipitates and also due to the changes to the solute content from the increasing precipitate volume fraction. Finally, dislocations have been shown to play a role in the electrical response due to precipitation [56]. Large interfacial stresses or deformation from mechanical loading will result in an increased dislocation density, and thus an increase in the electrical resistivity.

2.3.2 Classic Resistivity Experiments

The electrical response due to precipitation was first measured for much simpler alloys than nickel-base superalloys. These initial studies involved Al alloys [53, 54, 59], Cu alloys [55], and Fe alloys [56, 57]. The conclusions from all of these studies are summarized below:

1. The quenching temperature determined the rate at which the initial resistivity maximum was reached. A higher quench temperature implies a larger vacancy concentration upon quenching, which in turn resulted in faster diffusion. The vacancy concentration did not affect the value of the resistivity maximum. For a constant aging temperature (while varying the quenching temperature), the value of the resistivity maximum remained constant [53].

2. The aging temperature determined both the rate to reach the maximum and the value of the resistivity maximum. The rate first increased with increasing temperature then

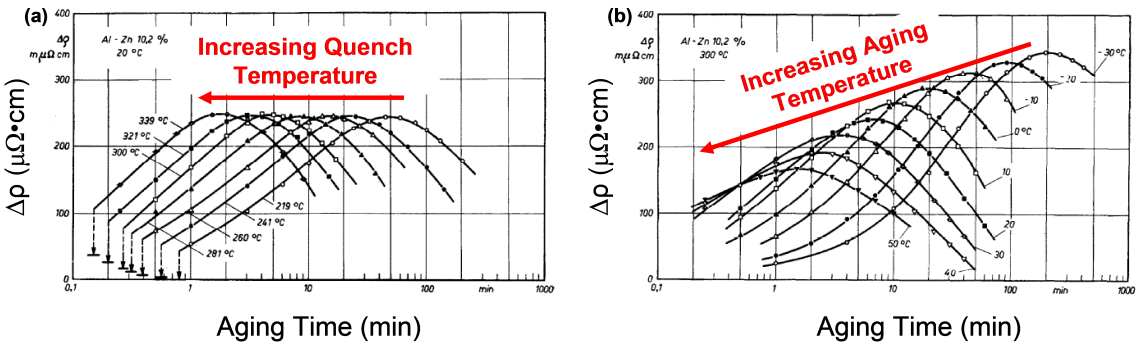

Figure 4: Change in electrical resistivity due to GP zone formation in an Al-Zn alloy, as presented by Panseri and Federighi [53]. The specimens were heat treated using (a) a constant aging temperature with varying quench temperatures and (b) a constant quench temperature with varying aging temperatures. The axis labels and arrows indicating the trends with temperature have been added for easier viewing.

decreased after a certain temperature was reached [56]. This is a C-curve type response that would be expected for a precipitation reaction. The value of the resistivity maximum increased with decreasing temperature in all cases, due to the increasing precipitate volume fraction at lower temperature [53–57, 59]. It was determined that the precipitates had sizes of approximately 1 nm at the resistivity maximum, regardless of the aging temperature [54, 56, 57].

3. In some cases, prolonged aging resulted in large interfacial strains. These strains, and their associated increase in dislocation density, gave rise to resistivity increases well after the initial maximum [56].

The most in depth studies on the effects of precipitation on the electrical response were performed by Panseri and Federighi [53] for Guinier-Preston (GP) zone formation in an Al-Zn alloy. The electrical resistivity results for these studies are given in Figure 4. These experiments were initially meant to ascertain the effects of vacancy concentration on the electrical response, as the authors believed that point defects would be the most relevant defect type affecting the resistivity maximum. As conclusion 1 above states, this was not the case for their experiments. Instead, as Figure 4(a) shows, the vacancy concentration only affects the initial formation kinetics of the resistivity maximum. The value of the maximum was controlled entirely by the aging temperature, as seen in Figure 4(b).

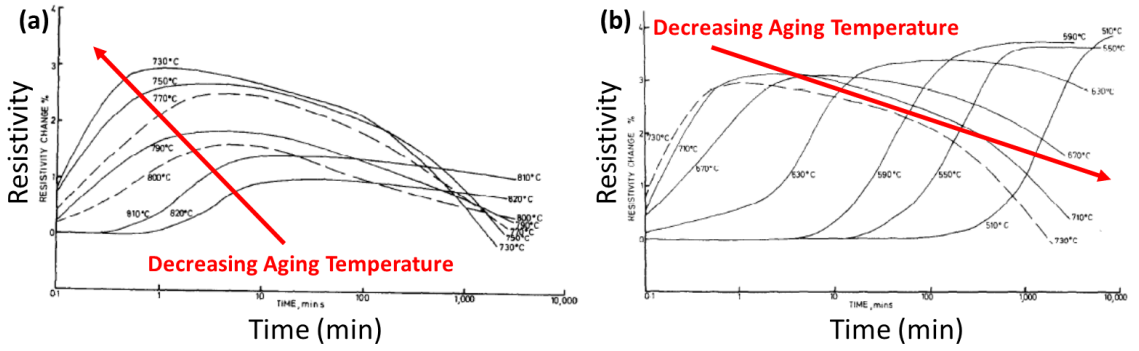

Figure 5: Change in electrical resistivity due to Ni_3Ti formation in an austenitic stainless steel, as presented by Wilson and Pickering [56]. The specimens were heat treated using varying aging temperatures, and the data is presented for (a) high aging temperatures and (b) lower aging temperatures. The axis labels and arrows indicating the trends with temperature have been added for easier viewing.

Figure 4(b) suggests faster kinetics to reach the resistivity maximum as the aging temperature is increased; however, Wilson and Pickering [56] were able to show a C-curve type response for aging of an austenitic stainless steel. These results are given in Figure 5. Figure 5(a) represents the higher aging temperatures and clearly shows that the kinetics initially speed up as the temperature is decreased. For aging temperatures less than 730°C, the kinetics become slower as the temperature is decreased, as shown by Figure 5(b). This C-curve type response to time and temperature is expected for a nucleation and growth process such as precipitation [31]. The precipitates formed during these experiments were Ni_3Ti, which has a similar chemistry to the γ' phase in Waspaloy. These Ni_3Ti precipitates formed large coherency strains with the matrix after long-term aging, which resulted in noticeable resistivity increases [56]. For Waspaloy, the low lattice mismatch between the precipitates and matrix makes such coherency strains unlikely - even after long-term aging [71].

Another interesting observation by Wilson and Pickering [56] was that the precipitates had sizes of approximately 1nm at the resistivity maximum, regardless of the aging temperature. This was also noted by several other researchers using a variety of characterization techniques. Specifically these precipitate sizes were confirmed by TEM studies [56], X-ray diffraction [57], and small angle X-ray scattering [54] for three separate alloy systems.

2.3.3 Resistivity Studies on Other Non-Nickel Alloys

Electrical resistivity is commonly used in industry to non-destructively monitor several alloy types. In fact, most papers available in the literature involve electrical resistivity testing of Mg, Cu, and Al alloys for a variety of processing conditions. For conciseness, selected papers on this subject have been cited [60–69].

Most studies have used electrical resistivity to prove whether or not a precipitation or dissolution reaction has occurred. For precipitation, the removal of solute results in a resistivity decrease. The addition of solute to the matrix from dissolution thus resulted in resistivity increases in several instances [62, 64]. While many studies qualitatively associated the solute content in the matrix as the reason for the electrical response [63–69], little work has been performed concerning quantifying the precipitate microstructure from resistivity measurements, as is the goal of this project. Such qualitative studies are especially useful for cases where more than one precipitation process occurs with processing. In such instances, multiple resistivity peaks have been observed with aging, with each precipitation reaction yielding a distinct peak [67]. Resistivity measurements have also been used to calculate the temperatures at which various precipitation reactions occur. Barucca et al. [61] showed that the temperature derivative of the resistivity was identical to the differential scanning calorimetry (DSC) trace of heat treated QE22 Mg.

Most studies involving the effects of precipitation on resistivity focus on the matrix solute content, since conduction electron scattering from precipitates is only dominant at the initial aging times, when the precipitates are first nucleated. A recent study has focused on this nucleation regime, whereby the resistivity maximum was fit with a Johnson-Mehl-Avrami (JMA) type equation [60]. Ferragut et al. [60] showed an excellent fit of this JMA equation to the measured resistivity of a 7012 aluminum alloy, as shown by Figure 6. It can be seen that the fitted JMA lines closely match the measured resistivity data points in all cases. The volume fraction of the GP zones was found to increase very similarly to the resistivity, causing the authors to attribute the volume fraction of zones to the resistivity maximum [60]. This is in agreement with the classic resistivity experiments mentioned in the previous section. The inset of Figure 6 shows that the resistivity eventually decreases

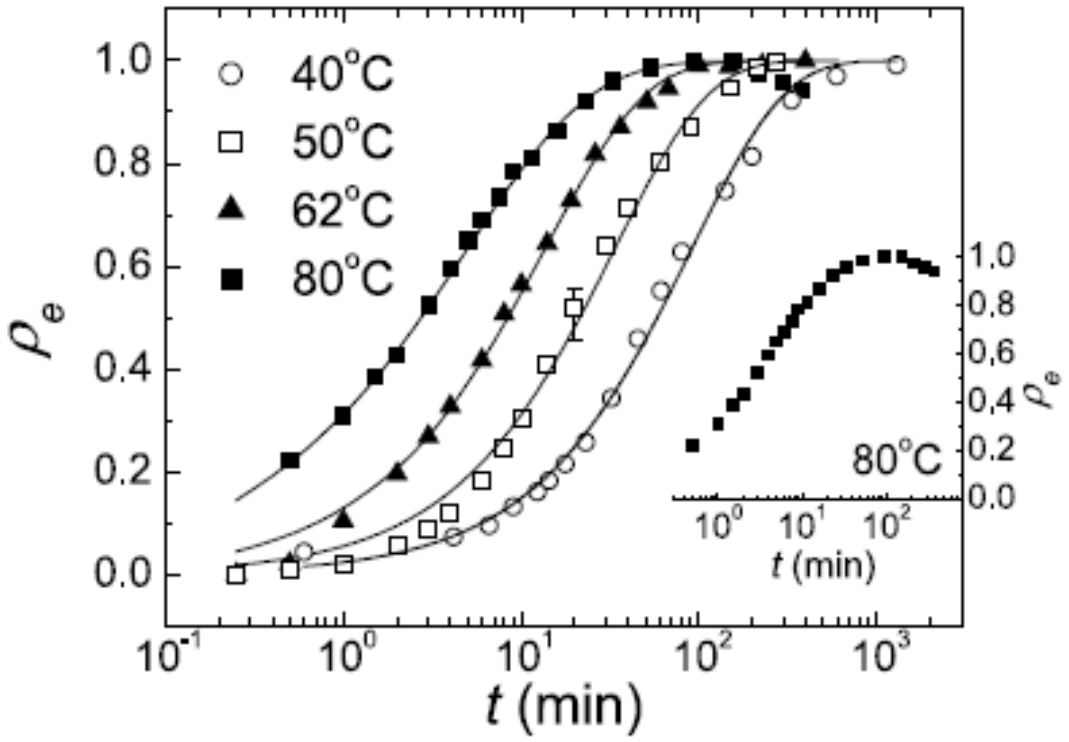

Figure 6: Relative resistivity with JMA type fits for heat treatment of 7012 aluminum [60]

for the samples heat treated at 80°C. For aging times past the maximum, the JMA model fails to describe the electrical response.

The role of dislocations on the electrical response has not been as heavily studied as for precipitates and solute atoms, but it is expected from Matthiessen's rule that these defects should also increase the resistivity [12]. It has been noted by Wilson and Pickering [56] that matrix strains increase the resistivity, which corroborates this statement. In one instance, the dislocation density was shown to be directly proportional to the resistivity in a strain hardened aluminum alloy [72]; however, the effects of dislocations have been shown to be negligible compared to the effects of the precipitation process itself in another aluminum alloy [68]. In one instance, a resistivity decrease was noted upon cold working of an aluminum alloy [69]. Even though the structural defects in the matrix increased by five orders of magnitude, the effects of solute segregation during cold rolling were more significant and caused the resistivity decrease. These results imply that precipitates and

solute atoms dominate the resistivity response; therefore, the effects of dislocations on the resistivity would only be seen when the precipitates are widely spaced and the solute content is unchanging. This will occur after long-term aging, as was observed by Wilson and Pickering [56].

2.3.4 Resistivity Studies on Nickel-Base Superalloys

Electrical resistivity testing of nickel-base superalloys is far less common in the literature than for the more simple alloy types. Marucco [70] was able to use electrical resistivity to relate Cr depletion in the matrix to precipitation in a Ni-Fe-Cr alloy. Industrially available superalloys have upwards of ten different alloying elements, making this method much more complex. Rosen et al. [3] performed resistivity measurements on several wrought nickel-base superalloys in order to calculate the activation energy for precipitate nucleation. By measuring the locations of the resistivity maximum with time and temperature, an activation energy of 250 kJ/mol was calculated [3]. The authors concluded that Ni self-diffusion was the dominant mechanism for precipitate nucleation in that study.

In order to use electrical resistivity as a non-destructive testing technique in superalloys, the electrical response must be related to the evolving microstructural defect densities. White et al. [2] were able to relate the density of solute atoms and precipitates to the electrical response of heat treated Nimonic PE16. Similarly to Matthiessens's rule, the addition of each impurity group was modeled to increase the resistivity of the PE16 alloy (ρ_{PE16}) from that of the matrix phase (ρ_{matrix}). The model for this resistivity response is given by equation 4 [2], where the subscripts i, s, and l denote impurity atoms, small precipitates, and large precipitates respectively. The small precipitate group had sizes near 1nm, and the large precipitates had sizes much larger than 1nm. As equation 4 below shows, the contribution from each impurity group on the resistivity is proportional to the number of atoms (n) in each impurity group, with n_0 representing the total number of impurity atoms available.

$$\rho_{PE16} = \rho_{matrix} + \rho_i \frac{n_i}{n_0} + \rho_s \frac{n_s}{n_0} + \rho_l \frac{n_l}{n_0} \tag{4}$$

Equation 4 showed an excellent agreement with the measured electrical resistivity of the PE16 specimens, implying that the effects of precipitates and solute atoms alone can be used to model the electrical response in superalloys under certain conditions. White et al. [2] determined that impurity atoms and small precipitates dominated the electrical response, but large precipitates had little effect. This would explain why the nucleation of small precipitates dominates the initial electrical response, whereas the removal of solute dominates the response at long aging times (when the precipitates are predominantly large).

Similarly to the goals of this project, Roebuck et al. [4] have used electrical resistivity to non-destructively obtain the equilibrium precipitate volume fraction in single crystal superalloy specimens. The authors created alloy-dependent empirical models for the evolution in this volume fraction with temperature. The precipitate volume fraction is a very useful parameter to obtain non-destructively; however, the precipitate size and spacing are also of importance towards predicting the mechanical properties of superalloys [1].

2.4 Small Angle Scattering (SAS)

2.4.1 SAS Overview

A generic schematic for a small angle scattering (SAS) setup is given by Figure 7. As Figure 7 illustrates, the incident radiation from the X-ray or neutron source has an initial wavevector k_i. After interaction with the nanometer and micrometer scale objects within the sample microstructure, the radiation scatters outwards with final wavevector k_f. SAS is an elastic scattering process; therefore, the magnitudes of both wavevectors are equal and are given by equation 5. The variable λ in equation 5 refers to the wavelength of the radiation. By measuring the intensity of the radiation scattered outwards to the detector, the scattering vector (Q) may be calculated as the difference between k_f and k_i. The scattering vector can be used as a measure of the size of the microstructural objects within the sample and is inversely proportional to the real space object size [28].

$$|k_i| = |k_f| = \frac{2\pi}{\lambda} \tag{5}$$

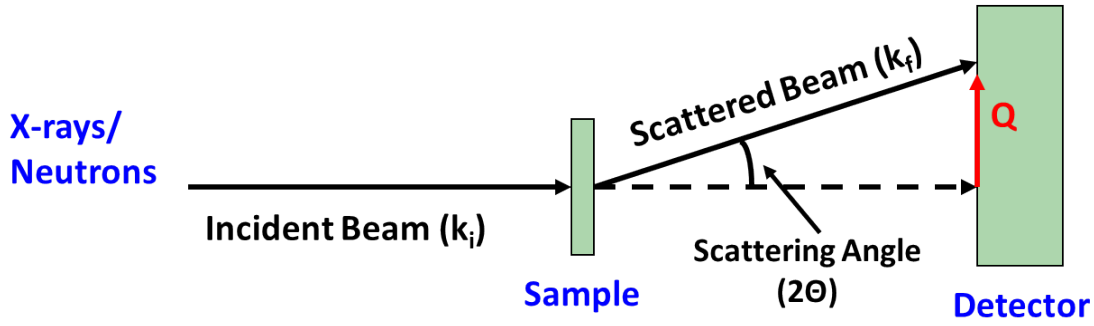

Figure 7: Schematic of a typical Small Angle Scattering (SAS) setup

Small angle scattering (SAS) is among the methods by which the γ' precipitate phase may be characterized in superalloys [7, 9–11, 13–27]. SAS is desirable relative to other characterization techniques, such as microscopy, since the measurements are performed throughout the sample volume, making the results more statistically significant. By proper fitting of the measured SAS data, volume distributions of particles can be obtained [73, 74]. For superalloys, the precipitate size, spacing, volume fraction, and distribution can all be obtained from SAS measurements. When fitting the SAS data, it is important to use models that most accurately reflect the true microstructure of the measured sample. For instance, the shape of the particles must be accounted for through the use of the correct form factor [28]. In addition, the density and composition of both the solution and particles (in this case γ and γ') must be known in order to accurately calculate the scattering contrast [28]. The scattering contrast determines the intensity of the scattering and must be known to calculate the precipitate volume fraction [28].

When performing SAS measurements, one can use either X-ray or neutron radiation. These two radiation types have different energies, penetration depths, and scattering lengths for the various elements, making some samples better suited to a particular radiation source [28]. For nickel-base superalloys, small angle neutron scattering (SANS) is far more common due to the greater penetrating power of neutrons over X-rays [13–25]. Since nickel is highly absorbent of X-rays, specimens with thicknesses on the order of 10μm to 20μm must be used for small angle X-ray scattering (SAXS) measurements [7, 9, 10]. SANS measurements, on the other hand, can measure millimeter thick samples

2.4.2 SAS Studies on Nickel-Base Superalloys

The various scattering regions for nickel-base superalloy samples can be seen in Figure 8. SAS data is often presented as shown in Figure 8, where the scattering intensity is plotted against the scattering vector (Q). As mentioned previously, Q is the difference between the scattered and incident wavevectors from the radiation. For superalloy specimens, the data exhibits distinct scattering regions for the carbides and for the γ' precipitates. Jemian et al. [75] were able to show that the scattering region from the carbide phase does not interfere with the analysis of the scattering region from the precipitate phase. Since Q is inversely proportional to the real space size, the scattering region for the micron-sized carbides occurs at low Q. The scattering intensity decreases with Q^{-4} dependence in this region, which is known as the Porod region [28]. The Porod region occurs in the high Q region for a given scattering population. Since the carbides are so large, the rest of their scattering region occurs at Q values that are too small to be measured at this time. The scattering region for the nanometer scale precipitates occurs at larger values of Q, and will shift to progressively lower Q values as they increase in size. By tracking the evolution in the γ' scattering region with heat treatment, the kinetics of the γ' phase transformation can be deduced.

The shape of the γ' scattering region will vary with precipitate spacing or sample thickness. At the initial aging times, interparticle scattering is more common due to the finely spaced precipitate phase. This interparticle scattering results in a correlation peak as shown in Figure 8. As the precipitate spacing increases, the probability of interparticle scattering decreases, resulting in the disappearance of this peak in the scattering data. When there is negligible interparticle scattering, the γ' scattering region evolves into a Debye region, where the intensity decreases with Q^{-n} dependence (n being a positive non-zero integer).

SAS has been used to study the kinetics of the γ' phase transformation in nickel-base superalloys in several instances by tracking the shift in Q of the γ' scattering region with aging time and temperature [7, 9, 11, 25–27]. This shift in Q is indicative of the evolution in precipitate size with heat treatment. These experiments have often been concerned with determining the temporal power law function for the growth of the precipitate radius [7, 9, 11, 26, 27]. These experiments have shown the expected $t^{1/3}$ behavior associated with

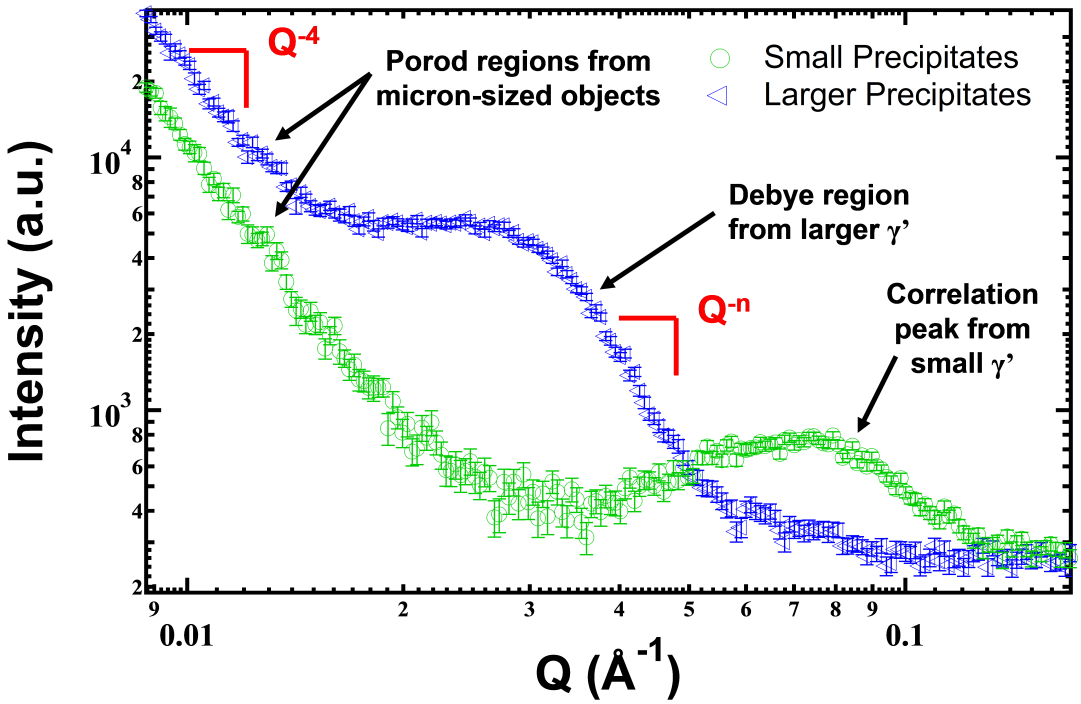

Figure 8: Representative SAS data for nickel-base superalloy specimens. The data exhibits distinct scattering regions from carbides and the γ' precipitates.

diffusion controlled coarsening [7, 9, 11, 26] as well as power laws lying between $t^{1/3}$ and $t^{1/2}$ indicating a mixed mode of growth and coarsening [9, 11, 27].

In addition to the precipitate kinetic behavior, SAS can be used to detect morphology changes in nickel-base superalloys [13, 15–17, 21, 23, 24]. It is expected that superalloys will display a progression in precipitate morphologies from spheroids to cuboids, arrays of cuboids, followed by solid state dendrites, whereby the kinetics of this transformation are controlled by the lattice mismatch [37]. For single crystal superalloy specimens, these morphology changes can be directly seen by the intensity at the SAS detector [16, 23]. Such a progression in the measured intensity is shown by Figure 9 for SANS measurements on the single crystal AM3 alloy [23]. The precipitates in this alloy were aligned along the [001] direction. By aligning the neutron beam along this direction, the transformation from spheroids to cuboids was evidenced by the intensity changing from the isotropic case of Figure 9(a) to a four-fold symmetry shown by Figure 9(b). For the spheroid morphology, the intensity at the detector will be directionally independent, yielding the ring-like isotropic

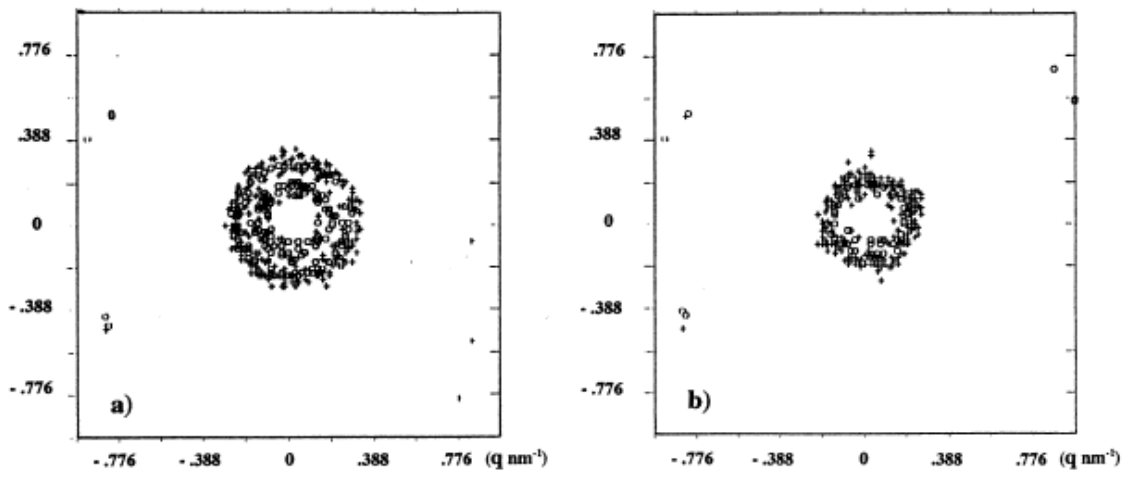

Figure 9: SANS detector image for heat treatment of AM3 single crystal superalloy specimens. The intensity measured along the [001] direction shifts from (a) isotropic scattering to (b) a four-fold symmetry, indicating the morphology change from spheroids to cuboids with heat treatment. [23]

scattering. The four-fold symmetry is due to the preferential alignment of cuboids along the [001] direction, yielding higher measured intensities along the other alignment directions and giving a diamond-shaped pattern at the detector [23]. In Figure 9, the images show the disappearance of the outer most scattering ring upon the transition from isotropic scattering to directionally dependent scattering. This is due to the increase in precipitate size occuring simultaneously to the morphology change, whereby the outer most ring shifts to lower Q. The further progression from cuboids to doublets and octets of cuboids has also been observed by SANS measurements on single crystal superalloy specimens [16]. After the initial shift from isotropic scattering to a four-fold symmetry, the scattering intensity shifted to higher values of Q, while maintaining the four-fold symmetry. This indicates that the precipitates still have cuboidal morphologies but became smaller in size, thus detecting the shift to the various arrays of cuboids [16].

The rafted morphology in nickel-base superalloys has also been detected via SAS [17, 24]. The rafted morphology involves the directional coarsening of the precipitates into plates (or rafts) through the simultaneous application of stress and thermal exposure [1]. An example SEM image of the rafted morphology may be seen in Figure 10. This is a common morphology change for superalloys used in turbine blades and is expected after long exposure

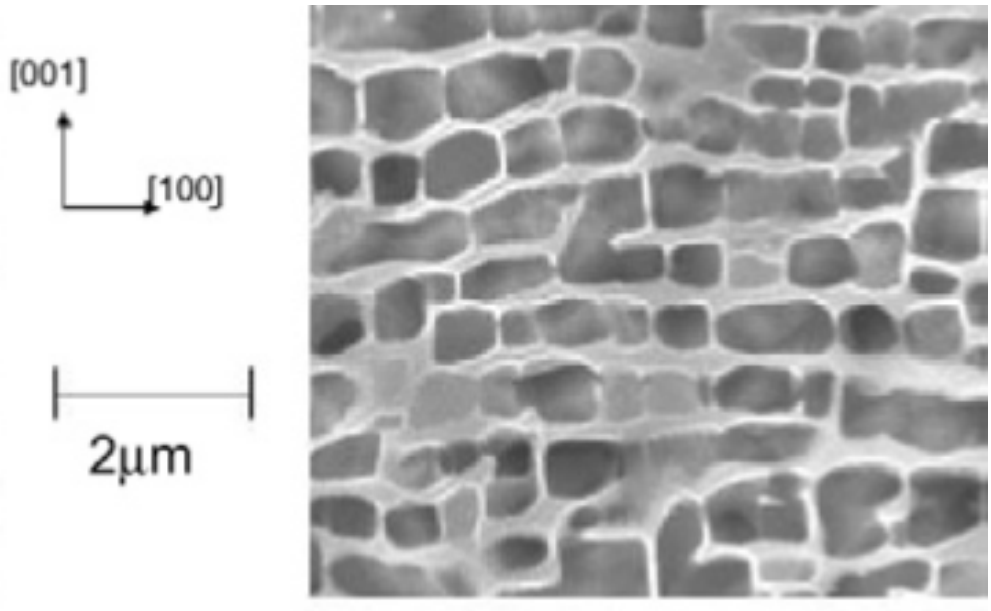

Figure 10: SEM image of the rafted morphology for precipitates in the single crystal superalloy MC-NG [17]

in the gas turbine engine, making this an important morphology change to quantify. For the transition from cuboids to rafts, the scattering intensity has shown a progression from four-fold to two-fold symmetry along the precipitate alignment direction [17, 24].

Morphology changes can also be detected for polycrystalline nickel-base superalloys [13]. Zrnik et al. [13] observed a morphology change through fitting of the measured SANS intensity versus Q data for the polycrystalline EI698VD superalloy. The transition in morphology was noted at shorter aging times than was required to image this transition in the TEM.

CHAPTER 3

EXPERIMENTAL PROCEDURE

The material tested was Waspaloy, which is a polycrystalline nickel-base superalloy primarily used in disc rotors for gas turbine engines. As-forged 13mm diameter Waspaloy bars were obtained from Fry Steel. An approximate composition quoted by Fry Steel for the Waspaloy bars is given by Table 1.

Table 1: Composition of the bulk Waspaloy bars (ignoring trace elements)

Element	Ni	Cr	Co	Ti	Al	Mo	Fe
Composition (at.%)	56.1	21.2	12.3	3.6	2.7	2.5	1.3

3.1 Heat Treatments

All heat treatments (excluding one case of an in-situ SANS measurement) were performed using a Carbolite Model CDF 12/65/500 horizontal tube furnace under flowing argon with a heating rate of 3.3°C/min during the ramp up to temperature. The as-received Waspaloy bars were first given a super-solvus solution treatment at 1145°C for 4 hours followed by quenching in an approximate 5wt% brine solution heated to approximately 50°C. This resulted in samples with grain sizes of approximately 85μm, as reported previously [5, 7].

Aging treatments were performed using two different heating schedules. The first heating schedule involved heating the solution treated bar to the chosen aging temperature, re-quenching it after the chosen aging time, sectioning approximately 2mm thick samples for characterization, then repeating these steps with the remaining bar for subsequent aging times. This cyclical method of heat treatment resulted in the samples being exposed to one extra ramp up period for each consecutive aging time that was sampled and follows the work by Kelekanjeri [76] closely. The second heating schedule involved cutting approximately 8mm sections from the solution treated bars. These sections were subsequently

aged and quenched individually, followed by further sectioning into approximately 2mm thick samples for characterization. This heat treatment schedule resulted in a single ramp up period for every aging time that was sampled.

In the case of in-situ aging during SANS measurements, a standard Institut Laue-Langevin (ILL) style furnace [77] was used under a vacuum less than 5 X 10^{-4} Torr. For these measurements, a solution treated sample was exposed to only one ramp up period, similarly to the second ex-situ heating schedule.

The aging temperatures studied were 600, 625, 650, 725, 800, and 875°C for aging times ranging between 2 min and 763.5 h. A list of all samples heat treated and measured in this thesis are given in Table 2.

3.2 Microscopy

Microscopy specimens were first ground with 400 US grit SiC grinding papers until flat. This was followed by polishing with 9μm and 3μm diamond pastes. Final polishing was performed using a suspension of 0.05μm colloidal silica mixed with 1 part 30% hydrogen peroxide, followed by polishing with a suspension of 0.05μm alumina. Contrast between the precipitate and matrix phases was achieved via two seperate etchants that have been reported previously [6] - a preferential precipitate etchant and a preferential matrix etchant. The preferential precipitate etchant consisted of 10mL each of HCl, HNO_3, H_2O, and 0.3g of molybdic acid reagent. The specimens were exposed to this etchant for approximately 15s. The preferential matrix etchant involved an electrochemical method, whereby the specimens were exposed to a solution of 2 parts methanol and 1 part HNO_3 at room temperature for 30s. During etching, a voltage of 50V DC from a Keithley 228A voltage/current source was applied.

Microstructural images were obtained using two separate scanning electron microscopes (SEM's). The samples exposed to the preferential precipitate etchant were all imaged via a Leo 1530 SEM, whereas the samples exposed to the preferential matrix etchant were imaged via a Zeiss SEM Ultra60. In addition, energy dispersive spectroscopy (EDS) measurements were also obtained using the Leo 1530 SEM. The EDS measurements were obtained to give

Table 2: List of all samples heat treated and measured. The sample types are given as follows: resistivity (R), hardness (H), microscopy (M), USAXS (U), SANS (S), and XRD (X).

Cumulative Heat Treatments		
Aging Temperature (°C)	Aging Time	Sample Type
600	2min, 6min, 18min, 30min, 1.5h, 3.5h, 8.5h, 18.5h, 38.5h, 88.5h, 163.5h, 263.5h, 463.5h, 763.5h	R, H, M, U, S
725	2min, 6min, 18min, 30min, 1.5h, 3.5h, 8.5h, 18.5h, 38.5h, 88.5h, 163.5h, 263.5h	R, H, M, U, S
800	2min, 6min, 18min, 30min, 1.5h, 3.5h, 8.5h, 18.5h, 38.5h, 88.5h, 163.5h, 263.5h	R, H, M, U, S
875	2min, 6min, 18min, 30min, 1.5h, 3.5h, 8.5h, 18.5h, 38.5h, 88.5h, 163.5h, 263.5h	R, H, M, U, S
Non-Cumulative Heat Treatments		
Aging Temperature (°C)	Aging Time	Sample Type
600	18min, 30min, 1.5h, 3.5h, 8.5h, 18.5h, 38.5h, 88.5h, 163.5h, 263.5h	R, X
625	18min, 35min, 1.5h, 3.5h, 8.5h, 12h, 15, 17h, 18h, 18.5h, 19h, 22h, 25h, 27h, 30h, 38.5h, 50h, 88.5h	R, X
650	18min, 30min, 35min, 42min, 50min, 1.5h, 3.5h, 8.5h, 18.5h, 38.5h	R, X
725	2min, 6min, 18min, 30min, 1.5h, 3.5h, 8.5h, 18.5h, 38.5h, 88.5h, 163.5h, 263.5h	R, H, M, S
800	2min, 6min, 18min, 30min, 1.5h, 3.5h, 8.5h, 18.5h, 38.5h, 88.5h, 163.5h, 263.5h	R, H, M, S
875	2min, 6min, 18min, 30min, 1.5h, 3.5h, 8.5h, 18.5h, 38.5h, 88.5h, 163.5h, 263.5h	R, H, M, S
In-Situ SANS		
Aging Temperature (°C)	Aging Time	Sample Type
725	up to 20h	S

a measure of the matrix composition for later small angle scattering (SAS) measurements. In some instances, a Park Systems XE-100 atomic force microscope (AFM) was also used for imaging.

3.3 Resistivity

Resistivity specimens were polished similarly to the microscopy specimens. DC four-point probe resistivity measurements were obtained at the center of the specimens using different orientations along the diameter for calculation of statistical error. The experimental setup consisted of a Signatone SP4-40045TFS four probe head attached to a Signatone S301-6 probe station, whereby the probe head had a spacing of 1mm between each probe. Current was applied to the outer probes using the delta mode setting of a Keithley 6221 AC/DC current source. The delta mode setting operates by quickly switching the direction of the current through the probes, so that error due to Joule heating may be removed [78]. The voltage drop across the inner two probes was measured with a Keithley 2182A nanovoltmeter. The measured electrical resistances were converted to resistivity by accounting for the sample geometry. This geometric correction factor was derived by Kelekanjeri and Gerhardt[79] for four-probe measurements along the diameter of the circular face of cylindrical specimens. A detailed explanation of the resistivity measurements and the conversion from resistance to resistivity is available elsewhere [6].

3.4 Small Angle Scattering (SAS)

3.4.1 Small Angle Neutron Scattering (SANS)

Specimen preparation for Small Angle Neutron Scattering (SANS) experiments consisted of polishing 2mm thick discs with a series of 400, 800, and 1200 US grit grinding papers to remove surface roughness. Both ex-situ and in-situ SANS experiments were conducted at Oak Ridge National Laboratory's High Flux Isotope Reactor along the CG-2 beamline [80]. This general purpose SANS beamline has a cold neutron source. The detector is a $1m^2$ area detector with $5x5mm^2$ pixel resolution. Various measurement configurations can be utilized due to the movable detector, movable neutron guides, and variable wavelengths that can be selected.

Different instrument configurations were used for the SANS measurements so that different ranges of the scattering vector, Q, could be measured. In all cases, the intensity at the detector was azimuthally averaged as a function of Q. Background scattering was removed by measuring a blank sample holder, and the data were reduced to plots of scattering intensity versus Q through the SPICE SANS reduction package[81]. This package operates within the Igor Pro software from Wavemetrics, Inc. [82], and is made freely available to those who use the CG-2 beamline.

3.4.1.1 Ex-Situ SANS

SANS measurements for samples given ex-situ heat treatment were performed using three instrument configurations (corresponding to high, medium, and low Q ranges) for every sample. This yielded a measured Q range of $10^{-3}\mathring{A}^{-1}$ to $1\mathring{A}^{-1}$. The high and medium Q ranges were obtained with a wavelength of $4.75\mathring{A}$ and a source to sample distance of 9.229m. The Q range was varied from the high to the medium range by changing the sample to detector distance from 1.161m to 8.861m respectively. The low Q range was obtained using a wavelength of $12\mathring{A}$, a source to sample distance of 17.275m, and a sample to detector distance of 19.361m.

3.4.1.2 In-Situ SANS

An approximately 5mm thick specimen was sectioned from a solution treated bar, and polished similarly to the ex-situ specimens for in-situ aging of Waspaloy during SANS measurements. For the in-situ experiment, only one configuration could be used at a given time, due to the precipitation reaction occurring simultaneously to the measurement. A constant wavelength of $4.75\mathring{A}$ and a constant source to sample distance of 8.713m were used for every measurement. The Q range was shifted to lower values as the precipitation reaction progressed by changing the sample to detector distance to progressively larger values. The three sample to detector distances used were 1.391m, 5.091m, and 9.091m. Since Q is inversely proportional to the real space size of the precipitates, this allowed for the increase in precipitate size to be tracked as the aging time increased.

3.4.2 Ultra Small Angle X-ray Scattering (USAXS)

The ultra small angle X-ray scattering (USAXS) measurements required specimens with thicknesses of approximately 10-20μm for adequate transmission of the X-ray beam. Such thinning is required for X-rays as compared to neutrons due to the high absorption of X-rays by nickel. The specimens were first ground with 400 US grit grinding papers until they began to peel off the mount. The specimen was then polished with a series of 800 and 1200 US grit grinding papers and removed from the mount. Approximately 5x5mm^2 specimens were cut from the thinned sample for further thinning with a Gatan disc grinder. The unpolished face was then polished with a series of 400, 800, and 1200 US grit grinding papers until final specimen thickness was achieved.

All USAXS experiments were conducted at Argonne National Laboratory's Advanced Photon Source along the 32-ID beamline [83]. The USAXS setup at the 32-ID beamline uses a double-crystal configuration (rather than the movable area detector in the case of the SANS measurements), making multiple instrument configurations unnecessary. The measurements were performed using 11.9keV X-rays in all cases. The scattering intensities were reduced to slit smeared USAXS data through the Indra 2 package [84], which also operates within the Igor Pro Software [82].

3.4.3 SAS Data Fitting

All data fitting for both SANS and USAXS measurements was performed using the Irena SAS package [74] within the Igor Pro software [82]. The data were modeled with a discrete volume distribution of particle scatterers; the theory behind such modeling was first reported by Potton et al. [73]. The generic equation for modeling the measured SAS intensity with a volume distribution of particle scatterers is given by equation 6 [74].

$$I(Q) = \sum \Delta\rho^2 S \sum F^2 V f \Delta D \tag{6}$$

In equation 6, the first summation is performed over each distribution of particle scatterers, and the second summation is performed over each diameter bin within a given distribution. The term $\Delta\rho^2$ is the scattering contrast, which is related to the difference

in density and composition of the particle and matrix phases (in this case the γ and γ' phases) [28]. The second term in equation 6, S, is the structure factor, which accounts for interparticle scattering [28]. The term, F, is the form factor, which accounts for the shape of the particles. The remaining terms in equation 6 (namely V, f, and ΔD) are the particle volume, volume distribution, and the width of the diameter bin respectively. In all cases, the primary distribution of precipitates was fit with a Gaussian distribution of particles. In the case of the cyclically heat treated specimens, a smaller, secondary distribution of precipitates was evidenced in the USAXS data. For this secondary distribution, the data were fit with either a Gaussian or a log normal distribution. These distribution types were chosen, as they resulted in the best fit to the measured SAS data.

In order to calculate the scattering contrast, the composition of the matrix phase was obtained via EDS measurements on specimens exposed to the preferential precipitate etchant. This composition is given nominally as $Ni_{0.607}Cr_{0.2304}Co_{0.135}Mo_{0.028}$. The composition of the precipitate phase was assumed to be $Ni_3Al_{0.5}Ti_{0.5}$, since the ideal composition of the γ' precipitates is expected to be Ni_3(Al, Ti) [1].

A hard sphere model was assumed for the structure factor for the Waspaloy system, whereby the precipitates are assumed to be spheroids that do not interpenetrate. A representative example of the precipitate microstructure for the aged Waspaloy specimens exposed to the matrix etchant is given in Figure 11, which shows a specimen that was aged at 800°C for 263.5h. Figure 11 clearly shows that the precipitates are predominantly spheroids, making the hard sphere model a good description of the true Waspaloy microstructure. The equation for the hard sphere model structure factor is given by equation 7 [74].

$$S(Q) = \frac{1}{1 + 3CN[sin(Q\Delta) - Q\Delta cos(Q\Delta)]/(Q\Delta)^3} \tag{7}$$

This structure factor depends on the correlation distance (center-to-center distance) between particles, Δ, as well as the particle coordination number, CN.

Since the precipitates are known to be spherical, the form factor for spheroids was used and is given by equation 8 [28]. In equation 8, r is the radius of the spherical particles.

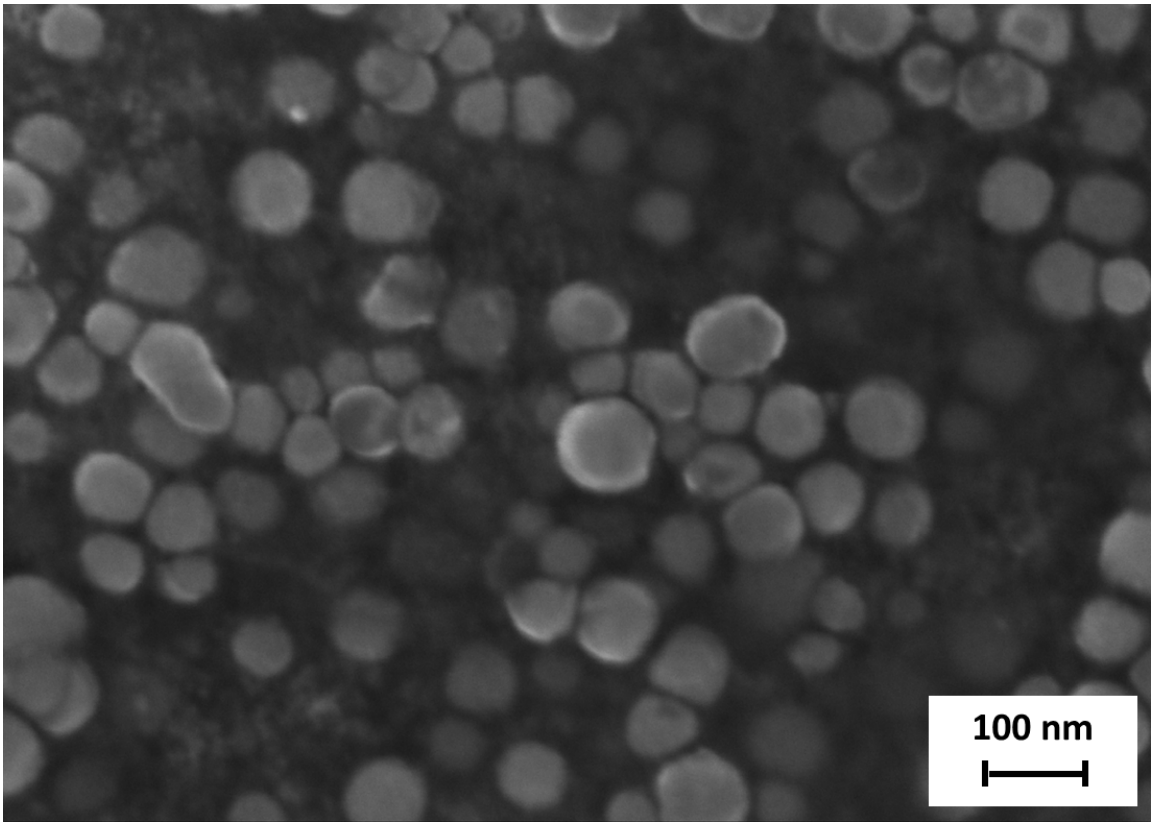

Figure 11: Image of the γ' microstructure for a Waspaloy specimen heat treated at 800°C for 263.5h. The image shows that the precipitate morphology is predominantly spherical.

$$F(Q) = \frac{3[sin(Qr) - Qrcos(Qr)]}{(Qr)^3} \tag{8}$$

3.5 X-ray Diffraction (XRD)

Specimens for X-ray diffraction measurements were polished similarly to the microscopy and resistivity specimens. XRD scans were obtained using a PANalytical X'Pert PRO Alpha-1 diffractometer with Cu Kα_1 radiation. This instrument has a solid state X'Celerator detector and a Bragg-Brentano parafocusing setup. The diffracted intensities were measured for 2Θ angles ranging from 42.981° to 100.000° with a step size of 0.0334225° and a scan rate of 0.005655° per s. All data analysis and background removal was performed using the JADE 9 software from Materials Data, Inc [85].

3.6 Hardness

Hardness specimens were polished similarly to the SANS specimens to remove surface roughness. Vickers microhardness measurements were obtained using a Leco MHT series 200 microhardness tester. The measurements were performed using a load of 1kg and a 15s indent time.

CHAPTER 4

COMPARISON OF SANS VS. USAXS

Small angle scattering (SAS) measurements have been performed on nickel-base superalloy specimens using both X-rays [7, 9, 26, 27] and neutrons [10, 11, 13–25]; however, small angle neutron scattering (SANS) measurements are far more prevalent in the literature. X-ray radiation is less penetrating than neutron radiation, which necessitates thinner samples for X-rays [28]. In addition, the scattering lengths of the elements are widely different for X-ray radiation as compared to neutron radiation, due to the difference in each radiation type's interaction with matter. X-rays interact with the electron cloud, whereas neutrons interact with the nucleus [28]. The difference in scattering lengths can result in widely different scattering contrasts for X-rays as compared to neutrons. As this chapter will show, each method has its own strengths and is better suited to certain types of samples and heat treatment conditions. The available facilities for each measurement type also vary depending on the institution. For instance, the USAXS beamline at the Advanced Photon Source allows for anomalous USAXS measurements and USAXS imaging to also be performed, which are not common techniques among small angle scattering beamlines [83].

In this chapter, a comparative study between SANS measurements and ultra small angle X-ray scattering (USAXS) measurements was performed for Waspaloy specimens heat treated at 800°C for aging times ranging between 0.5h and 88.5h. Aging was performed utilizing the cyclic heat treatment method, whereby each subsequent aging time involved an extra heating up cycle. The measured SAS data and the subsequent fitted particle size distributions for both techniques were compared. The γ' precipitate microstructure induced for these heat treatment conditions is given by Figure 12. The precipitates shown in Figure 12 display the expected increase in size and spacing with aging time and remain spherical throughout all aging times measured.

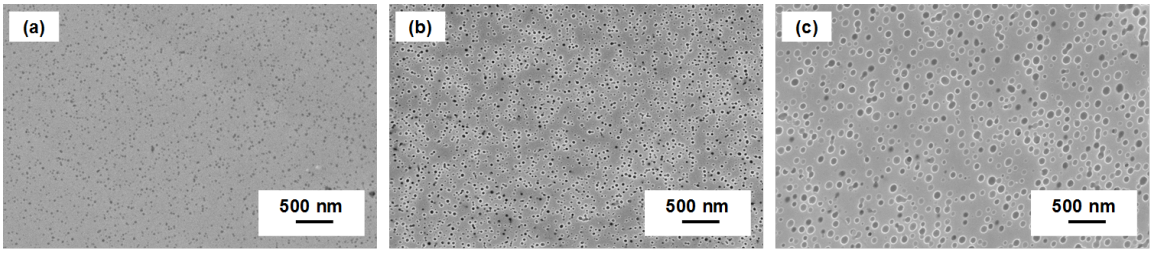

Figure 12: SEM images of the γ' precipitate microstructure in Waspaloy after heat treatment at 800°C for (a) 8.5h, (b) 38.5h, and (c) 263.5h respectively. The images show the expected increase in precipitate size and spacing with aging time.[10]

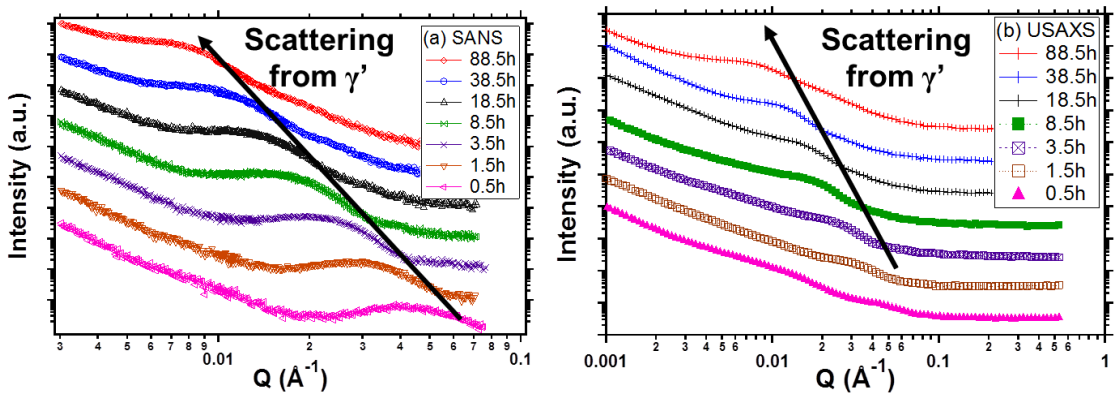

Figure 13: Small angle scattering data for Waspaloy specimens heat treated at 800°C as measured by (a) SANS and (b) USAXS [10]

4.1 SAS Data

The measured SAS data due to the evolving precipitate microstructure shown in Figure 12 is presented in Figure 13. The data were fit with volume distributions of spherical particles for both the SANS and USAXS measurements. Each aging time has been shifted in intensity, in order to make the dataset more readable.

The data presented in Figure 13 are very similar in many respects. Both SANS and USAXS measurements display the expected scattering regions due to carbides at low Q along with the scattering regions due to the γ' precipitates at higher Q (see Section 2.4.2). In both cases, the γ' scattering region shifts to progressively lower Q with aging time, which is evidence of the increase in precipitate size; however, the shape of the γ' scattering region is different as measured by the two different techniques. The SANS data, shown by Figure 13(a), displays a correlation peak for the γ' scattering region. This is indicative of

interparticle scattering [28]. The USAXS data, shown by Figure 13(b), displays a Debye region, whereby the scattering intensity decreases with Q^{-n} dependence, n being a positive, non-zero integer. The presence of a Debye region in the USAXS data suggests that an insignificant amount of interparticle scattering occurred during these measurements [28].

The difference in the shape of the γ' scattering regions can be explained by the difference in sample geometry. The USAXS specimens were required to be 10-20μm thick in order to adequately transmit the X-ray beam, while the SANS specimens were approximately 2mm thick (see Section 3.4). As specimen thickness increases, the probability of interparticle scattering increases [28], which accounts for the large degree of interparticle scattering evidenced in the SANS data that is not present in the USAXS data. The presence of the correlation peak in the SANS data is beneficial towards studying the evolution of the precipitate microstructure in Waspaloy, since the precipitate correlation distance (center-to-center distance) and coordination number may be obtained from fitting of the data. Since there are no correlation peaks in the USAXS data, this information cannot be obtained.

The SANS measurements were also able to detect the γ' precipitates at shorter aging times than the USAXS measurements, as can be seen by the well defined γ' scattering region at 0.5h for the SANS case that is not clearly visible in the USAXS case. It is believed that the difference in scattering contrast between the two radiation types explains the earlier detection of the γ' precipitates via SANS. An increase in the scattering contrast would result in a larger measured intensity for a given sample. In addition, the SANS samples, being of much greater thickness than the USAXS samples, had a much larger number of precipitates, which would also contribute more to the scattering intensity at any given aging time.

4.2 Particle Size Distributions

The SAS data shown in Figure 13 were fit with a volume distribution of particle scatterers. The particle size distributions (PSD's) obtained from this fitting are shown in Figure 14, whereby the PSD for each aging time has been shifted upwards to increase the readability of the data.

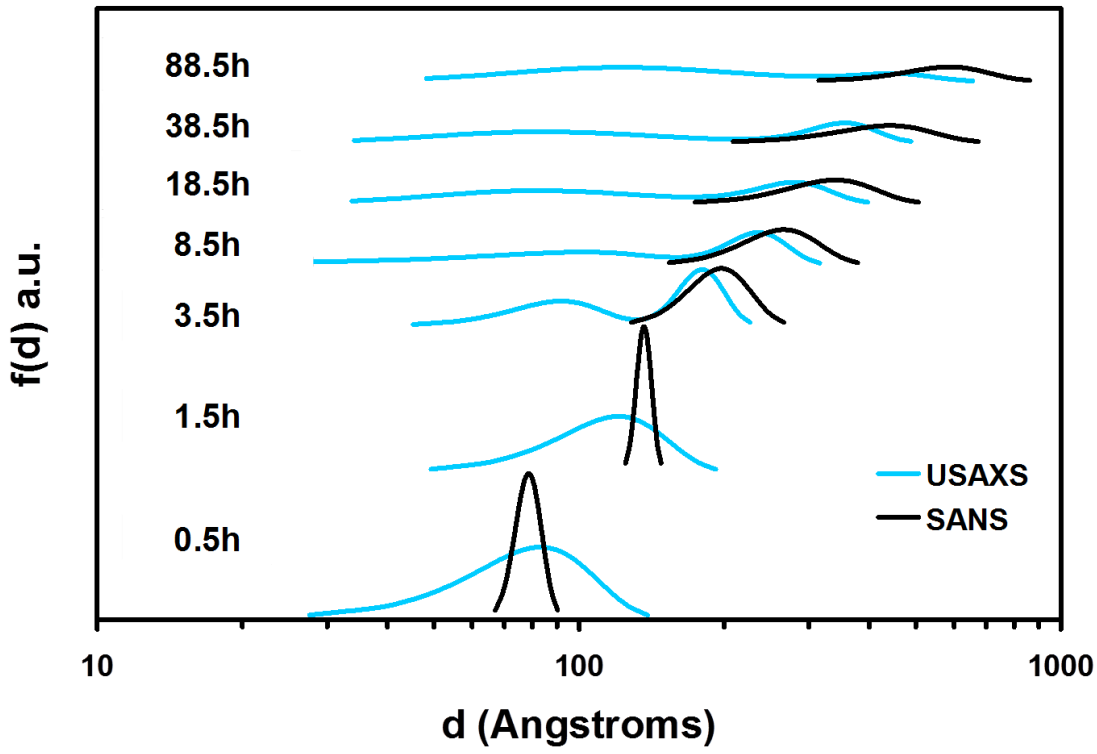

Figure 14: Particle size distributions (PSD's) of the γ' precipitate phase in Waspaloy after cyclic heat treatment at 800°C. The PSD's obtained from USAXS measurements show a bimodal behavior that is not evident in the SANS data. The primary USAXS distribution is shifted to smaller diameters due to the smaller sample volume required for USAXS measurements. [10]

The PSD's as measured by both SANS and USAXS are different in several ways. The distributions obtained from fitting of SANS data are tighter than those obtained by USAXS measurements for the lowest aging times. The more obvious difference between the two data sets is that the USAXS data shows an evolution to a bimodal distribution with aging time. Such a bimodal distribution has been shown previously for USAXS measurements on Waspaloy specimens [7]. It will be shown in Chapter 8 that the secondary distribution is due to the cyclic heat treatment schedule used. Unlike the USAXS data, the SANS data shows a single primary distribution throughout all measured aging times. It is possible that the detector used for the USAXS measurements had a higher resolution, yielding a lower error in the intensity versus Q data. A lower intensity error would make data fitting to more than one distribution easier. Regardless of the origin of this difference, the primary distribution appears to dominate the SANS results in all cases.

Another difference in the PSD's is that the primary distributions are shifted to larger diameters for the SANS case as opposed to the USAXS case. This discrepancy can be explained by the difference in sample geometry between the two measurements. The smaller measured volume of the USAXS samples would result in the preferential removal of the largest precipitates near the surface of the specimens. The SANS specimens had thicknesses that were several orders of magnitude larger than the largest precipitates, which would make this effect negligible. The larger sample volume for SANS specimens also makes these measurements more statistically significant than USAXS measurements on Waspaloy samples.

4.3 Conclusions

The SAS data for Waspaloy specimens cyclically heat treated at 800°C shows distinct differences when measured via SANS as compared to USAXS. The measured SAS data is very similar between the two cases, except that the SANS data shows correlation peaks for the γ' scattering region that are not evident in the USAXS data. This allows for the precipitate correlation distance and coordination number to be obtained via SANS - but not via USAXS. The main differences between the two measurement techniques involved

the fitted particle size distributions of the γ' phase. USAXS was able to detect a secondary precipitate size distribution that was not evidenced in the SANS data. Conversely, the SANS measurements yielded more accurate primary particle size distributions due to the much larger specimens that were measured and the higher statistical significance associated with these samples. In Chapter 8, it will be shown that the secondary precipitate size distribution is due to the cyclic heat treatment schedule used for these experiments. USAXS is thus more useful for cyclically heat treated Waspaloy specimens, whereas, SANS measurements are more useful for specimens that are not cyclically heat treated.

CHAPTER 5

COMPARISON OF EX-SITU VS. IN-SITU SANS

Small Angle Neutron Scattering (SANS) is a useful method for measuring the kinetics of phase transformations in nickel-base superalloys [10, 11, 16, 17]. Of particular interest is the temporal power law function that describes the increase in the precipitate radius due to heat treatment. A $t^{1/3}$ rate law is indicative of diffusion controlled coarsening, and a $t^{1/2}$ rate law is indicative of diffusion controlled growth [31]. In nickel-base superalloys, mixed modes of growth and coarsening have been previously evidenced from small angle scattering measurements [9, 27].

In this chapter, the effects of in-situ versus ex-situ heat treatment on SANS samples are studied in order to assess the effects of removing samples from the furnace and quenching to room temperature. Such in-situ SANS measurements have been performed for nickel-base superalloy specimens previously [14, 16, 17]. Both the in-situ and ex-situ heat treatments presented here were performed using a non-cyclic heating schedule at 725°C. The differences between the measured γ' precipitate size distributions for the two different heat treatment methods are explored, with particular emphasis placed on evaluating the temporal power law function mentioned above.

5.1 SANS Data

As the SANS data will show, the precipitate radii were on the order of single nanometers for the heat treatment conditions used in this chapter. A representative example image of the precipitate microstructure can be seen by Figure 15. It is apparent from Figure 15(a) that the precipitates were difficult to view in the SEM, even at 50kx magnification. Figure 15(b) is an AFM amplitude image for a specimen heat treated at 875°C for 2min. The higher aging temperature and different imaging technique allowed for the small precipitates to become clearly visible.

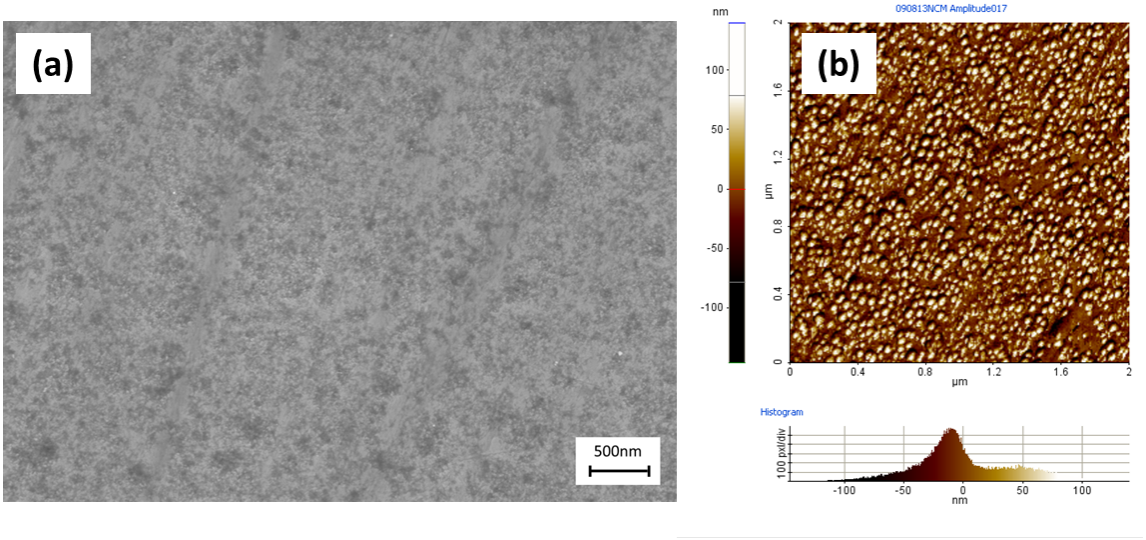

Figure 15: Images of the γ' microstructure for ex-situ Waspaloy specimens heat treated for short aging times. The images are (a) an SEM image after heat treatment at 725°C for 2min and (b) an AFM amplitude image after heat treatment at 875°C for 2min. The precipitates are visible as small, upraised spheres. Due to the heat treatment conditions used, the precipitates were of small size for all aging times.

The SANS spectra for both in-situ and ex-situ heat treatment at 725°C are given by Figure 16. Only selected aging times were chosen for Figure 16 to increase the readability of the data. In the case of the in-situ data, the approximate mid-point of the measurements was used for the listed aging times, and time zero was taken as the time at which the furnace first reached a steady 725°C. Much longer aging times were able to be measured for samples given ex-situ treatment, as seen by the specimen aged for 263.5h on Figure 16(b). The longest measured aging time for the in-situ specimen was approximately 21h. It should also be noted that the ex-situ data was obtained in absolute units, but the in-situ data was unable to be converted to absolute units due to the inability to measure the intensity standard at the temperature used in the experiment. Therefore Figure 16(a) has an arbitrary intensity scale.

Figure 16 displays all of the scattering regions expected from superalloy specimens (see Section 2.4.2). The scattering region due to the γ' precipitates is a correlation peak, due to interparticle scattering. As would be expected, the γ' scattering regions shift to progressively lower Q with aging time due to the increase in precipitate size. While the SANS

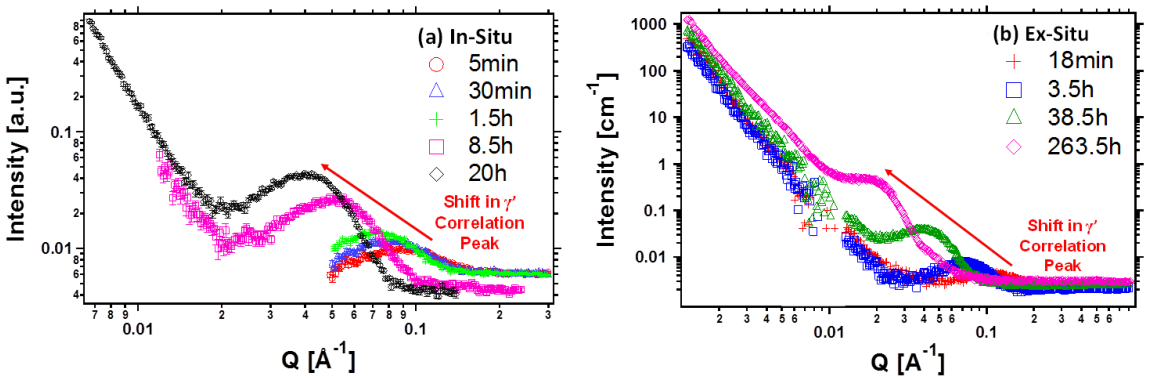

Figure 16: SANS spectra for both in-situ and ex-situ heat treatment at 725°C. The scattering region for the γ' precipitates shifts to progressively lower Q with aging time, due to the increase in precipitate size.

spectra behave similarly for both in-situ and ex-situ heat treatment, it is important to compare the microstructural data obtained by fitting of the measured SANS data.

5.2 Microstructural Data

The measured SANS data was fit with a volume distribution of spherical particles, as described in Section 3.4. The most relevant microstructural data obtained from this fitting was the average precipitate radius ($\langle r \rangle$), correlation distance (Δ), and coordination number (CN). These microstructural data are shown in Figures 17, 18, and 19 respectively. For the case of in-situ aging, the data points are located at the midpoint in the measurement for the aging time, and the time error bars represent the spread over the entire measurement.

5.2.1 Precipitate Size and Nearest Neighbor Data

5.2.1.1 Average Precipitate Radius

The evolution in $\langle r \rangle$ with aging time for both in-situ and ex-situ heat treatment is given in Figure 17. The error bars for $\langle r \rangle$ represent the standard deviations of the fitted volume distributions. The radii increase with aging time in both cases, as would be expected for a precipitation reaction. The precipitates remain small throughout all aging times, having values ranging between 1nm and 5nm for the heat treatment conditions used. Such small precipitate sizes are corroborated by the barely visible precipitates shown in Figure 15.

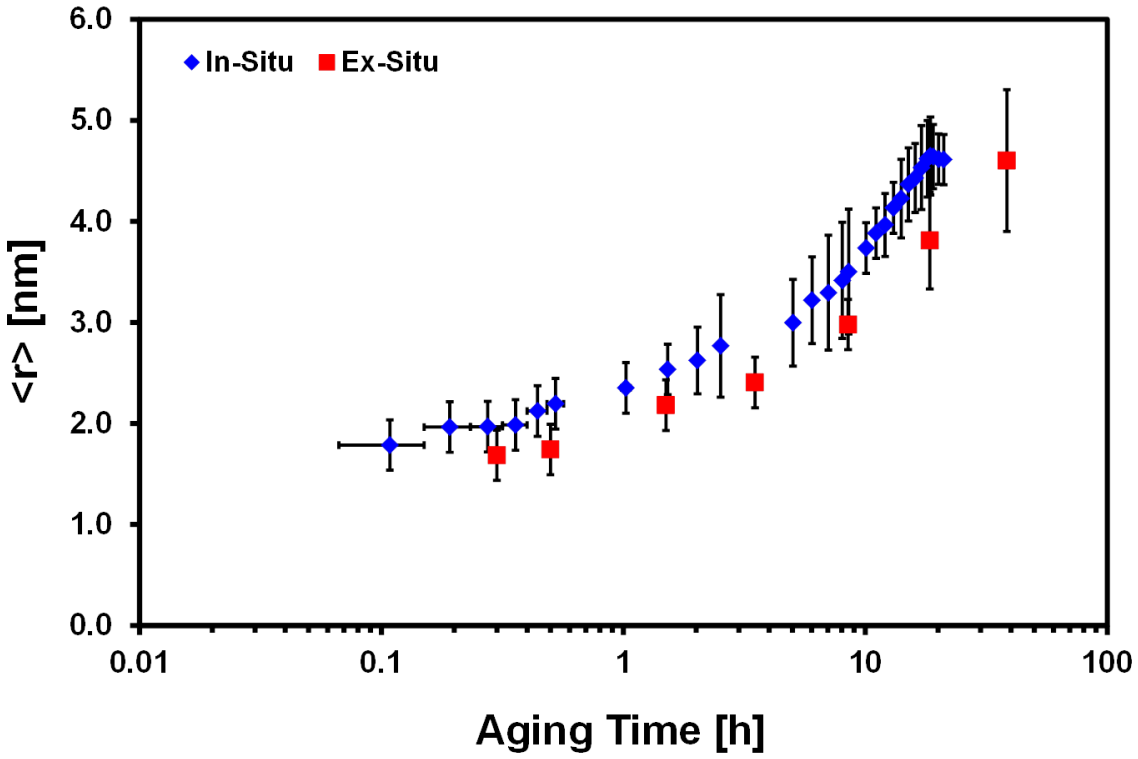

Figure 17: Average precipitate radius as a function of aging time for both in-situ and ex-situ heat treatment at 725°C. The radii increase in both cases, as would be expected, and are within the statistical error at any given aging time.

The values for $\langle r \rangle$ are shifted to slightly larger values for the in-situ heat treatment as compared to the ex-situ heat treatment; however, the values are well within the measured statistical error in all cases, making the relative difference between the two heat treatment procedures negligible. The differences in the data may be explained by the spread in time that the measurements were performed over. Since the precipitation reaction was occurring simultaneously to the measurement, it would be expected that the precipitates would grow to slightly larger sizes than if the microstructure was frozen in time.

5.2.1.2 Correlation Distance

The trends in correlation distance (Δ) with aging time are given by Figure 18. Similarly to $\langle r \rangle$, the Δ values increase with aging time for both in-situ and ex-situ heat treatment. This increase in precipitate spacing is a normal precipitation behavior. Unlike the $\langle r \rangle$ values, the Δ values are significantly larger for the in-situ data set as compared to the ex-situ data

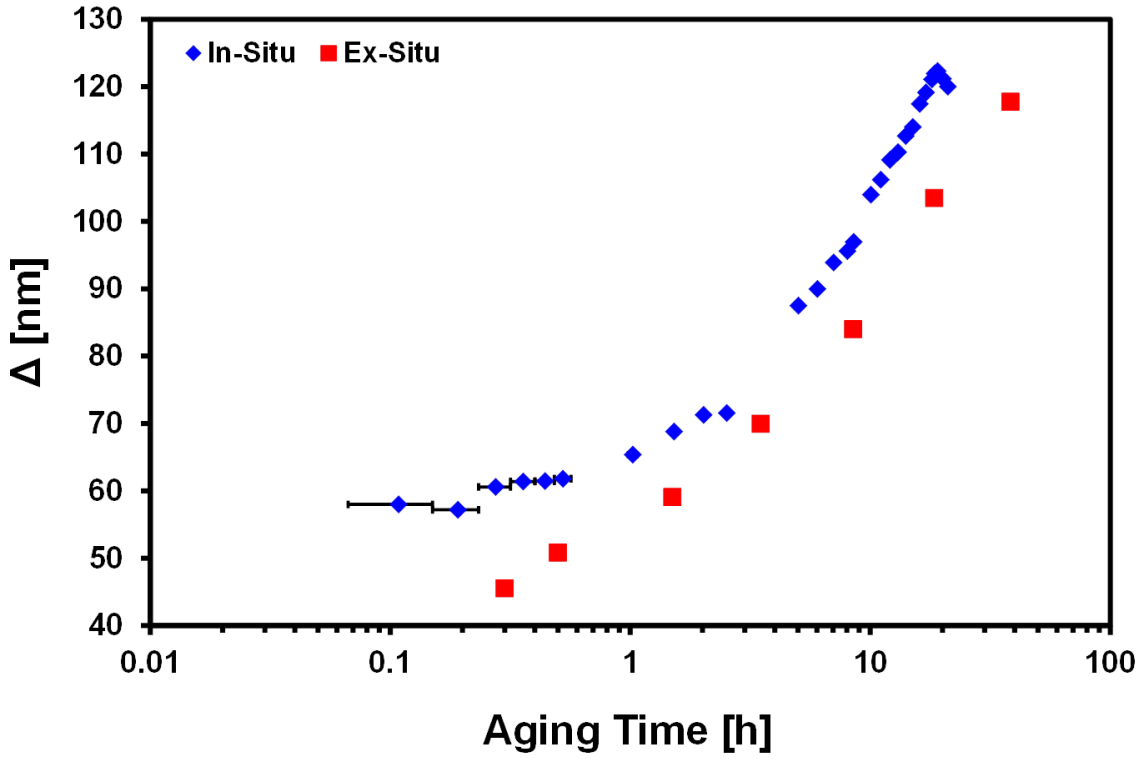

Figure 18: Correlation distance (center-to-center distance) between precipitates as a function of aging time for both in-situ and ex-situ heat treatment at 725°C. The values increase with aging time, as would be expected, but the precipitate to precipitate distance for the in-situ sample is noticeably larger than for the ex-situ samples in all cases.

set. It was not possible to calculate statistical error for the correlation distances, since only single scattering runs were performed for each sample. It is possible that the in-situ data would be within the measurable error of the ex-situ data, if multiple scattering runs were performed for both the in-situ and ex-situ cases.

5.2.1.3 Coordination Number

The trends in the γ' precipitate coordination number (CN) are given by Figure 19. Unlike the average radii and correlation distances, CN decreases with aging time. It is to be expected that the precipitate microstructure will tend towards a smaller number of larger, widely-spaced precipitates; therefore, the trends shown by Figures 17-19 are reasonable. Similarly to $\langle r \rangle$, the CN data for both in-situ and ex-situ heat treatment is very similar, and has values ranging between 3 and 5 nearest neighbor precipitates. Figure 19 displays a

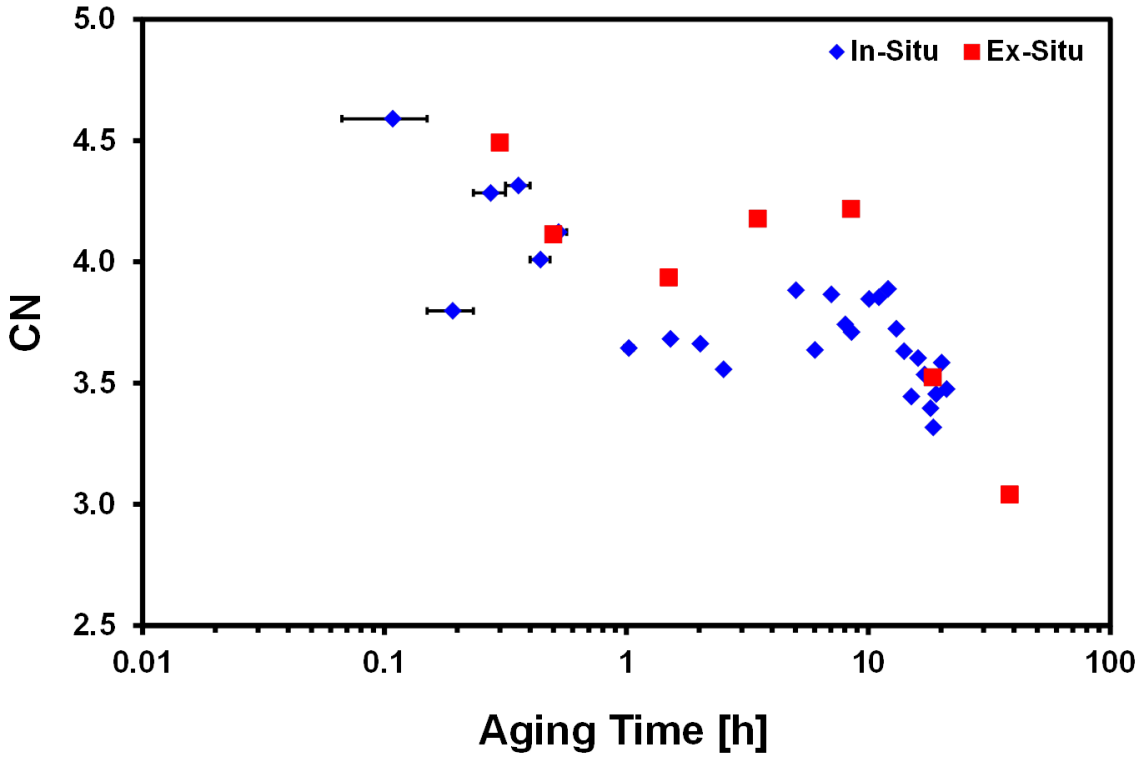

Figure 19: Precipitate coordination number as a function of aging time for both in-situ and ex-situ heat treatment at 725°C. The data decreases with time in both cases, with similar data for both in-situ and ex-situ heat treatment.

large degree of scatter for both data sets, but the in-situ data points fall very closely to the ex-situ data points in most cases. It is again not possible to calculate the statistical error for this data for the reasons discussed earlier; however, it can be stated that the data are quite similar regardless.

5.2.2 Characteristic Rate Laws

The average radii shown in Figure 17, were used to calculate the temporal power law function describing the increase in the precipitate radius with aging time. The data were plotted as the natural logarithm of the radius versus the natural logarithm of the aging time, as shown by Figure 20. The slopes of the lines seen in Figure 20 represent the power law exponent describing the increase in the γ' precipitate radius with aging at 725°C.

The data is again within the measured statistical error for both data sets; however, the trends in the data are slightly different. It is obvious from Figure 20, that the in-situ

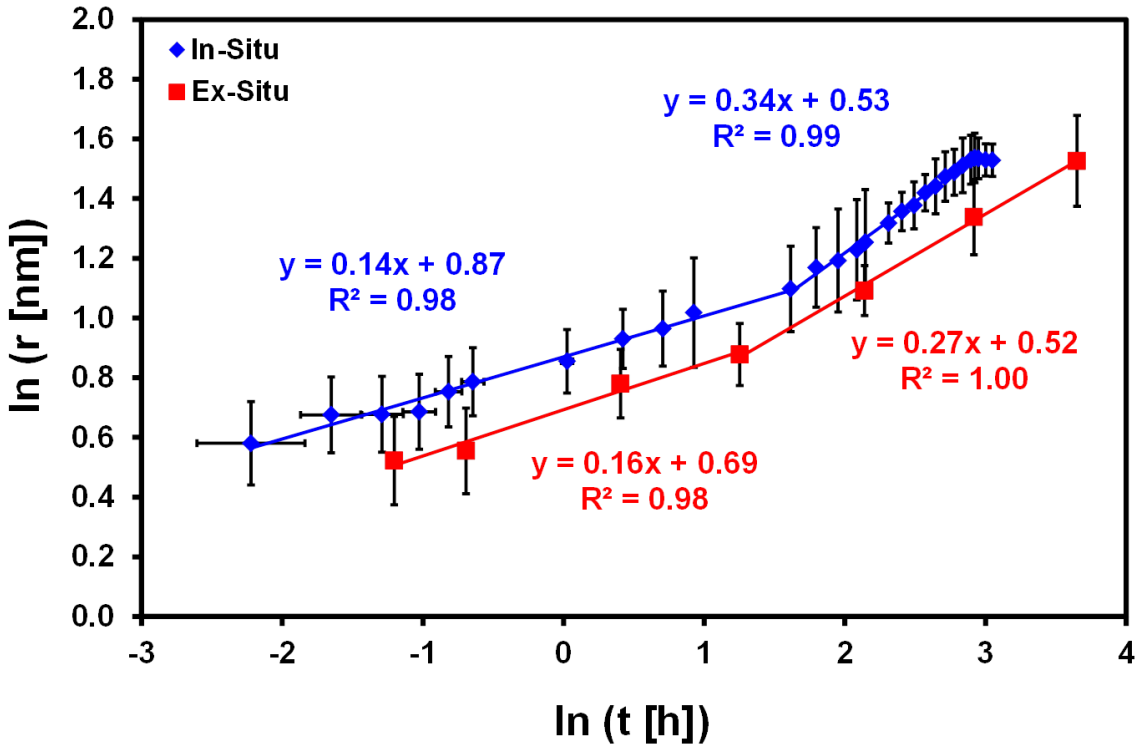

Figure 20: Natural logarithm of the precipitate radius plotted against the natural logarithm of the aging time for both in-situ and ex-situ heat treatment at 725°C. The data were fit via linear least squares regression, with the slopes of these linear fits representing the power law exponent describing the increase in the γ' precipitate radius with aging time.

data displays two distinct linear regions. While two linear regions can be fit to the ex-situ data set, the data could also be misconstrued as having a single linear trend. The data for in-situ aging, shows an initial $t^{0.14}$ dependence that increases to a $t^{0.34}$ dependence at later aging times. The data for ex-situ specimens shows a $t^{0.16}$ followed by a $t^{0.27}$ dependence respectively. The differences between the in-situ and ex-situ data can best be explained by the limited number of data points for the ex-situ specimens. For the in-situ case, the data were taken at five and ten minute intervals, but for the ex-situ specimens, only selected aging times could be measured. The larger number of measured aging times for the in-situ case, resulted in a much smoother trend in the data.

The rate laws calculated from both in-situ and ex-situ data imply that the specimens have not yet reached the diffusion controlled growth regime for the aging treatment conditions at 725°C used in this chapter. This is to be expected, since it has already been shown that longer aging times and higher temperatures would be required to reach the diffusion controlled growth or coarsening stages in this alloy [7, 9]. For this particular case, at 725°C, the in-situ data appears to be more reliable than the ex-situ case, as the rate law is evolving quickly with aging time.

5.3 Conclusions

The γ' precipitate microstructure behaved similarly as measured by SANS measurements for specimens given either in-situ or ex-situ heat treatment at 725°C. In both cases, the average precipitate radii and correlation distances increased with aging time, and the coordination number decreased with aging time, as would be expected. The most significant difference in the two data sets was for the rate of increase in the precipitate radii. A plot of the natural logarithm of the precipitate radius versus the natural logarithm of the aging time revealed two growth rates for both the in-situ and ex-situ datasets; however, the two regions were much more distinct in the in-situ case. For the in-situ case the radii first increased with $t^{0.14}$ dependence followed by $t^{0.34}$ dependence, whereas the ex-situ data showed a $t^{0.16}$ followed by a $t^{0.27}$ dependence. The discrepancy is believed to be due to the limited number of data points in the ex-situ data, which resulted in slightly different data trends.

The results suggest that care must be taken in interpreting the growth rates from SANS data on specimens given ex-situ heat treatments. For cases where the rate law is evolving with time, sufficient aging times should be sampled such that a smooth trend in the data can be obtained. Both data sets suggest that the the diffusion controlled growth stage was not reached for the heat treatment conditions used in this study.

CHAPTER 6

RESISTIVITY AND HARDNESS TRENDS

The electrical resistivity of nickel-base superalloys will evolve as the precipitation process occurs, due to the competing processes of precipitate formation and solute removal [2–4]. In order to non-destructively monitor the precipitate microstructure (and also the mechanical properties), proper electrical response-microstructure models must be developed. Quantifying the precipitate microstructure using small angle scattering was the subject of the previous two chapters. In this chapter the trends in the electrical and mechanical response due to γ' precipitation in Waspaloy are explored. Four-probe resistivity measurements and Vickers microhardness measurements are compared as a function of aging time for specimens cyclically heat treated at 600, 725, 800, and 875°C, with microstructural explanations given for the trends in both measurements.

6.1 Precipitate Microstructure

The evolution in the precipitate microstructure due to the heat treatment conditions used in this chapter is given in Figures 21-23. Figure 21 displays the evolution in the γ' precipitate microstructure for Waspaloy specimens heat treated at 875°C for increasing aging times. The spherical precipitates show a clear progression from an initial small, finely-spaced phase to a larger, widely-spaced phase with aging time. The large object visible in Figure 21(a) is an etch pit - not a γ' precipitate. This alloy has been shown to display etch pits at the lowest aging times when this preferential precipitate etchant is used [6].

The trends in the γ' microstructure with temperature are shown by Figure 22, whereby the specimens were heat treated for 163.5h for increasing aging temperatures. Similarly to Figure 21, the precipitates increase in size as the aging temperature is increased, as the rate of solute diffusion will be faster at higher temperature.

The γ' precipitates were not visible in the SEM for aging at 600°C; therefore, the atomic force microscope (AFM) and the preferential matrix etchant were used to image

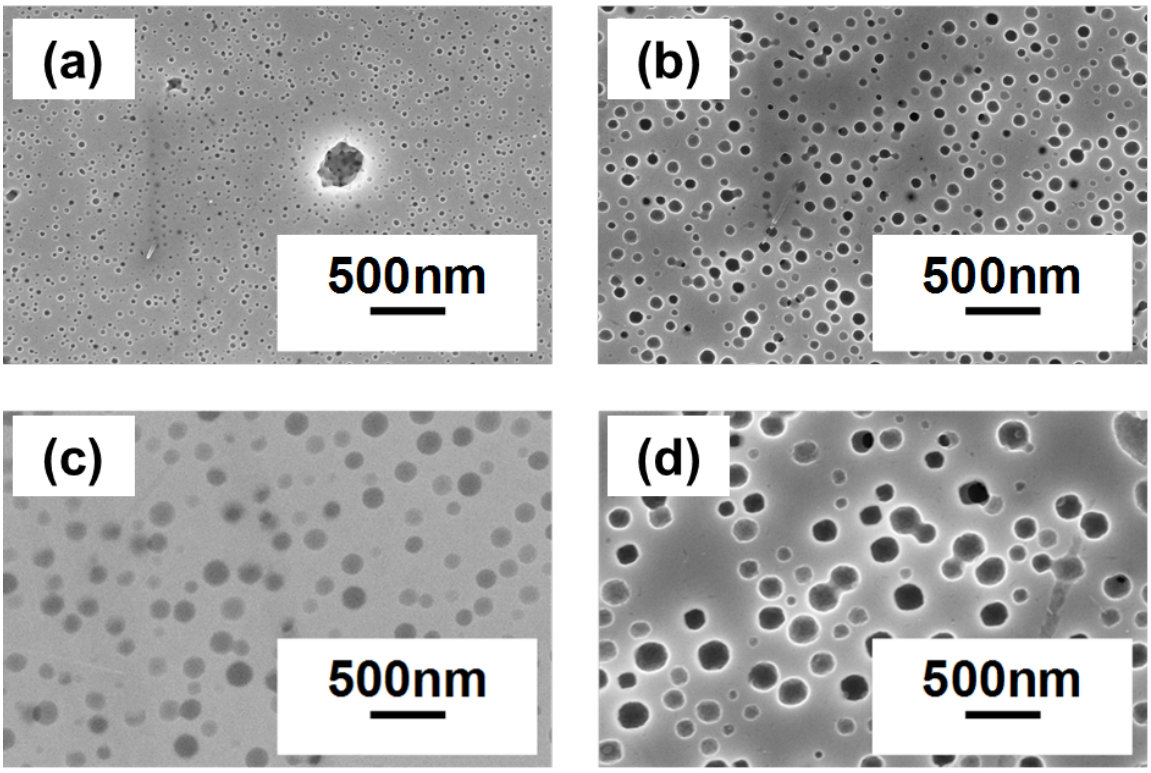

Figure 21: SEM images of the γ' precipitate microstructure in Waspaloy after heat treatment at 875°C for (a) 1.5h, (b) 18.5h, (c) 88.5h, and (d)163.5h respectively. The images show the expected increase in precipitate size and spacing with aging time.[8]

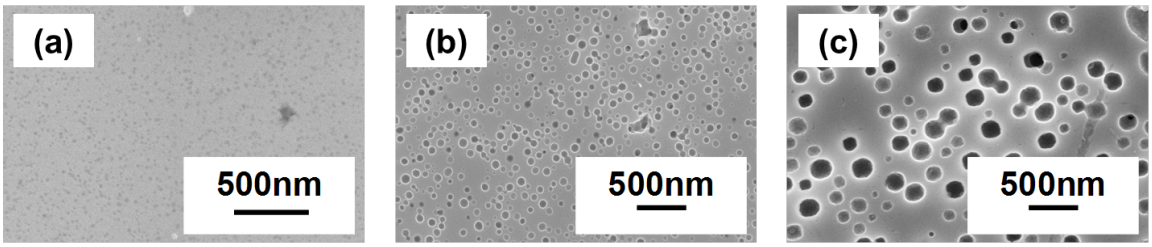

Figure 22: SEM images of the γ' precipitate microstructure in Waspaloy after heat treatment at (a) 725°C, (b) 800°C, and (c) 875°C for 163.5h. The images show the expected increase in precipitate size with aging temperature, due to faster solute diffusion at higher temperature.[8]

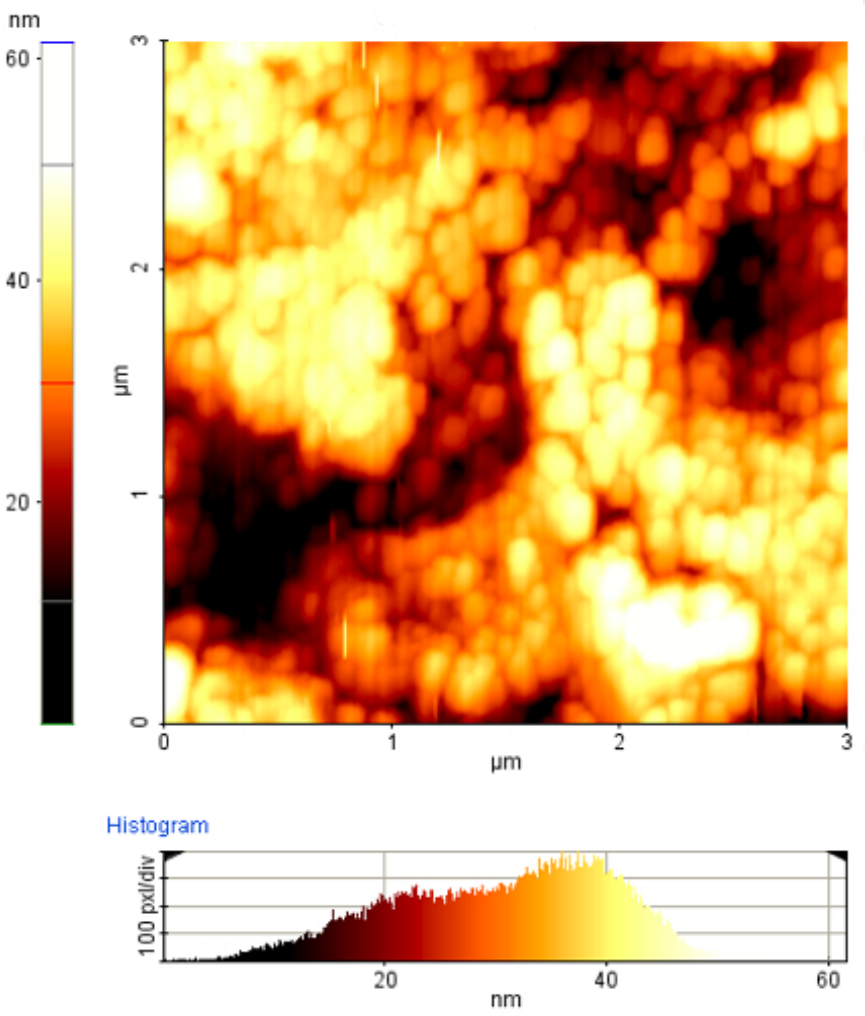

Figure 23: AFM topographical image of the γ' precipitate microstructure in Waspaloy after heat treatment at 600°C for 763.5h. AFM imaging was required for the specimens heat treated at 600°C, due to the much smaller precipitate sizes. [8]

specimens at this temperature. Figure 23 shows the small spherical precipitates for a Waspaloy specimen heat treated at 600°C for 763.5h.

6.2 Electrical Conductivity

The calculated electrical resistivity values were converted to electrical conductivity by taking the inverse and are given in Figure 24. The data points located at 0.01h represent the solution treated specimens. The conductivity displayed an initial decreasing trend (corresponding to increasing resistivity) for aging at 600, 725, and 800°C. This is the expected electrical response for a precipitation hardened alloy, whereby the initial nucleation

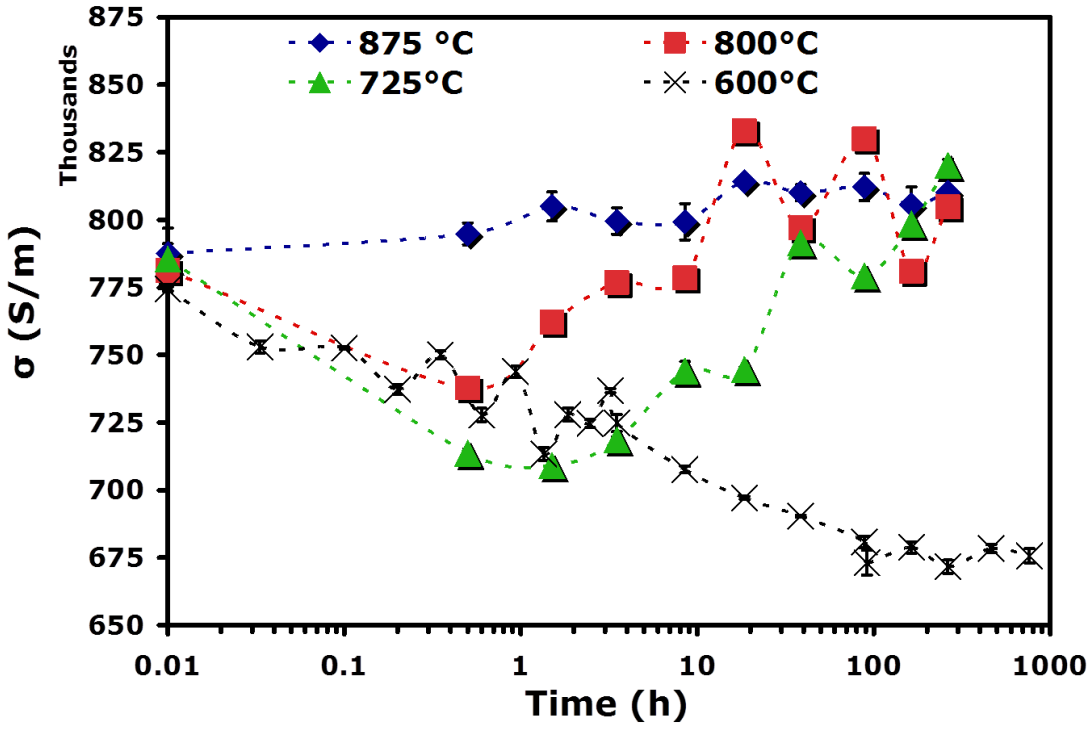

Figure 24: Electrical conductivity as a function of the aging time for Waspaloy specimens heat treated at 600, 725, 800, and 875°C. The values located at 0.01h represent the solution treated specimens. [8]

of precipitates causes an increase in conduction electron scattering [53–57]. A conductivity minimum was reached after 163.5h, 1.5h, and 0.5h for aging at 600, 725, and 800°C respectively.

The decreasing conductivity region was not evidenced by the samples heat treated at 875°C. At 875°C the data shows an increasing trend throughout all measured aging times. This can be explained by the faster solute diffusion expected at 875°C compared to the lower aging temperatures. Consequently, much shorter aging times would need to be measured such that the decreasing conductivity region would be evidenced.

After the initial conductivity minimum (resistivity maximum) the conductivity increases with aging time, as shown by the 725°C and 800°C sample sets. This increasing conductivity region can be explained by two mechanisms. The first mechanism is the increase in precipitate spacing, whereby the mean free path through the precipitates is increasing with aging

time (see Figure 21). The second mechanism is the removal of precipitate forming solute atoms from the matrix phase, as the precipitate volume fraction increases. As Matthiessen's rule states, purer metals will also be more electrically conducting [12]. The increasing conductivity region is therefore due to a decrease in conduction electron scattering from both precipitates and solute atoms.

The specimens aged at 600°C do not show the eventual increase in conductivity that is present for the other aging temperatures. Instead, the conductivity decreases to a minimum after 163.5h of aging and stays relatively constant for the remaining aging times. This can be explained by the much slower solute diffusion expected for aging at 600°C as compared to the higher aging temperatures. If longer aging times were sampled for the 600°C data set, then the increasing conductivity region should eventually be evidenced.

During the increasing conductivity region, the data shows a fluctuating behavior with aging time for the 725, 800, and 875°C sample sets. As will be shown in Chapter 8, the fluctuating resistivity behavior may be explained by the presence of a smaller, secondary precipitate population [9, 10]. The formation of these smaller precipitates would result in an increase in conduction electron scattering. Due to the cyclic heating schedule used for these experiments, the secondary precipitate population has been shown to go in and out of solution with aging time [9], which would account for the fluctuating conductivity behavior shown in Figure 24.

6.3 Vickers Microhardness

The Vickers microhardness values obtained from Waspaloy specimens heat treated at 600, 725, 800, and 875°C are given in Figure 25. The measured hardness trends are as described in Section 2.1 for superalloy specimens. The data shows an increasing hardness region for the initial aging times at all four aging temperatures; however, there is some scatter in the data at the lowest aging times, especially for aging at 600°C. The increasing region is expected due to the increasing stress required for dislocations to shear through precipitates. Hardness maxima were obtained after aging at 88.5h and 1.5h for heat treatment at 800°C and 875°C respectively. Hardness maxima were unable to be obtained for heat treatment at

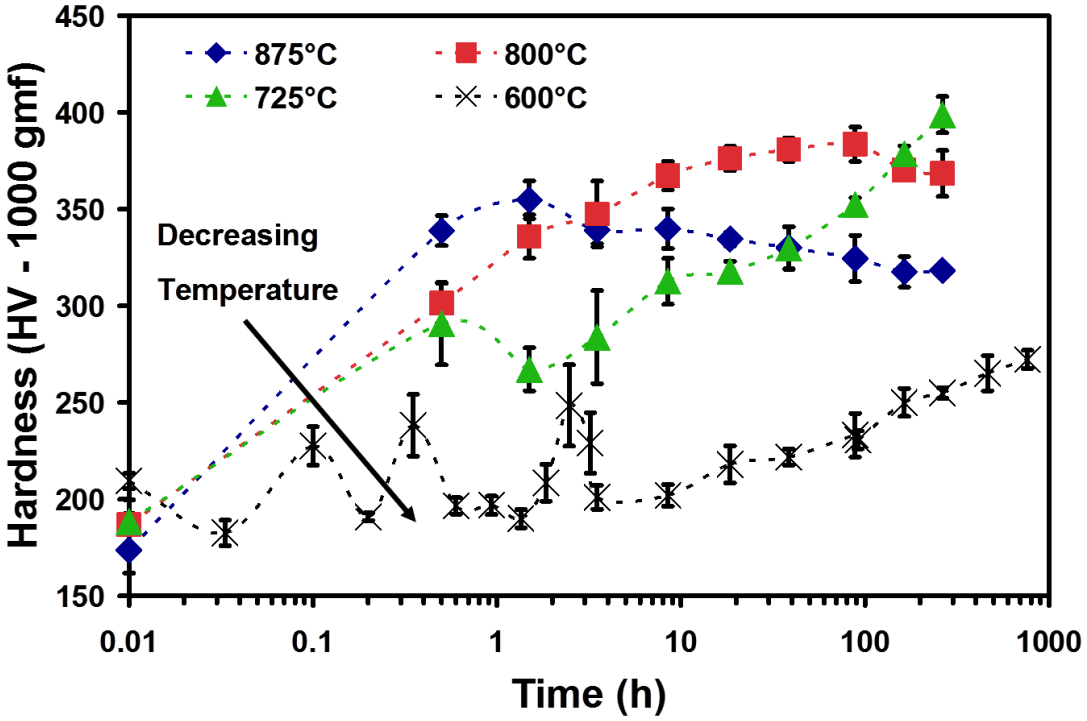

Figure 25: Vickers microhardness as a function of the aging time for Waspaloy specimens heat treated at 600, 725, 800, and 875°C. The values located at 0.01h represent the solution treated specimens. [8]

600°C and 725°C, due to the slower kinetics of growth at these lower temperatures. After the hardness maximum, the Vickers microhardness values decrease with continued aging at 800°C and 875°C. This is as expected due to the decreasing stress required for dislocations to undergo Orowan bowing as a means of moving throughout the material.

6.4 Correlations between the Electrical and Mechanical Response

The generic trends in the electrical conductivity and Vickers microhardness can be summarized as follows. The conductivity quickly reaches to a minimum followed by a much slower increase to a maximum with aging time. The Vickers microhardness displays a single maximum that occurs at similar aging times to the maximum in conductivity, as is evidenced by the samples heat treated at 800°C and 875°C in Figures 24 and 25. The similar peak locations can be explained by the precipitate phase reaching the equilibrium volume fraction in the vicinity of the hardness maximum [86]. Once the equilibrium volume fraction

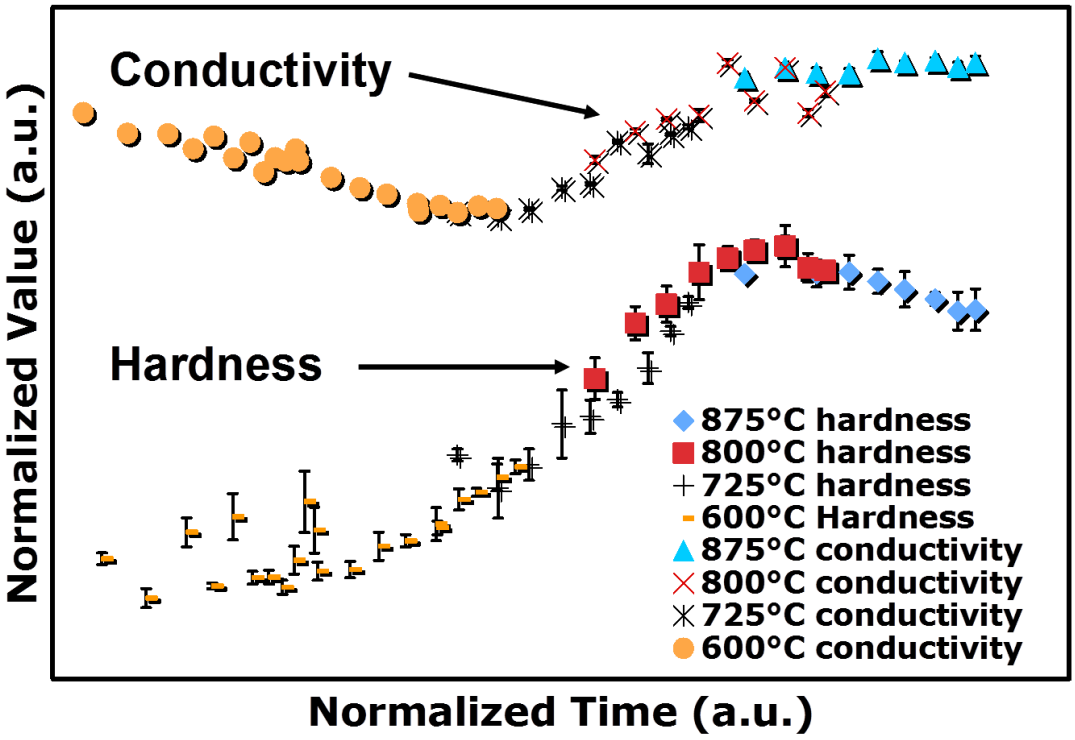

Figure 26: Normalized conductivity and hardness values as a function of normalized aging time for Waspaloy specimens heat treated at 600, 725, 800, and 875°C. The conductivity and hardness values are plotted on a linear scale, whereas the aging times are plotted on a logarithmic scale. [8]

is reached, this indicates that the maximum amount of solute will have been removed from the matrix phase for a given aging temperature - thus causing a conductivity maximum.

In order to better compare the electrical and mechanical response as a function of the aging time, the conductivity and hardness data shown in Figures 24 and 25 were normalized with respect to time and magnitude using the extrema in the two data sets as reference points for normalization. This normalized data is given by Figure 26. For Figure 26, the y axis is plotted on a linear scale, and the x axis is plotted on a logarithmic scale to match Figures 24 and 25.

Figure 26 allows for the empirical trends in the electrical and mechanical response due to γ' formation to be more readily identified. It is obvious from Figure 26 that the initial conductivity minimum occurs at much shorter aging times than the hardness maximum. The conductivity minimum (or resistivity maximum) is due to a microstructure with the

maximum capability of scattering conduction electrons, whereas the hardness maximum is due to a microstructure with the maximum capability of impeding dislocation motion. The difference in the underlying mechanisms promoting changes to these two measurements can account for the difference in peak locations. As previously mentioned, the location of the conductivity and hardness maxima occur at similar aging times - most likely due to the equilibrium γ' volume fraction being reached.

6.5 Conclusions

Four-point probe resistivity testing has proven to be sensitive to the γ' precipitation process in Waspaloy. The electrical conductivity shows an initial decrease to a minimum, due to the fast nucleation of the precipitates. The conductivity then shows a much slower increase to a maximum that occurs at similar aging times to the maximum in the Vickers microhardness. These similar peak locations can be explained by the precipitates reaching their equilibrium volume fraction, whereby both maximum resistance to dislocation motion and maximum removal of matrix solute are both achieved.

In order to use electrical resistivity testing as a viable method for monitoring precipitation in superalloys, quantitative models for the electrical response due to the precipitate microstructure must be developed. The following chapters will involve fitting the electrical response with microstructural models. Relationships between the mechanical properties and precipitate microstructure are well researched up to this point [1]; however, Appendix A presents a microstructural model for the decrease in hardness in the over-aged regime. Such modeling is useful towards predicting the decrease in strength or hardness due to coarsening of γ'.

CHAPTER 7

RESISTIVITY DURING PRECIPITATE NUCLEATION

The electrical resistivity of precipitation hardened materials shows a fast increase to a maximum due to nucleation of a fine precipitate phase. This maximum in resistivity has often been attributed to the volume fraction of the precipitates or zones that are nucleated [53–55]. This region has also been modeled with a Johnson-Mehl-Avrami (JMA) [32, 33] type equation for aging times up to the initial resistivity maximum [58, 60]. In this chapter, the electrical response of Waspaloy specimens heat treated at 600, 625, and 650°C was modeled with a similar JMA model for aging times ranging between 2min and 263.5h. The evolution of the calculated rate constants with temperature was used to calculate an activation energy for the nucleation of γ' in Waspaloy. The precipitate volume fraction was obtained via X-ray diffraction (XRD), similarly to Ferragut et al. [60]. The evolution of the precipitate volume fraction was compared to the electrical response to ascertain the role of the volume fraction on the initial resistivity peak maximum.

7.1 X-ray Diffraction Data

Proof of γ' nucleation was obtained from X-ray diffraction (XRD) scans on the heat treated Waspaloy specimens. A representative example scan is given by Figure 27. In all cases, the γ' peaks were of far smaller intensity than the γ matrix peaks, due to the expected small volume fraction of precipitates during the nucleation regime. For a given lattice reflection, the precipitate and matrix peaks occured at similar scattering angles (2Θ). This can be attributed to the expected low lattice mismatch in Waspaloy [37, 71], whereby the lattice parameters of both phases have similar values. The two phases also have similar crystal structures. The matrix phase is FCC, and the precipitate phase has the ordered $L1_2$ structure, which is similar to the FCC crystal structure [1]. The XRD data shown in Figure 27 shows the expected behavior for γ' precipitation in nickel-base superalloys such as Waspaloy [38].

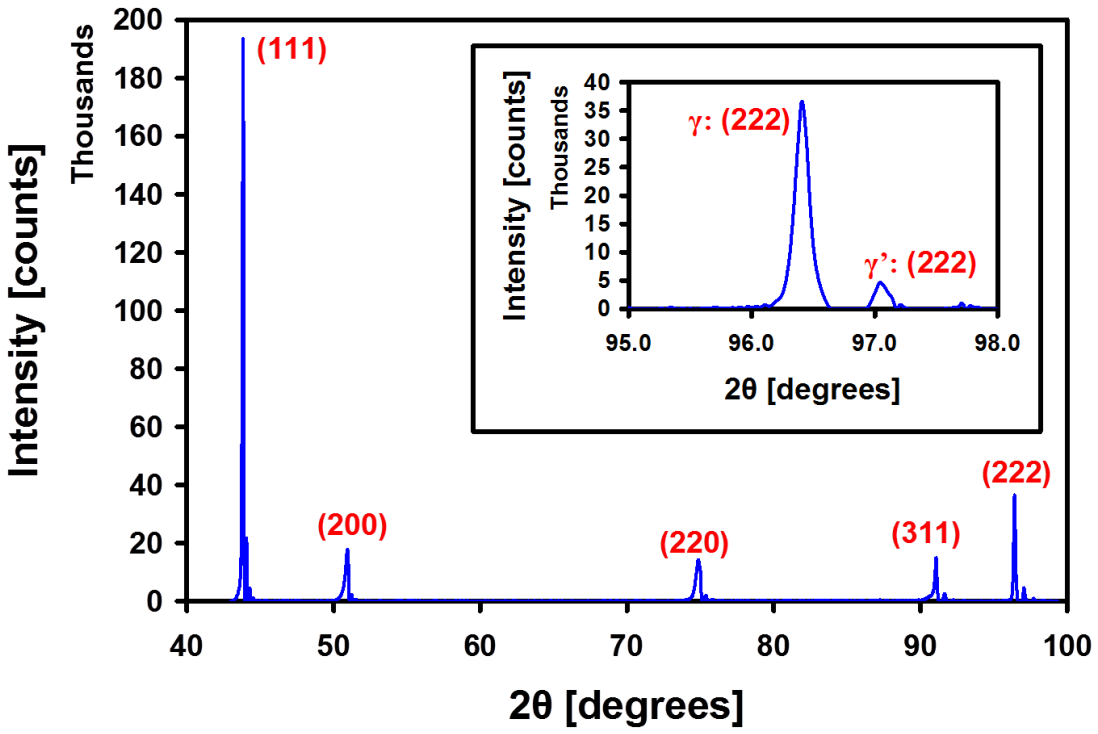

Figure 27: XRD scan of a Waspaloy sample heat treated at 650°C for 8.5h. The matrix and precipitate peaks occur at similar scattering angles due to a low lattice mismatch and similar crystal structures. The relative intensities of a matrix peak compared to a precipitate peak can be better seen by the inset, where the (222) lattice reflection of both phases is shown.

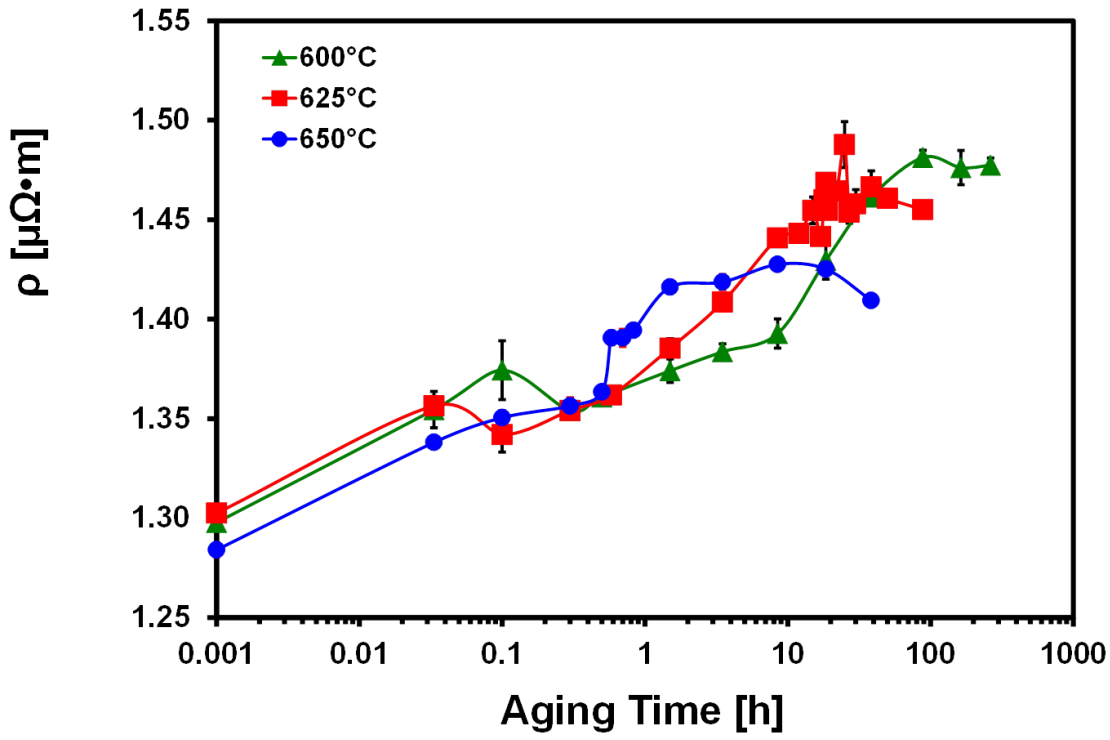

Figure 28: Electrical resistivity as a function of aging time for Waspaloy specimens heat treated at 600, 625, and 650°C

7.2 Johnson-Mehl-Avrami (JMA) Fitting

7.2.1 Electrical Resistivity

The electrical resistivity data for aging at 600, 625, and 650°C is given in Figure 28. The resistivity data displays the expected increase to a peak for all aging temperatures, with the peak shifting to lower resistivity and shorter aging times as the aging temperature is increased. This is the expected behavior due to the smaller precipitate volume fraction and faster kinetics expected at higher temperature.

The resistivities shown in Figure 28 were converted to relative resistivities (ρ_{rel}) using equation 9. The relative resistivity measures the increase in resistivity from that of the solution treated sample (ρ_{ST}) to that of the maximum in resistivity (ρ_{max}). The ρ_i values are the resistivity measurements made as a function of the aging time. The relative resistivity was fit with a JMA type equation, also given by equation 9. The k and n values from the JMA model have their normal meanings and are constant for a given aging temperature.

$$\rho_{rel} = \frac{\rho_i - \rho_{ST}}{\rho_{max} - \rho_{ST}} = 1 - exp\left[-(kt)^n\right] \tag{9}$$

The variable, n, in equation 9 is often obtained by rearranging the equation to that given by equation 10. By plotting the left-hand side of equation 10 against the natural logarithm of the aging time, the slope yields the variable n directly from the measured resistivities.

$$lnln\left(\frac{1}{1-\rho_{rel}}\right) = nlnt + nlnk \tag{10}$$

The only unknown from equation 9 is the rate constant, k. Therefore, the relative resistivity data at each aging temperature was fit to equation 9 employing non-linear least squares regression, using k as the sole fitting parameter. The relative resistivities along with their corresponding JMA fits are given by Figure 29. The excellent fit of the JMA model to the measured electrical resistivity data indicates that the JMA model is valid for predicting the electrical response of Waspaloy due to the nucleation of γ'.

7.2.2 Activation Energy

The k and n values used to fit the data in Figure 29 are given by Table 3. The k values have an Arrhenius type behavior given by equation 11, where R is the universal gas constant.

$$k = Aexp\left(-\frac{Q_{act}}{RT}\right) \tag{11}$$

The activation energy (Q_{act}) can thus be calculated from the slope of the natural logarithm of k with respect to the inverse of the absolute temperature (T). Such an Arrhenius type plot is given by Figure 30 for the k values listed in Table 3. The slope of the linear fit to the data was used to calculate an activation energy of 398 kJ/mol. The activation energy calculated from Figure 30 is similar in magnitude to that reported in the literature for nickel-base superalloys [3, 36, 44]. Rosen et al. [3] reported an activation energy of 250 kJ/mol for γ' precipitation in several wrought nickel-base superalloys. This activation energy was attributed to nickel self-diffusion being the dominant nucleation mechanism. The alloys used by Rosen et al. [3] were of a much simpler composition than the Waspaloy specimens used in this study. The fewer alloying elements used for those specimens could

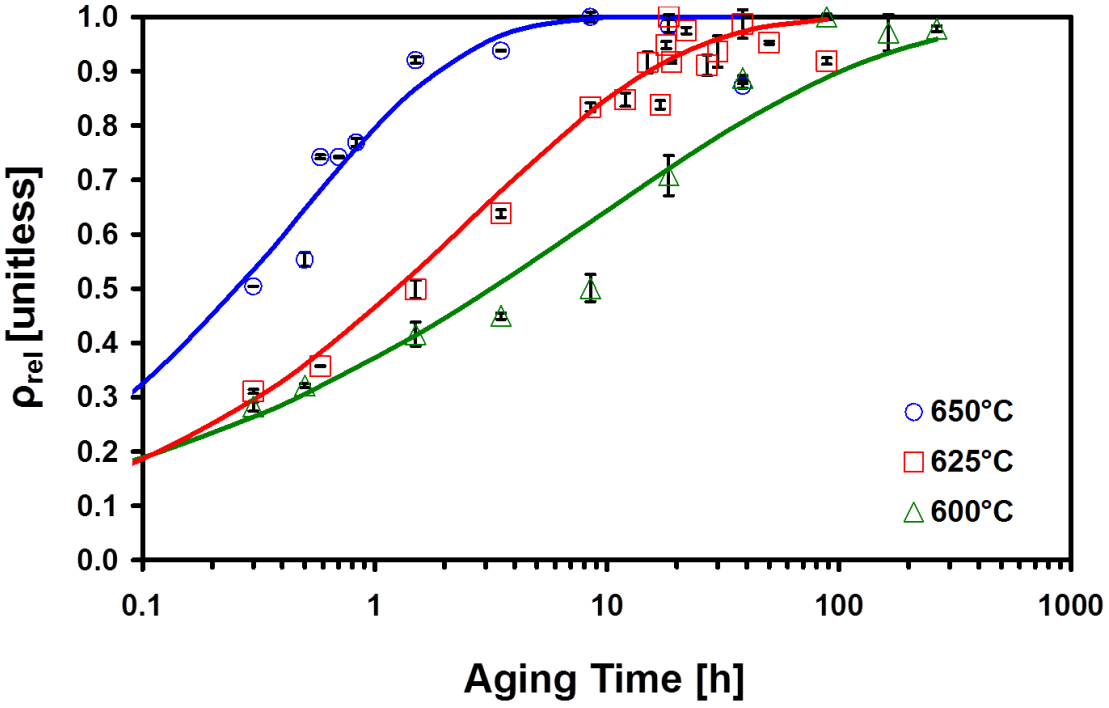

Figure 29: Relative resistivities calculated for Waspaloy specimens heat treated at 600, 625, and 650°C. The data are fit with a JMA model meant to describe the electrical response due to the initial nucleation of precipitates. The excellent fit of the model to the measured data is an indicator of the JMA model's potential for predicting changes to the precipitate microstructure via electrical resistivity testing.

Table 3: Fitted k and n values from JMA modeling of resistivity

Aging Temperature (°C)	$\boldsymbol{k}$ **(s^{-1})**	$\boldsymbol{n}$ **(unitless)**
600	3.03 X 10^{-5}	0.35
625	1.04 X 10^{-4}	0.48
650	5.93 X 10^{-4}	0.61

account for the lower activation energy than that reported here. It has been shown that the activation energy of nickel-base superalloys can vary with aging time, for example one study reported values ranging between 228 and 653 kJ/mol [44]. The activation energy calculated using the JMA model is well within this range, implying that the value obtained for these Waspaloy samples is reasonable.

7.3 Relationship between Resistivity and Volume Fraction

The integrated intensities of the XRD peaks were used as a metric for the evolving precipitate volume fraction during nucleation. The peaks were first fit using the Jade 9 software from Materials Data, Inc. [85], followed by normalization by the maximum peak intensity. These normalized intensities (I) were used along with equation 12 as a measure of the precipitate volume fraction relative to the value at the resistivity peak maximum ($f_{V,rel}$). In equation 12, I_i is the intensity at a given aging time, and I_∞ is the intensity at the maximum in resistivity.

$$f_{V,rel} = \frac{I_i}{I_\infty} \tag{12}$$

The behavior of ρ_{rel} and $f_{V,rel}$ with respect to aging time at 650°C is given by Figure 31. The resistivity and volume fraction both show similar trends with aging time; however, the relative resistivity is larger than the relative volume fraction in all cases. This was also noted by Ferragut et al. [60] for JMA fitting of 7012 aluminum. This implies that the resistivity and volume fraction are not linearly related for nucleation of γ' in Waspaloy. In fact, Lendvai et al. [59] reported a resistivity dependence of $f_V^{2/3}$ for nucleation of GP zones in an aluminum alloy. Such a dependence would account for the relative resistivity being larger than the relative volume fraction.

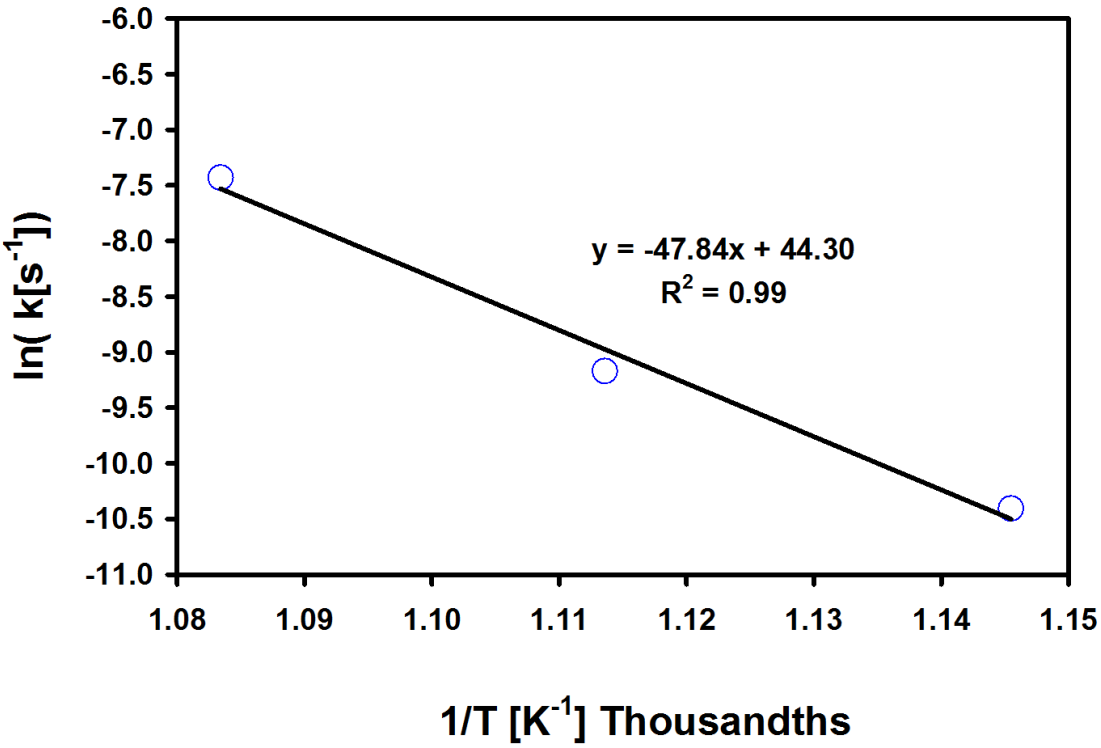

Figure 30: Arrhenius plot of the fitted k values from JMA modeling of the electrical response of Waspaloy. The specimens were heat treated at 600, 625, and 650°C. The activation energy for γ' nucleation was obtained from the slope of the linear fit to the data.

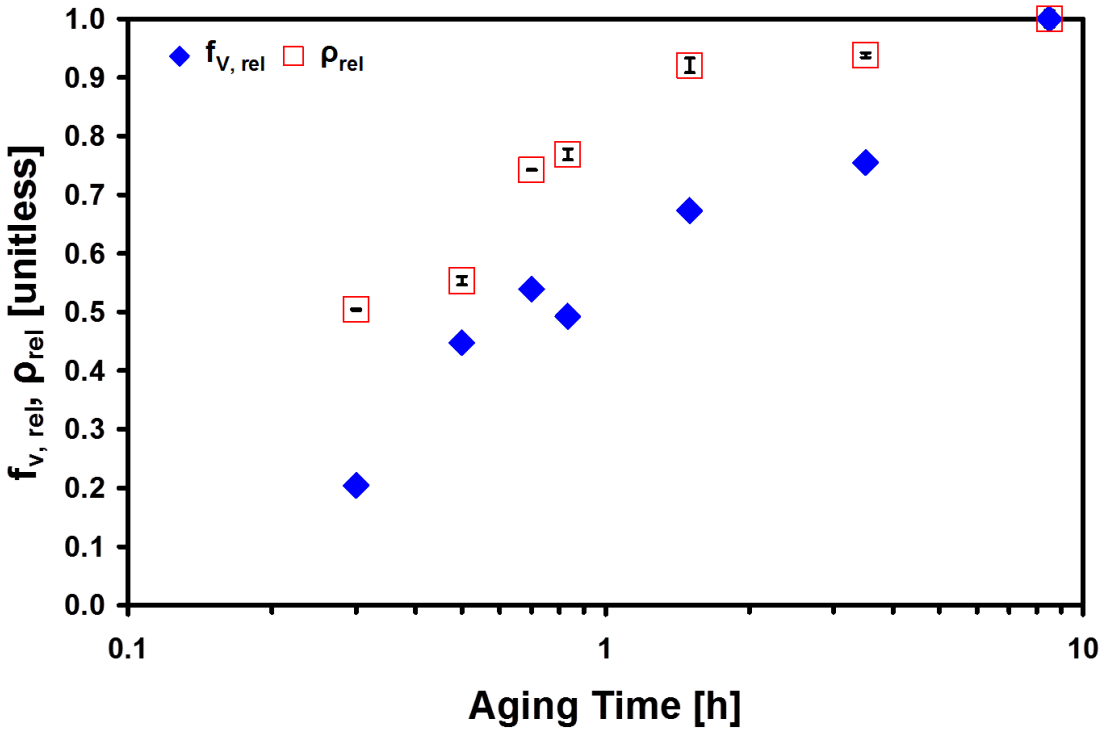

Figure 31: Relative resistivity and relative volume fraction of precipitates for Waspaloy specimens heat treated at 650°C. The resistivity values are larger than the volume fractions for all measured aging times.

7.4 Conclusions

The initial increase in electrical resistivity to a maximum has been successfully modeled with a JMA type equation for the nucleation of γ' in Waspaloy. An activation energy of 398 kJ/mol was calculated through the evolution of the fitted rate constants with temperature. The maximum in resistivity can be attributed to the increase in the volume fraction of nucleated precipitates in the initial stages of aging. The volume fraction increased similarly to the measured electrical resistivity; however, the relative resistivity was larger than the relative volume fraction for all aging times, implying that the correlation between resistivity and volume fraction is not linear. JMA fitting of the electrical response is useful for predicting the precipitation behavior in nickel-base superalloy specimens during the initial processing stages.

CHAPTER 8

RESISTIVITY DURING GROWTH AND COARSENING

In the previous chapter, the initial resistivity maximum due to γ' nucleation was modeled with a JMA type equation. This model showed an excellent fit to the measured data; however, the JMA model is only applicable to the initial nucleation of precipitates. For aging times past the resistivity peak, this model fails to accurately describe the electrical response due to the evolving precipitate microstructure. The eventual growth and coarsening of precipitates occurs well after the resistivity maximum. The mechanical properties of superalloys change drastically during the growth and coarsening stages, making it desirable to model the resistivity for these longer aging times as well.

In this chapter, electrical resistivity measurements were obtained for Waspaloy specimens cyclically heat treated at 725, 800, and 875°C for aging times ranging from 0.5h to 263.5h. The evolution in the precipitate microstructure was evaluated using SEM imaging and ultra-small angle X-ray scattering (USAXS). A microstructural model is presented that accounts for the effects of the evolving precipitate microstructure and matrix solute content on the measured electrical response. This model is especially useful in that it applies to the growth and coarsening stages of precipitation, rather than the nucleation regime only. In the next chapter, this model will be improved to better encompass the true precipitate microstructure in Waspaloy.

8.1 Microscopy

Microstructural images of the γ' phase are given by Figures 32 and 33. Figure 32 presents the progression in the precipitate microstructure with aging at 875°C for increasing aging times. The precipitates remain spherical throughout all aging times and display the expected increase in precipitate size and spacing as the aging time increases. Similar trends were noted for aging at the lower aging temperatures; however, as can be seen by Figure 33,

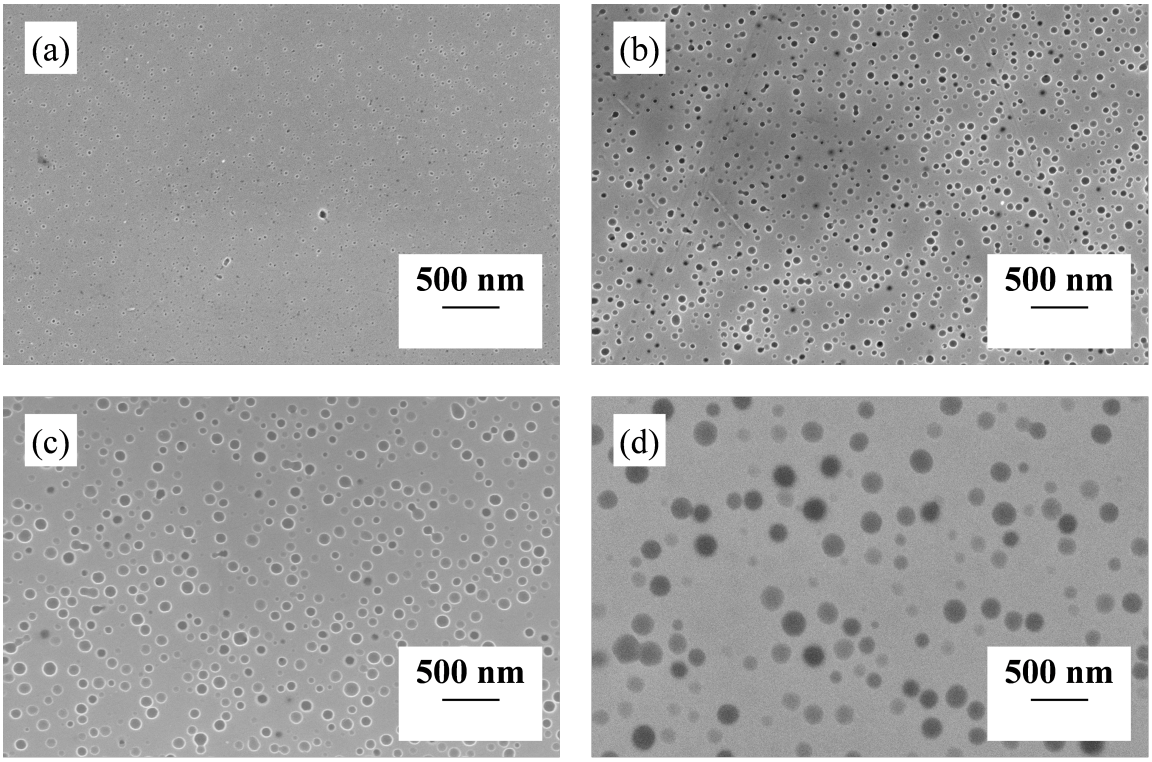

Figure 32: SEM images of the γ' precipitate microstructure in Waspaloy after heat treatment at 875°C for (a) 0.5h, (b) 3.5h, (c) 8.5h, and (d)263.5h respectively. The images show the expected increase in precipitate size and spacing with aging time.[9]

the kinetics of growth were much slower at lower temperature. Figure 33 displays the γ' evolution with temperature for specimens heat treated for 163.5h in all cases.

8.2 USAXS Measurements

8.2.1 USAXS Spectra

The evolution in the precipitate microstructure was quantified via USAXS measurements. A representative example of the USAXS spectra obtained for these specimens is given by Figure 34, whereby each subsequent aging time has been shifted upward in intensity for easier viewing. Figure 34 displays the expected scattering regions from superalloy specimens (see Section 2.4.2), and are designated as regions I, II, and III. Region I corresponds to scattering from carbides located at the grain boundaries, which are not the subject of the present study. Regions II and III correspond to scattering from the primary and secondary precipitate size populations respectively. Unlike the SANS measurements, the scattering

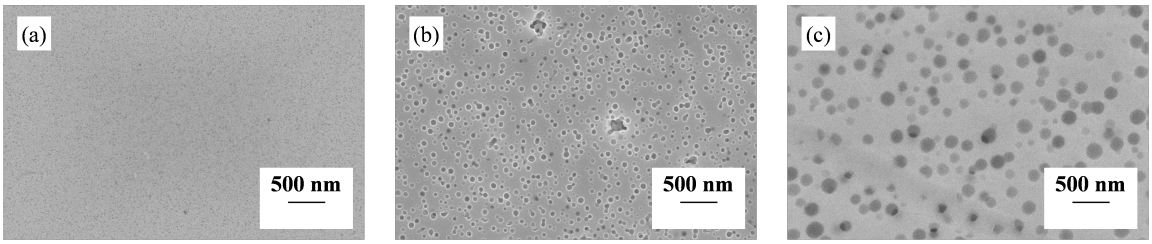

Figure 33: SEM images of the γ' precipitate microstructure in Waspaloy after heat treatment for 163.5h at (a) 725°C, (b) 800°C, and (c) 875°C respectively. The images show the expected increase in precipitate size with aging temperature.[9]

regions from γ' are Debye regions in all cases, whereby the intensity decreases with Q^{-n} dependence.

At the lowest aging times, the USAXS data shows a single distribution of precipitates in all cases. This is as evidenced by the sample aged for 0.5h in Figure 34. This primary precipitate population shifts to progressively lower Q as the aging time increases. Such a progression is indicative of the increasing precipitate size with aging. Continued aging resulted in the formation of a secondary precipitate size population, denoted as region III in Figure 34.

8.2.2 Microstructural Evolution

The USAXS spectra, like those shown in Figure 34, were fit with a volume distribution of spherical particles. The particle size distributions (PSD's) obtained from such data fitting are given in Figure 35. The data show a shift to a bimodal distribution for every aging temperature, but the aging time required to induce this secondary population increased with decreasing aging temperature. The primary precipitate size population shifts to larger diameters and broadens significantly with aging time. This is typical of precipitate coarsening. The secondary precipitate population does not progressively shift to larger diameters with time, as does the primary population. Instead, the sizes for the secondary phase appear to change in a more erratic fashion.

Of particular interest from the PSD's shown in Figure 35 are the average precipitate radius ($\langle r \rangle$) and the volume fraction (f_V). This data is presented by Figures 36 and 37 respectively. Multiple USAXS measurements were obtained for each sample, allowing for a

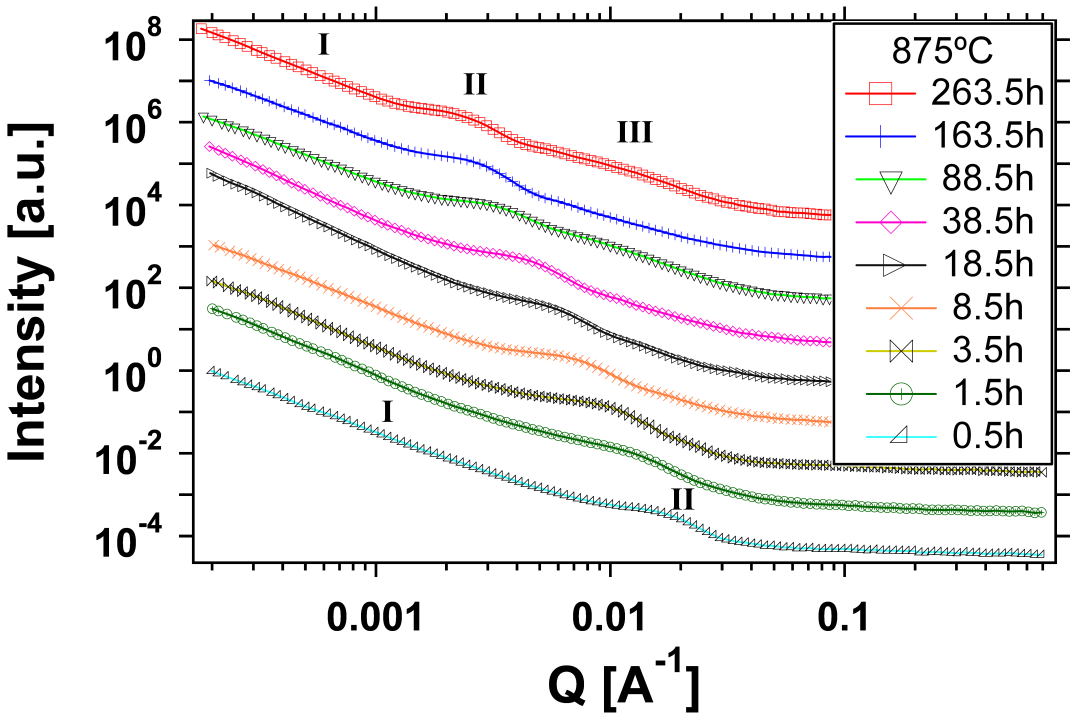

Figure 34: USAXS spectra for Waspaloy specimens cumulatively heat treated at 875°C for increasing aging times. Each aging time has been shifted in intensity to increase the readability of the data. Regions I, II, and III denote scattering due to carbides, the primary precipitate size population, and the secondary precipitate size population respectively. [9]

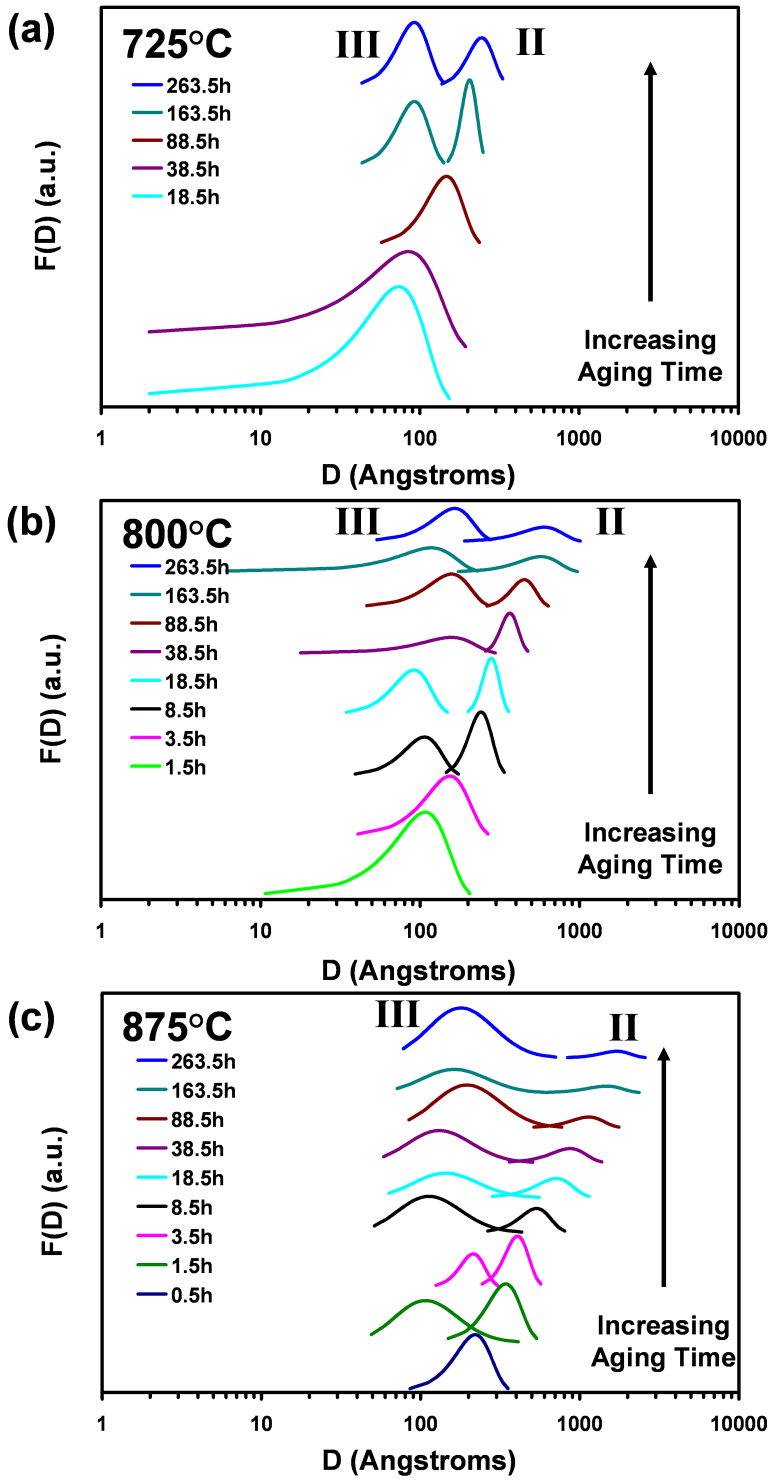

Figure 35: Volume distributions of the γ' phase in Waspaloy, as obtained by USAXS data fitting. Regions II and III denote the primary and secondary precipitate size populations noted from the USAXS data. [9]

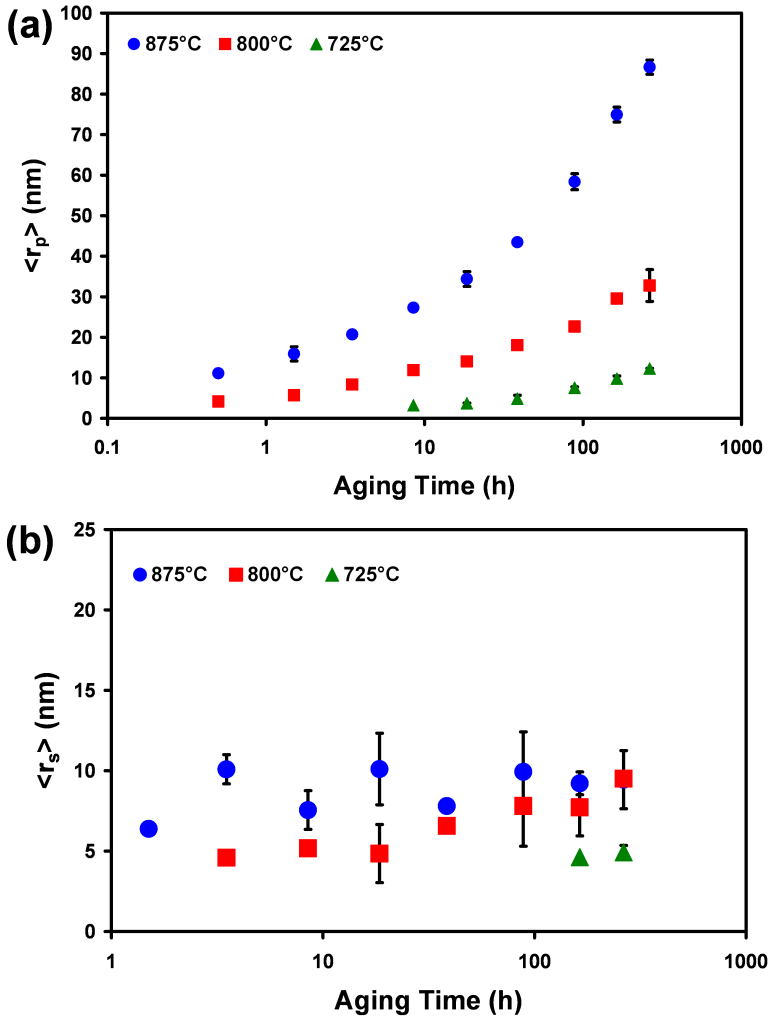

Figure 36: Average precipitate radii for the (a) primary and (b) secondary precipitate populations for Waspaloy specimens heat treated at 725, 800, and 875°C [9]

statistical average of the microstructural parameters to be calculated. These averages and standard deviations correspond to the data markers and error bars shown in Figures 36 - 39.

The average primary radius ($\langle r_p \rangle$) and the average secondary radius ($\langle r_s \rangle$) as a function of aging time are given by Figure 36. There is a clear progressive increase in $\langle r_p \rangle$ with both time and temperature in all cases. This is similar to the evolution in the γ' microstructure noted from Figures 32 and 33. The $\langle r_s \rangle$ data shows an increasing trend with aging time, but with a high degree of scatter and with larger standard deviations than that measured for $\langle r_p \rangle$.

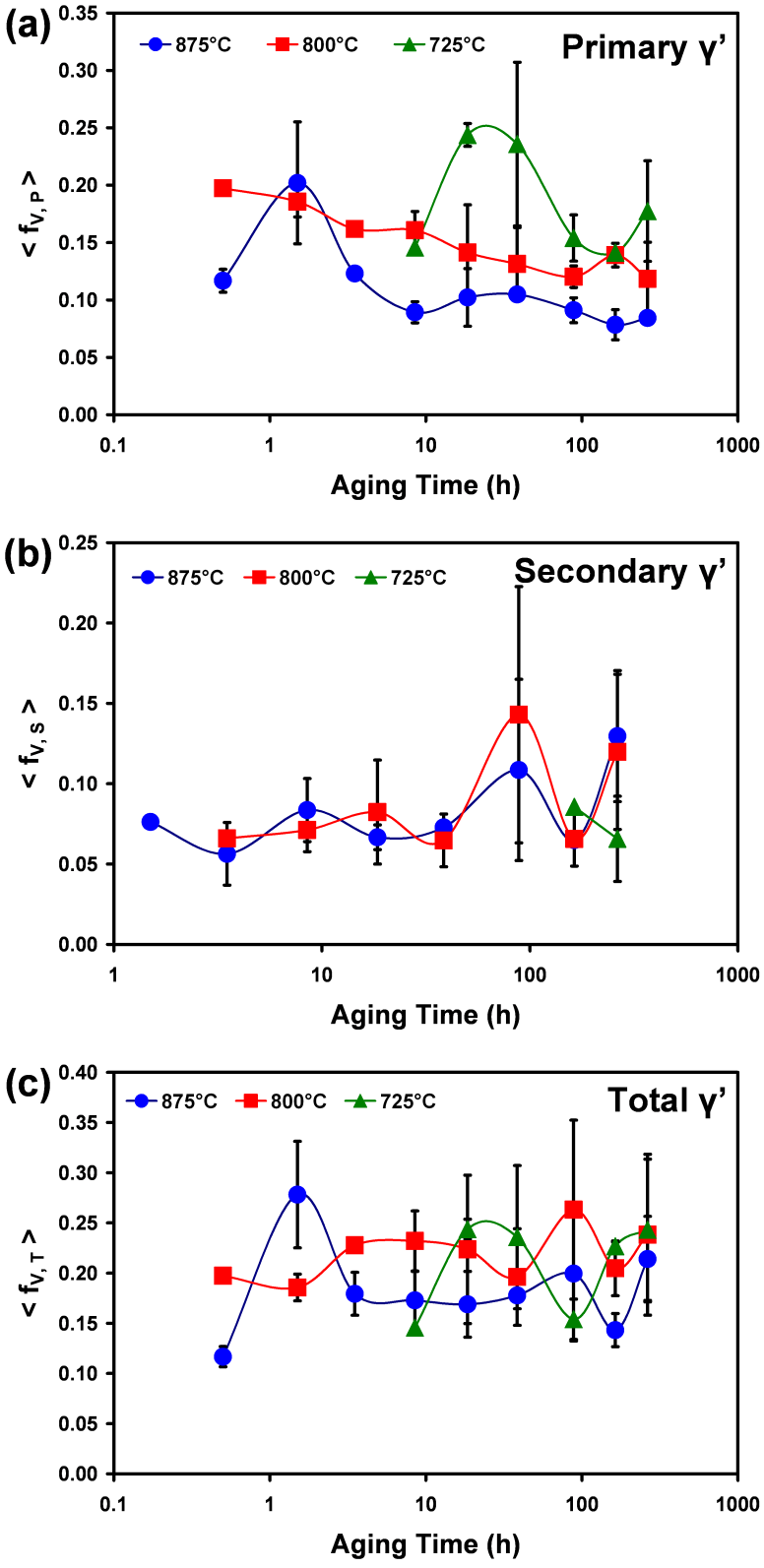

Figure 37: Volume fractions of the γ' phase in Waspaloy corresponding to the (a) primary, (b) secondary, and (c) total precipitate population for specimens aged at 725, 800, and 875°C [9]

The average over multiple USAXS runs for f_V is given by Figure 37. The subscripts P, S, and T refer to the volume fractions of the primary, secondary, and total precipitate populations respectively. The average primary precipitate volume fraction ($\langle f_{V,P} \rangle$) reaches a peak followed by a decreasing trend for aging at 725°C and 875°C. These peaks occur at 18.5h and 1.5h respectively, and are most likely due to the primary phase reaching the equilibrium volume fraction. The decrease in $\langle f_{V,P} \rangle$ after the maximum can be explained by the smallest precipitates from the primary distribution joining with the largest precipitates from the secondary distribution. The 800°C data does not show a peak for $f_{V,P}$; however, a large standard deviation is noted for the sample aged for 1.5h. It is possible that this indicates a peak in the data, with the true volume fraction lying below that calculated from USAXS measurements. Furthermore, Kelekanjeri et al. [7] noted a peak in the primary volume fraction for Waspaloy specimens heat treated at 800°C. These specimens were given a vacancy stabilization treatment in addition to the solution treatment and aging treatment, so those samples were not subject to the exact same processing conditions as the samples used in this study. Nevertheless, it is evidence of a possible peak location at 1.5h for the specimens heat treated at 800°C.

The average secondary precipitate volume fraction ($\langle f_{V,S} \rangle$) behaves quite differently than $\langle f_{V,P} \rangle$, with $\langle f_{V,S} \rangle$ showing a fluctuating behavior throughout all aging times. The $\langle f_{V,S} \rangle$ values also appear to be temperature independent, with the data points corresponding to varying temperature occurring well within the error bars for each aging time. It is believed that the secondary precipitate phase is due to the cyclic heating schedule used for these experiments. Samples at each aging time would be exposed to the same number of ramp-up cycles regardless of the aging temperature. This would account for the temperature independence of $\langle f_{V,S} \rangle$.

The average total precipitate volume fraction ($\langle f_{V,T} \rangle$) displays both the peaked behavior of $\langle f_{V,P} \rangle$ and the eventual fluctuating behavior noted in $\langle f_{V,S} \rangle$. In the case of $\langle f_{V,T} \rangle$, the 800°C data set also displays a peak, with the peaks occurring after 18.5, 8.5, and 1.5h at 725, 800, and 875°C respectively.

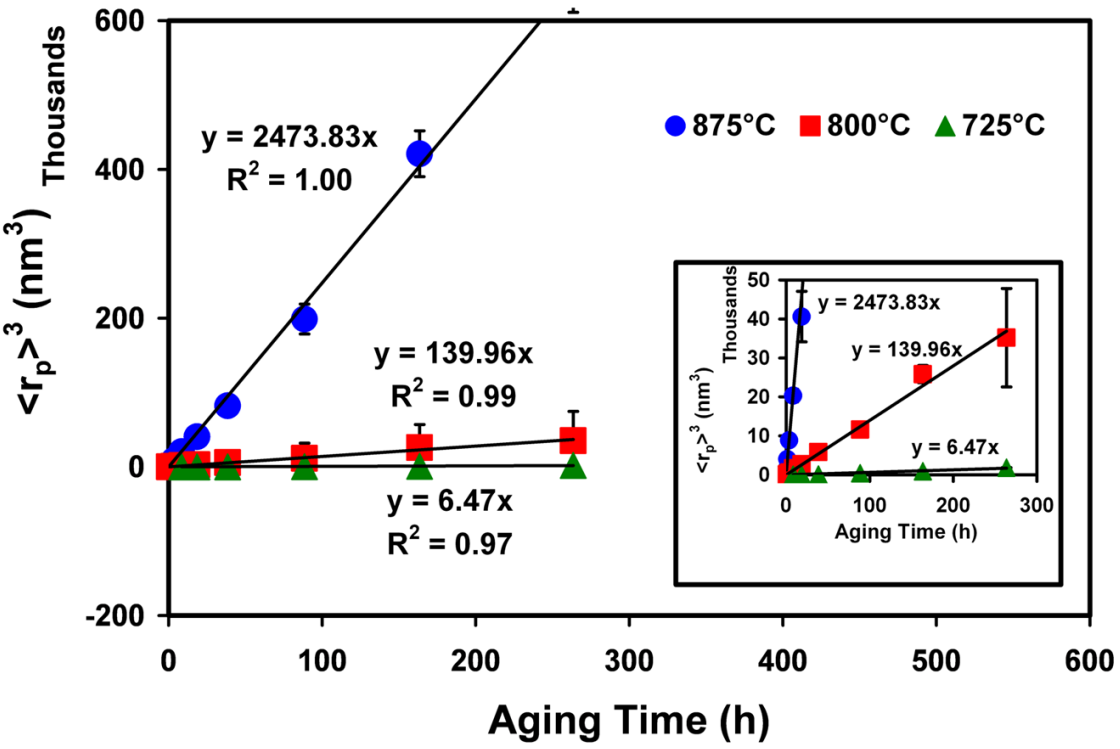

Figure 38: Coarsening plots for the primary γ' precipitates in Waspaloy specimens heat treated at 725, 800, and 875°C with linear fits to the data. The inset better displays the increasing slopes (coarsening rate constants) with increasing temperature. [9]

8.2.3 Growth and Coarsening Behavior

The coarsening plots for the average primary precipitate radius, $\langle r_p \rangle$, are given by Figure 38 as a plot of $\langle r_p \rangle^3$ versus the aging time. The inset of Figure 38 better displays the increasing slopes of the data with temperature, indicating the increase in the coarsening rate constants. No growth or coarsening response was noted for the secondary precipitate population.

While the linear fits to the coarsening data indicate a $t^{1/3}$ dependence for the precipitate radii, it should be noted that the 725°C data set displays a less ideal fit to the data. A plot of the natural logarithm of the radius with respect to the natural logarithm of the aging time is more indicative of the true temporal power law exponent. Such a plot is given in Figure 39 for aging at all three measured temperatures. Figure 39 indicates that the precipitates are within the diffusion controlled coarsening regime throughout all aging

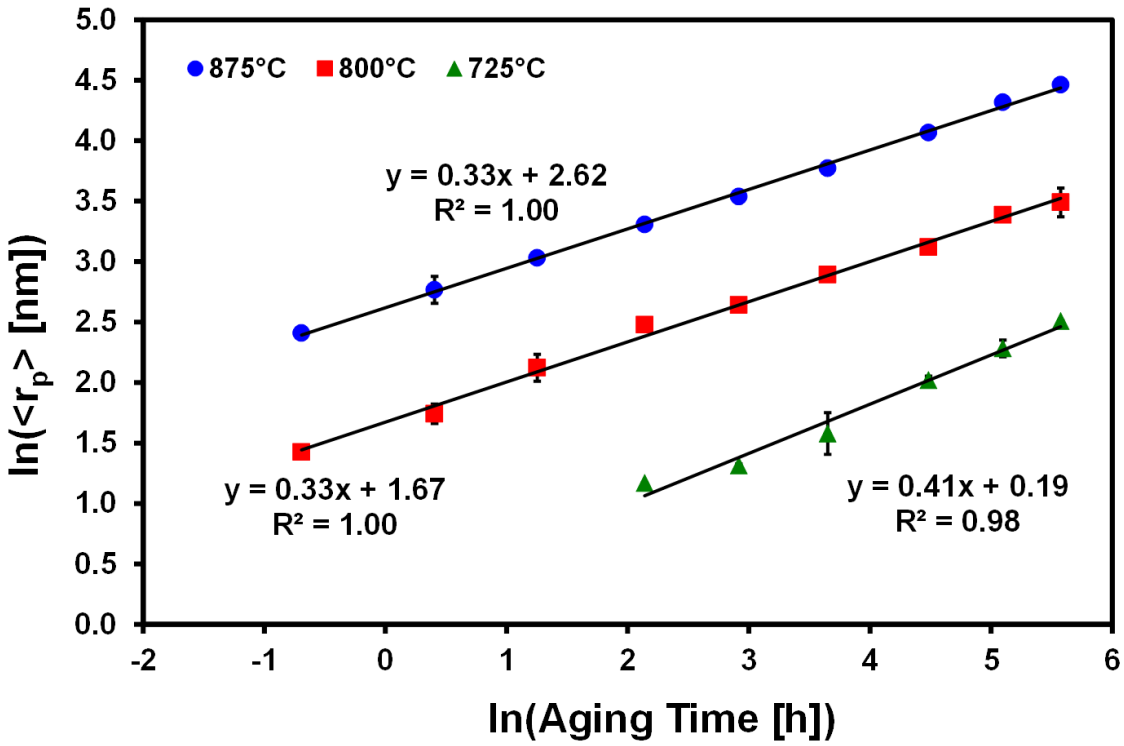

Figure 39: Plot of the natural logarithm of the average primary radius with respect to the natural logarithm of the aging time for specimens aged at 725, 800, and 875°C. The slopes of the linear fits yield the temporal power law exponent describing the precipitation regime (growth or coarsening) for each particular aging temperature. The data indicates diffusion controlled coarsening for the 800°C and 875°C data sets and a mixed mode of growth and coarsening at 725°C.

times for the samples heat treated at 800°C and 875°C. Heat treatment at 725°C resulted in a $t^{0.41}$ temporal power law, indicating a mixed mode of growth and coarsening. This would explain the lower R^2 value for the linear fit to the 725°C data set from Figure 38.

8.3 Electrical Response

The previous sections presented the evolution in the precipitate microstructure due to cyclic heat treatment. This section will describe the effects of this evolving precipitate microstructure on the measured electrical response. The electrical resistivity due to aging at 725, 800, and 875°C is given by Figure 40. The data in Figure 40 displays the expected initial increase to a maximum, excepting the case of the 875°C data set, whereby the faster kinetics prevented sampling of this region. The data then displays the expected decrease in resistivity,

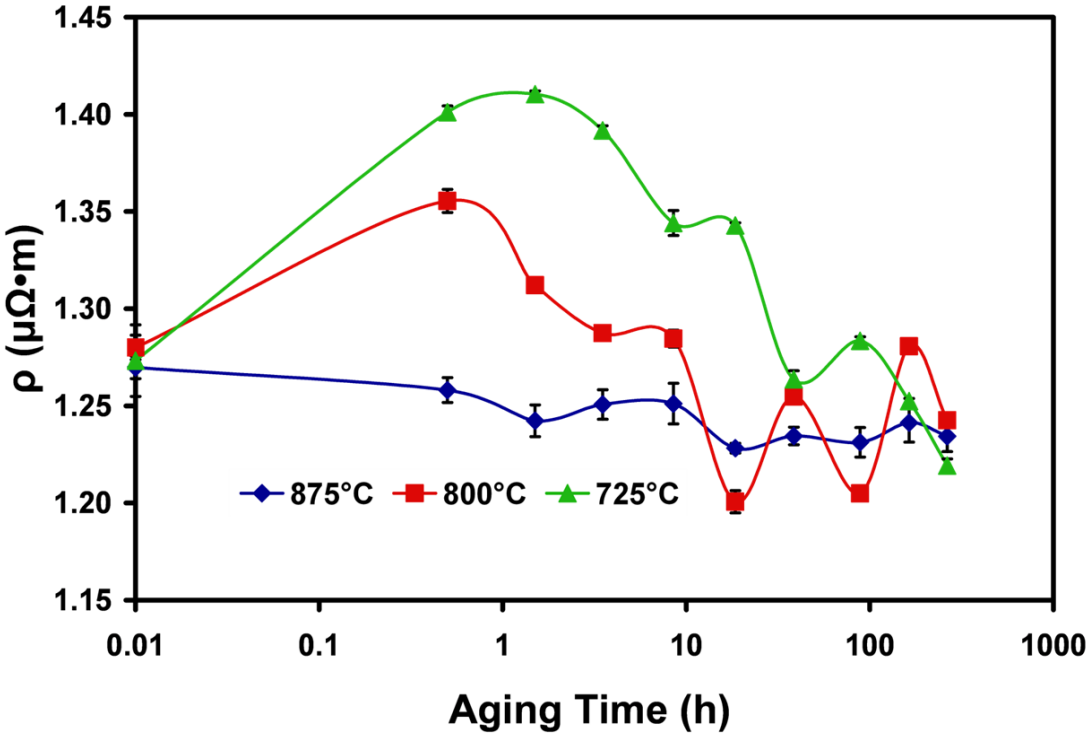

Figure 40: Measured electrical resistivity as a function of aging time for Waspaloy specimens heat treated at 725, 800, and 875°C. [9]

followed by a fluctuating behavior. This fluctuating resistivity behavior is similar to the fluctuating behavior noted in the secondary precipitate volume fraction shown in Figure 37. It is believed that the secondary precipitate phase is thus responsible for the fluctuating resistivity behavior noted in Figure 40. The secondary precipitates were of much smaller size than the primary precipitates in all cases (see Figure 36). The formation and dissolution of this phase would result in a corresponding increase and decrease in conduction electron scattering from precipitates, giving rise to the fluctuating resistivity behavior.

The resistivity regions shown in Figure 40 are expected due to cyclic heat treatment of Waspaloy specimens (see Chapter 6). These trends arise from the competing mechanisms of conduction electron scattering from precipitates and solute atoms. In order to use electrical resistivity to monitor the γ' phase, the effects of the precipitate microstructure on the electrical response must be quantified.

8.4 Modeling Electron Scattering from Precipitates

The original work towards modeling the electrical response of Waspaloy due to the evolving γ' microstructure was performed by Kelekanjeri et al. [7]. Kelekanjeri et al. [7] proposed a "figure of merit" designed to model the conduction electron scattering capability of the evolving precipitate microstructure with heat treatment. In that paper, the figure of merit was designated as η, but for the purposes of this project, this term will be designated as η_g, as it models the changes to the precipitate geometry only. The original formulation for η_g is given by equation 13 [7], with the summation performed over each size distribution of precipitates.

$$\eta_g = \frac{S_V}{\Delta} = 3.33 \sum \frac{f_V^{4/3}}{\langle r \rangle^2} \tag{13}$$

Equation 13 states that the extent of conduction electron scattering from precipitates should be both directly proportional to the precipitate surface area per unit volume (S_V) and indirectly proportional to the precipitate nearest neighbor distance (Δ). As S_V increases, the probability of a conduction electron colliding with a precipitate will also increase. Conversely, as Δ increases, the probability of a conduction electron colliding with a precipitate will decrease, due to an increase in the mean free path. The formulation given by Equation 13 is thus reasonable for predicting conduction electron scattering from precipitates only. In order to derive the right-most side of equation 13, the following assumptions were made:

1. The precipitates are assumed to be spherical.
2. The nearest neighbor distance is assumed to be that of a distribution of point particles in an infinite volume.
3. The precipitates are assumed to all have the average size, $\langle r \rangle$.

The first assumption is accurate for Waspaloy, as it has been shown that the γ' phase is predominantly spherical; however, this is not always the case for superalloy specimens, which can take on a variety of morphologies [37]. Assumption 2 is an oversimplification, since the

precipitates are of finite size. Assumption 3 is also not accurate, since the precipitates have a distribution of particle sizes, as can be seen by Figure 35.

However, this model provided the first simplified version that allowed fitting the precipitate microstructure to the electrical resistivity in Waspaloy [7]. If these assumptions are assumed to hold, then the nearest neighbor distance for a distribution of point particles is given by equation 14, where N_V is the number density of precipitates [87].

$$\Delta = 0.554 N_V^{-1/3} \tag{14}$$

For a microstructure where all precipitates have the average size, S_V is given by equation 15. Equations 14 and 15 are thus used to formulate η_g.

$$S_V = 4\pi N_V \langle r \rangle^2 = \frac{3 f_V}{\langle r \rangle} \tag{15}$$

Kelekanjeri et al. [7] noted a generic similarity between the measured electrical resistivity and η_g for Waspaloy specimens heat treated at 800°C for short aging times. At the longer aging times, η_g ceased to model the electrical response. The changing solute content of the matrix phase was not included in η_g. At the lowest aging times, a negligible amount of solute would be removed from the matrix, which would account for the similarity noted between η_g and the resistivity in this region. At longer aging times, the solute content of the matrix cannot be ignored and will evolve concurrently with the geometry of the precipitate phase. This would explain the failure of η_g to model the resistivity at the longest aging times. The next section will introduce a compositional term than can be added to η_g to model both conduction electron scattering from precipitates and solute atoms.

8.5 Modeling Electron Scattering from Solute Atoms

In this section, a compositional term (η_c) is presented that is designed to model the effects of conduction electron scattering from solute atoms. The matrix phase of Waspaloy is a solid solution containing all of the alloying elements in the bulk material. As the precipitate volume fraction increases, the precipitate forming elements are selectively removed from solution in the matrix phase - effectively reducing the solute content of the matrix. By

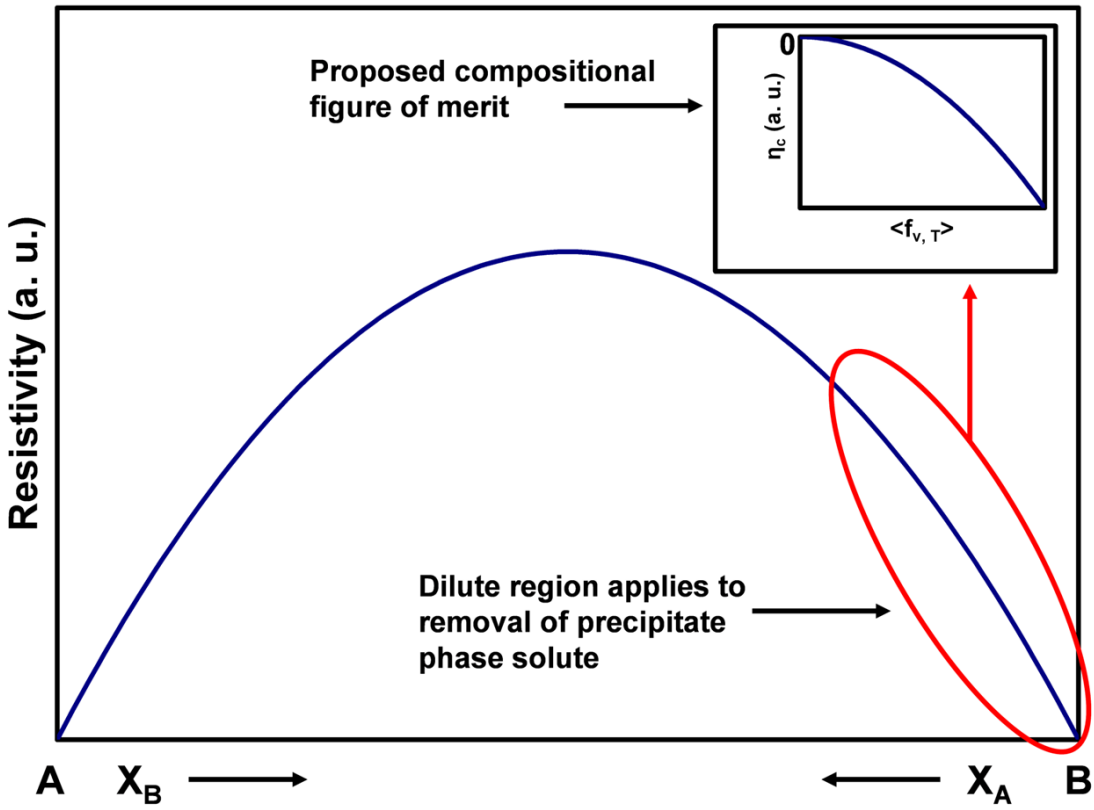

Figure 41: Schematic of the expected electrical response of a hypothetical A-B alloy in complete solid solution. It is expected that pure metals will be the least resistive, with the resistivity increasing as either solute is added. The inset displays the proposed response of a compositional figure of merit designed to correlate conduction electron scattering from solute atoms to the precipitate volume fraction. [9]

Matthiessen's rule, it is expected that purer metals will have lower resistivities [12]. The expected electrical response of a hypothetical A-B alloy in complete solid solution is given by Figure 41, whereby the resistivity is lowest for the pure metals and is larger as either solute is added to the solution.

Waspaloy is not a binary alloy, as schematically depicted in Figure 41. Instead, the composition of the matrix phase will be complex, containing over ten alloying elements - all of which partition into the precipitate phase with aging [29, 30]. The precipitate volume fraction is a more microstructurally relevant parameter to model the electrical response with, as changes to the matrix composition arise from the drawing of these elements into the γ' phase. The expected changes to the electrical behavior of the matrix phase should mirror what is presented in the inset of Figure 41, where η_c is plotted against the total

volume fraction. When all solutes are in solution ($f_{V,T} = 0$), there should be a maximum in compositional type scattering events in the matrix. As $f_{V,T}$ increases, the extent of compositional type scattering events should decrease due to solute removal from the matrix. By Nordheim's rule, the resistivity behavior like that shown in Figure 41 can be treated parabolically with composition [12]. Therefore, a first estimate for η_c is given by equation 16.

$$\eta_c = -C f_{V,T}^2 \tag{16}$$

In equation 16, C is a positive fitting constant that depends on the aging temperature. The partitioning ratios of the elements in the γ' precipitates will vary with temperature, resulting in different compositional dependence on volume fraction at each aging temperature. The compositional term is negative as it acts to detract from conduction electron scattering as the precipitate volume fraction increases. The total microstructural model for the electrical response will involve the competing mechanisms of conduction electron scattering from precipitates and solute atoms. This model for the electrical response of aged Waspaloy is given by equation 17.

$$\eta' = \eta_g + \eta_c = 3.33 \sum \left(\frac{f_V^{4/3}}{\langle r \rangle^2} \right) - C f_{V,T}^2 \tag{17}$$

In equation 17, η_g will be dominant when the precipitates are small and the volume fraction is low. This occurs at the lowest aging times, where Kelekanjeri et al. [7] noted a generic correlation between η_g and the measured resistivity. The η_c term becomes more dominant for large volume fractions, which occur at the longer aging times. Therefore, equation 17 should be able to model the electrical response of Waspaloy throughout all relevant aging times.

The microstructural information obtained from USAXS data fitting (presented in Figures 37 and 36) was used in equation 17 to calculate η'. The constant C was iteratively varied to yield the best fit to the measured electrical resistivity shown in Figure 40. The evolution of this microstructural model with aging time is compared to the measured electrical response via Figure 42. It is apparent that η' more closely matches the measured

electrical response over a wider range of aging times and temperatures than does η_g alone. The addition of the compositional term to the previous figure of merit, thus results in a better simulation of the true electrical response of Waspaloy specimens.

8.6 Conclusions

The γ' precipitate microstructure displayed a transition from a unimodal to a bimodal distribution upon cyclic heat treatment at 725, 800, and 875°C. The primary population of precipitates behaved as expected with aging time, whereby the distributions shifted to larger precipitate size and broadened significantly. It was determined that the precipitates were in the diffusion controlled coarsening regime for heat treatment at 800°C and 875°C; however, a mixed mode of growth and coarsening was noted upon heat treatment at 725°C. The secondary precipitate population did not show a progressive increase to larger sizes as aging time increased. The USAXS-derived precipitate volume fraction showed that this secondary population fluctuated in and out of solution with aging time, most likely due to the cyclic heating schedule used for these specimens. This cyclic behavior was evidenced in the electrical resistivity as well, implying that the formation and dissolution of this secondary population resulted in significant changes to the electrical response with cyclic heat treatment.

A microstructural model was presented that accounts for conduction electron scattering from precipitates and solute atoms. This model showed empirical correlations with the measured electrical response over a wider range of aging times and temperatures than modeling due to precipitates alone. This model shows promise for non-destructively obtaining the precipitate microstructure from the electrical response of Waspaloy; however, the model must be refined to better encompass the true precipitate microstructure. The following chapter will discuss improvements to the model presented here to yield better fits to the measured electrical response due to precipitation.

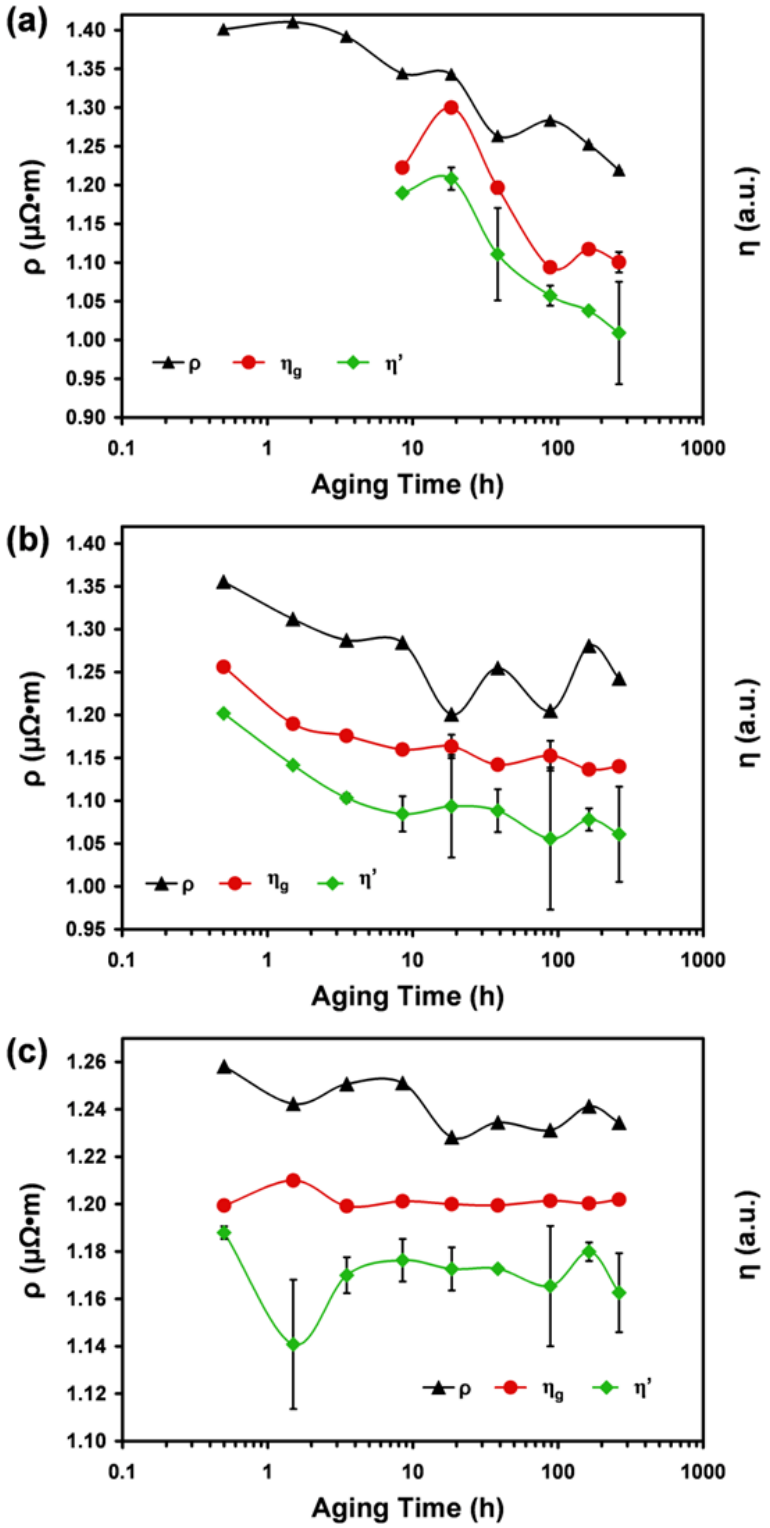

Figure 42: Evolution in both a microstructural model for the electrical response (η') and the true measured electrical response upon aging at (a) 725°C, (b) 800°C, and (c) 875°C. It can be seen that η' more closely matches the resistivity than does η_g alone. [9]

CHAPTER 9

IMPROVEMENTS TO MICROSTRUCTURAL MODEL

As seen by Figure 42 in the previous chapter, the addition of the compositional modeling term (η_c) to the original precipitate geometry term (η_g) results in a more accurate model for the electrical response due to precipitation in Waspaloy. In this chapter, η_c is refined to more accurately reflect the true Waspaloy microstructure. In addition, η_g is also revised so that it does not rely on the assumptions that the precipitates are point particles and are of the average size. The data is first fit using the improved compositional term only, followed by fitting using both improved terms.

The specimens examined in this section are Waspaloy samples exposed to non-cyclic heat treatment at 725°C and 800°C for times ranging from 2min to 263.5h. SEM and small angle scattering (SAS) were used to characterize the precipitate microstructure. The use of non-cyclic heat treatment allows for smoother resistivity trends to be obtained, as the secondary precipitate size population does not form under these conditions [11]. The lack of this secondary phase, also allows for the use of the more penetrating small angle neutron scattering (SANS) measurements, as opposed to the USAXS measurements used in the previous section. SANS measurements are more statistically significant than USAXS measurements and should give better data for the primary precipitate phase population (see Chapter 4).

9.1 Microscopy

The evolution in the precipitate microstructure due to non-cyclic heat treatment at 800°C is given by Figure 43. The γ' precipitates increase in size with aging time, as would be expected; however, the smaller secondary precipitate size population is not present in these specimens. These specimens were also given a preferential matrix etchant [6], causing the precipitates to appear as upraised spheres in Figure 43.

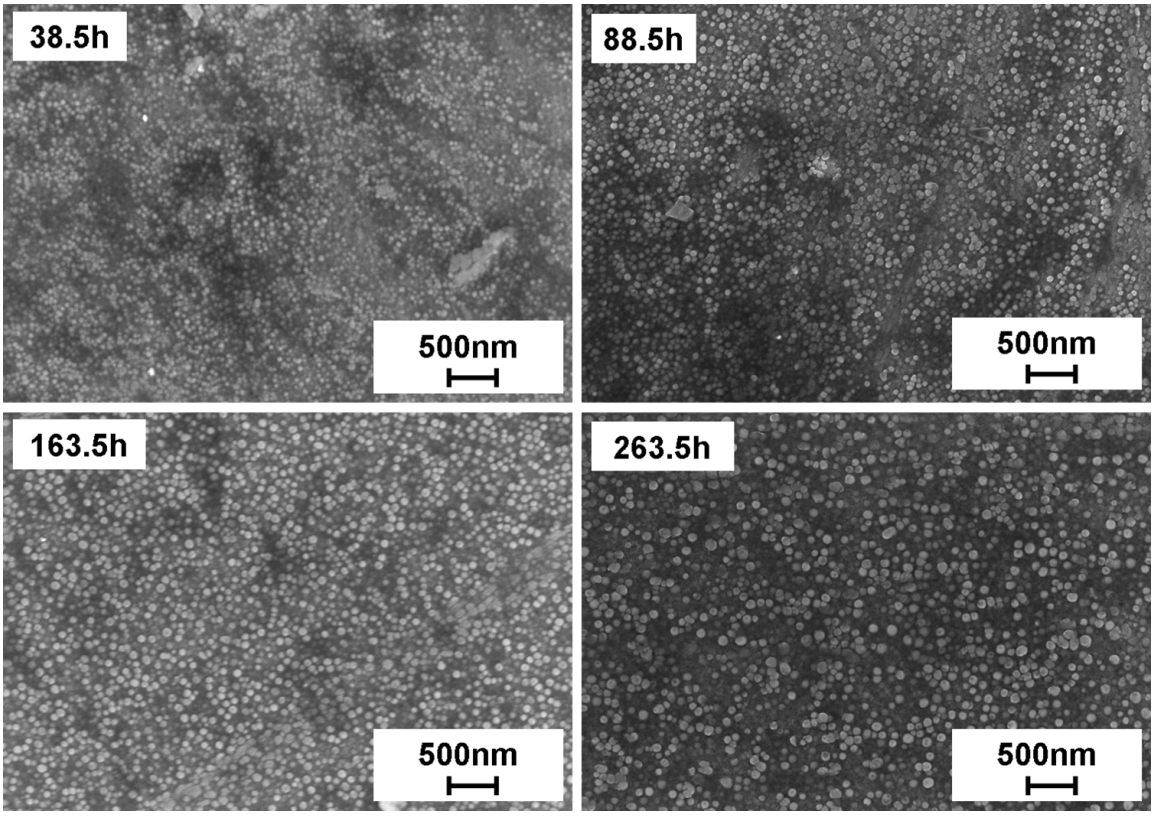

Figure 43: SEM images of the evolving γ' microstructure in Waspaloy due to non-cyclic heat treatment at 800°C. The single precipitate size population increases in size with aging time, as would be expected.

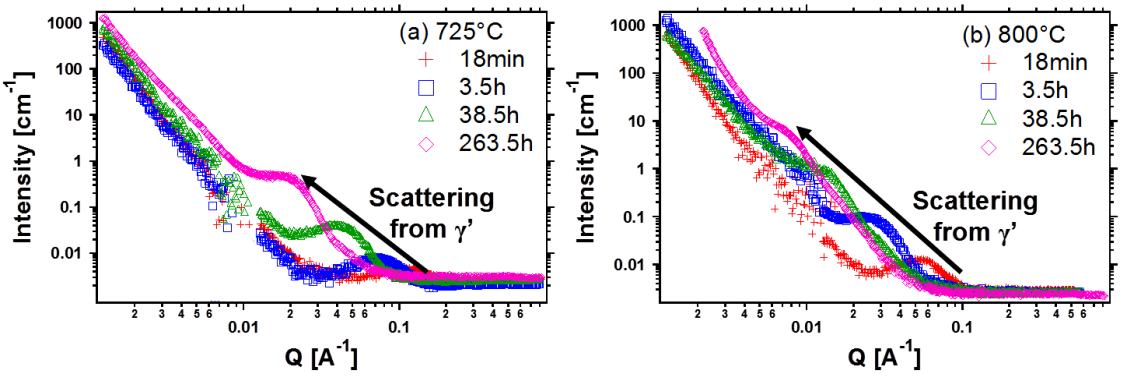

Figure 44: Selected SANS spectra for Waspaloy specimens non-cyclically heat treated at (a)725°C and (b) 800°C. The shift in the γ' scattering region is indicated with arrows. [11]

9.2 SANS Measurements

9.2.1 SANS Spectra

SANS spectra were obtained for the specimens heat treated at 725°C and 800°C and are given by Figure 44. Only selected aging times are included on Figure 44, so that the data remains readable. The SANS spectra show the expected scattering region at low Q from the carbides located at the grain boundaries. The γ' scattering region is at higher Q and shifts to progressively lower Q with aging time due to the increasing precipitate size. The γ' scattering region is a correlation peak due to the much thicker samples as compared to USAXS. Consequently, the probability of interparticle scattering increases as the samples become thicker (see Chapter 4) [28]. The correlation peak begins to evolve into a Debye region, similar to that seen by USAXS, with aging time due to the increase in precipitate spacing.

9.2.2 Microstructural Data from SANS

The SANS spectra were fit with a volume distribution of particle scatterers in all cases. The evolution of these particle size distributions with time and temperature may be seen in Figure 45, whereby each aging time has been shifted upwards. The SANS data for aging at 725°C for 2min and 6min did not display significant scattering from the γ' precipitates; therefore, there is no microstructural data available for these two specimens.

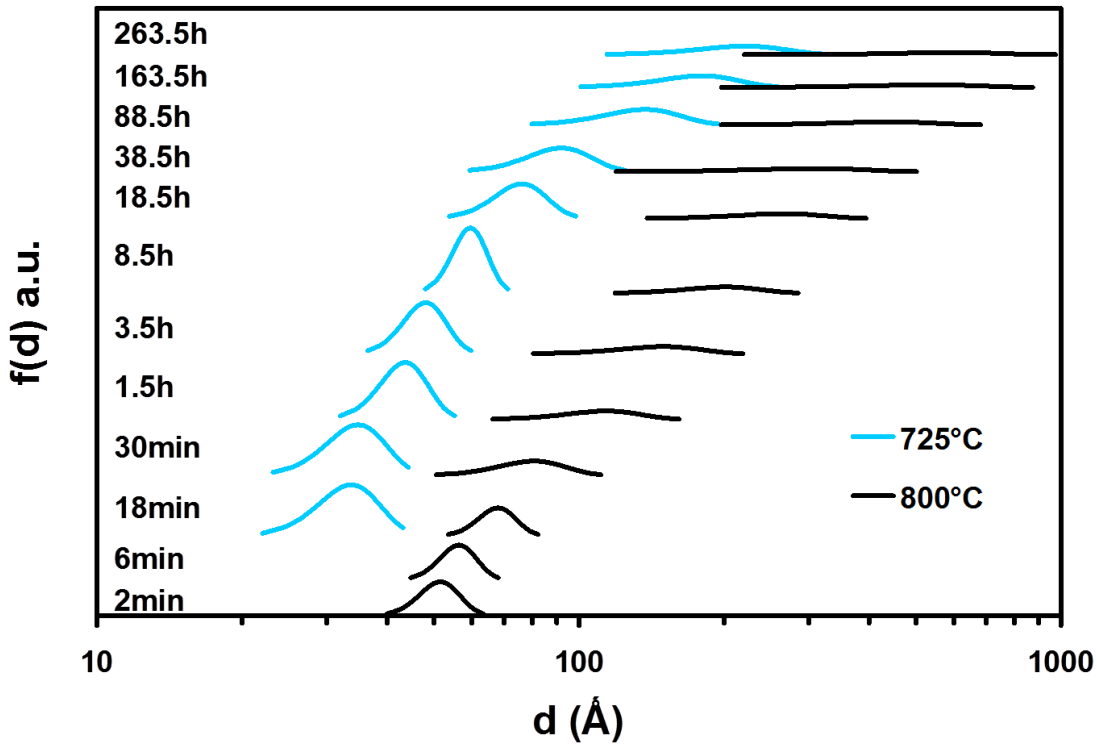

Figure 45: Particle size distributions of the γ' phase for Waspaloy specimens non-cyclically heat treated at 725°C and 800°C [11]

For both aging temperatures, a single precipitate size population is obtained from the SANS fitting, due to the use of non-cyclic heat treatment. The initial distributions are very narrow, and they shift to larger diameters and broaden significantly as aging continues. This evolution in the PSD's is commonly seen for precipitate coarsening. The PSD's upon aging at 800°C are shifted to larger diameters than for those heat treated at 725°C in all cases. The faster rate of diffusion at the higher aging temperature gives rise to these larger precipitates.

The evolution in the average precipitate radius can be seen by Figure 46. Only single scattering runs were performed for this set of experiments, so the standard deviation of the fitted volume distributions were used for the error bars of Figure 46. As Figure 46(a) shows, the average radii increase smoothly with both time and temperature, similarly to the primary precipitate population from cyclic heat treatment shown by Figure 36(a). The coarsening behavior of this single precipitate size population can be seen in Figure 46(b), where the data seems to indicate $t^{1/3}$ dependence for the growth of the radii at both temperatures. A plot of the natural logarithms of the radius versus the aging time revealed $t^{1/3}$ dependence for aging at 800°C and $t^{0.39}$ dependence at 725°C. This can be compared with the $t^{1/3}$ and $t^{0.41}$ dependence noted for cyclic heat treatment at 800°C and 725°C respectively. The data thus suggests diffusion controlled coarsening and mixed growth and coarsening at 800°C and 725°C regardless of the use of cyclic versus non-cyclic heat treatment.

9.3 Electrical Resistivity

The electrical response due to non-cyclic heat treatment at 725°C and 800°C is given by Figure 47, where the data points at 0.001h represent the solution treated specimens. The resistivity displays the expected initial maximum followed by the slower decrease with aging time; however, the resistivity trends are much smoother than those observed for the cyclically heat treated specimens. The fluctuating behavior noted in the resistivity at long aging times is not present for these measurements, giving further evidence to the claim that the secondary precipitate size population is responsible for this fluctuating behavior in

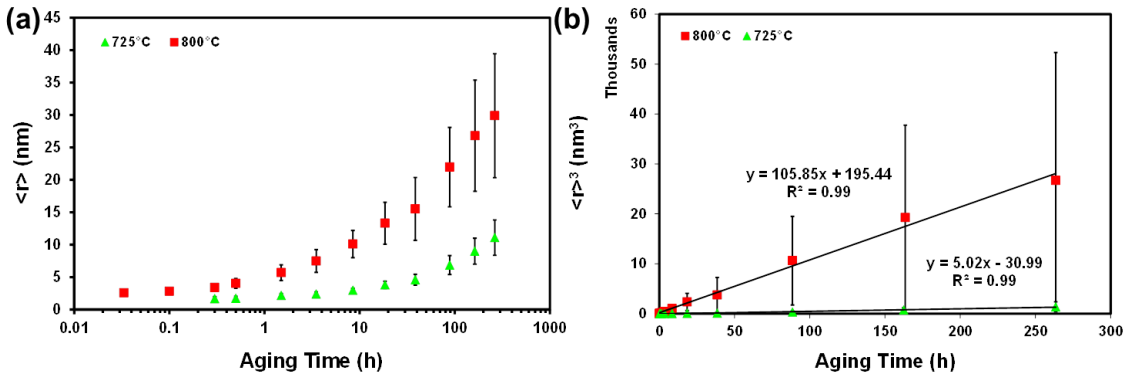

Figure 46: Evolution in the precipitate radii for Waspaloy specimens non-cyclically heat treated at 725°C and 800°C. The data is presented as (a) the average precipitate radius with aging time and (b) the coarsening plots. [11]

the cyclically heat treated Waspaloy specimens. In the next section, the electrical response from Figure 47 will be fit using a revised compositional modeling term.

9.4 Improvements to Compositional Modeling Term

Equation 16 from the previous chapter assumed a parabolic behavior for the electrical response of the matrix phase in Waspaloy. While this might be accurate for a binary alloy, Waspaloy is a much more complex system with over ten different alloying elements. It is therefore proposed that a more generic form of η_c be used to model the compositional effects on the electrical response. This improved formula is given by equation 18.

$$\eta_c = -C f_{V,T}^{n} \tag{18}$$

Equation 18 has two positive, non-zero fitting constants - C and n. This new η_c still has the same generic decrease with increasing volume fraction; however, it is not constrained to have a parabolic decrease, as was the case for equation 16. Similarly to the previous model, C and n should be fit to the data at each aging temperature due to the variations in the partitioning ratios as temperature is changed.

The model for the entire electrical response (η') can also be improved by normalizing the term in equation 17 by its maximum value (η_{max}) to yield a unitless value. Positive η'

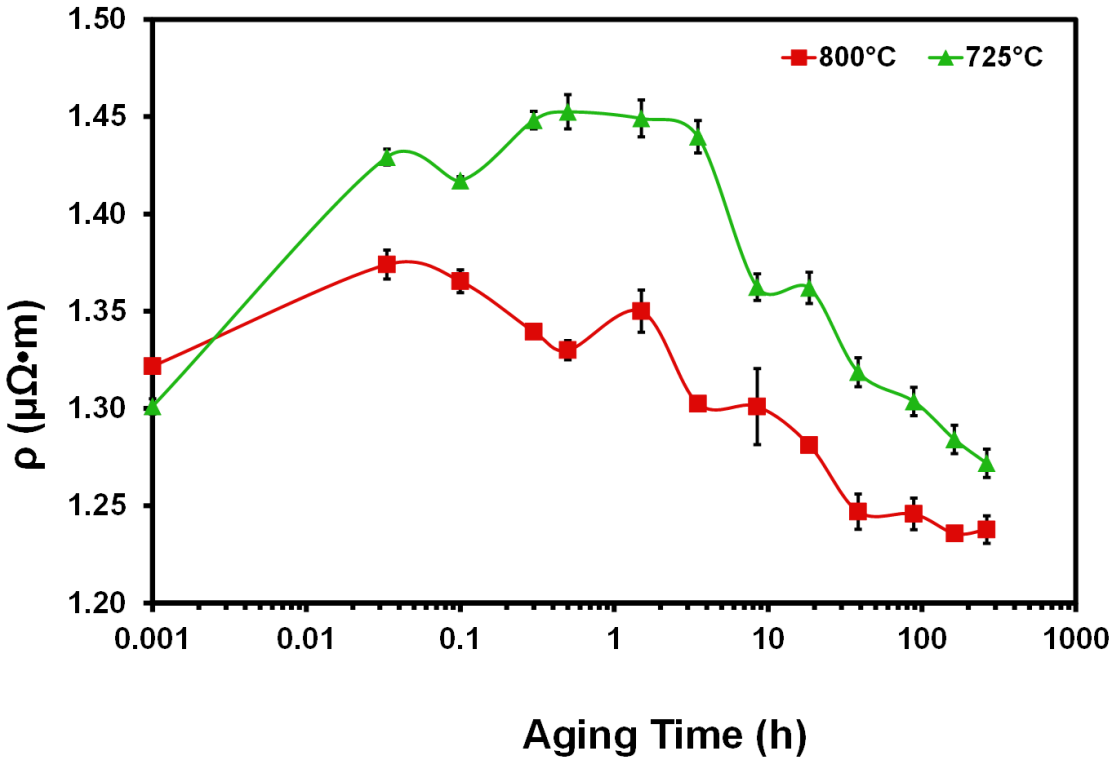

Figure 47: Electrical resistivity for Waspaloy specimens non-cyclically heat treated at 725°C and 800°C. The data points located at 0.001h represent the solution treated specimens.[11]

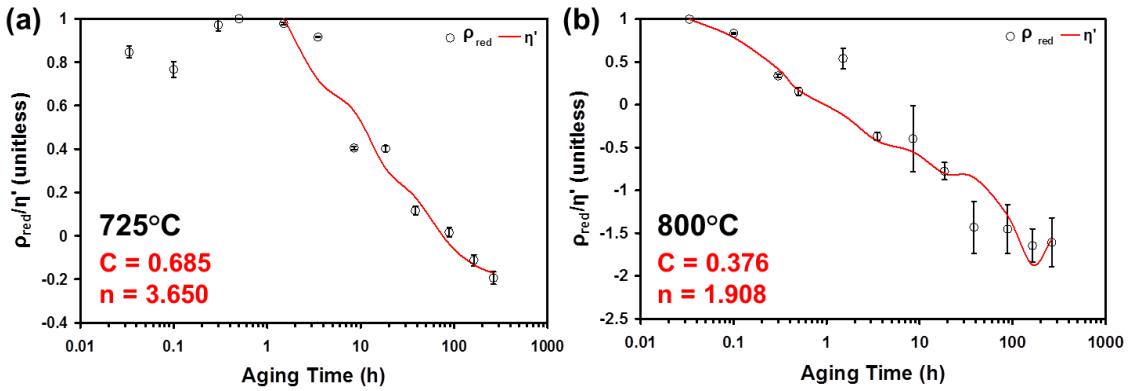

Figure 48: Reduced resistivity with η' fits for Waspaloy specimens non-cyclically heat treated at (a) 725°C and (b) 800°C. The excellent fit of this microstructural model to the measured electrical response indicates the model's validity. Modified from [11]

values would indicate that η_g is the dominant term, whereas negative values would indicate that η_c is the dominant term. This improved η' is given by equation 19.

$$\eta' = \frac{\eta_g + \eta_c}{|\eta_{max}|} = \frac{3.33 \sum \left(\frac{f_V^{4/3}}{\langle r \rangle^2} \right) - C f_{V,T}^n}{|\eta_{max}|} \tag{19}$$

The electrical resistivity shown in Figure 47 was fit with the η' microstructural model, given by equation 19, and is displayed in Figure 48. The data is presented as a fit to the relative resistivity given by equation 9 in Chapter 7, allowing for the resistivity and η' values to be plotted on the same axis. The fitted η' model shows excellent agreement with the measured electrical resistivity for both aging temperatures. With the exception of the outlier located at 1.5h of aging at 800°C, the η' fit lies very closely to the measured data points in all cases. There is a noticeably larger standard deviation in the electrical resistivity at this data point, which may account for the discrepancy. The good fit of this microstructural model to the measured response implies that this model is a good indicator of the effects of the γ' microstructure on the conduction electron scattering ability of the bulk Waspaloy specimens. In the next section, η' will be further revised to account for the finite size and distribution of the precipitates.

9.5 Improvements to Geometric Modeling Term

The η' model used in the previous section has shown an excellent fit to the measured electrical resistivities of Waspaloy specimens; however, the underlying assumptions for this model are not an exact representation of the true Waspaloy microstructure. Specifically, the γ' precipitates have a finite size; therefore, the assumption that the precipitates are point particles is not accurate. The assumption that the precipitates all have the same size is also inaccurate, as there is a distribution of precipitates in the microstructure. This section presents an updated η_g model that more accurately reflects the true γ' microstructure in Waspaloy.

Since the γ' precipitates have a finite size, the location of a new precipitate is dependent on the locations of all the other precipitates. This in turn makes the formula for the nearest neighbor distance of point particles to be an inaccurate representation of the actual nearest neighbor distances. Instead, the mean free path between precipitates (λ) is a more accurate representation of the true microstructure, as the finite size of the particles is accounted for [88, 89]. The variable, λ, can thus replace the nearest neighbor distance, Δ, used in equation 13. The mean free path is defined by equation 20.

$$\lambda \equiv \frac{4(1 - f_V)}{S_V} \tag{20}$$

The precipitates also have a distribution of precipitate sizes. Since the smallest precipitates are expected to be the most effective at scattering conduction electrons, the precipitates having much smaller diameters than the average size should have a greater contribution to the resistivity than those of average size or larger. Modeling with the entire distribution of precipitates is thus important towards accurately describing the effects of the precipitate microstructure on the electrical response of superalloys.

For a distribution of precipitates, S_V and f_V are given by equations 21 and 22 respectively. Equation 21 can be compared to the original formulation for S_V, given by equation 15. For a distribution of particles, the average second moment of the radius ($\langle r^2 \rangle$) is not

equal to the average first moment of the radius squared ($\langle r \rangle^2$). Similar logic applies to the average third moment of the radius in equation 22.

$$S_V = 4\pi N_V \left\langle r^2 \right\rangle \tag{21}$$

$$f_V = \frac{4}{3}\pi N_V \left\langle r^3 \right\rangle \tag{22}$$

Inserting equations 20 - 22 into the original equation for η_g (equation 13) yields equation 23.

$$\eta_g = \frac{S_V}{\lambda} = \sum \frac{9 f_V^2}{4(1 - f_V)} \left(\frac{\langle r^2 \rangle}{\langle r^3 \rangle} \right)^2 \tag{23}$$

The new η' model that reflects the entire distribution of precipitates is given by equation 24. The microstructural information used for fitting in the previous section (along with the average second and third moments of the radius) was refit to the measured resistivity using this improved η'. The resistivity and η' fits are shown in Figure 49. The η' model again shows an excellent fit to the measured electrical data. The 725°C sample set shows a difference from the measured response between 3.5h and 8.5h. This is in a region where the resistivity steeply declines. It is believed that the lack of data between 3.5h and 8.5h made it difficult to fit the resistivity in this region. If additional aging times were measured between 3.5h and 8.5h, then a smoother trend could be obtained.

$$\eta' = \frac{\eta_g + \eta_c}{|\eta_{max}|} = \frac{\sum \frac{9 f_V^2}{4(1-f_V)} \left(\frac{\langle r^2 \rangle}{\langle r^3 \rangle} \right)^2 - C f_{V,T}^n}{|\eta_{max}|} \tag{24}$$

The C values from the η' model decreased for both aging temperatures, when fit with a distribution of precipitates. The n values also decreased somewhat, but not to the extent that C decreased. Since the formula for η_g is drastically different for the distribution of precipitates, it is expected that the fitting coefficients for η_c would also change. Since the fits to the measured data remain good, the η' model shows promise for relating volume distributions of the γ' phase in Waspaloy to the measured electrical response.

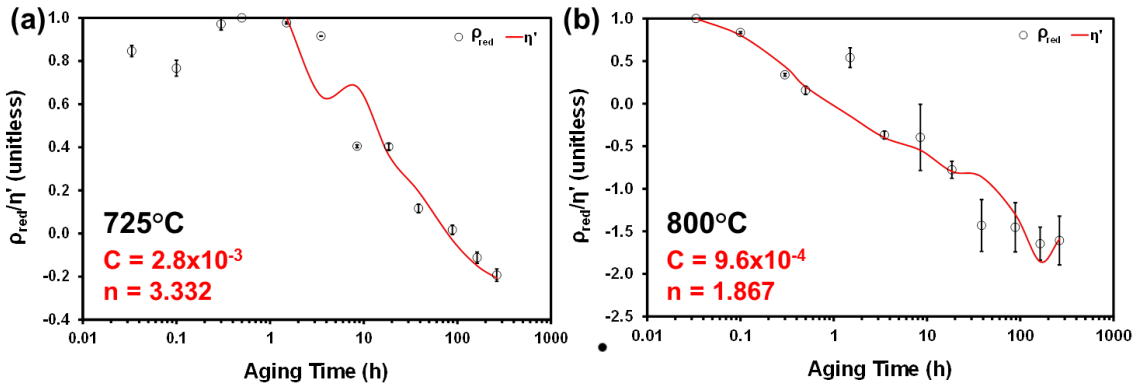

Figure 49: Reduced resistivity with η' fits (using a distribution of precipitates) for Waspaloy specimens non-cyclically heat treated at (a) 725°C and (b) 800°C. The excellent fit of this microstructural model to the measured electrical response indicates the model's validity.

9.6 Conclusions

The use of non-cyclic heat treatment resulted in a single precipitate size population - in contrast to the bimodal distributions noted for cyclic heat treatment. The precipitate radii from this distribution increased smoothly with both time and temperature. The precipitates were determined to be in the diffusion controlled coarsening regime for heat treatment at 800°C and a mixed mode of growth and coarsening at 725°C. The microstructural evolution in the non-cyclically heat treated specimens is the same as that observed for the primary precipitate size population due to cyclic heat treatment at these same aging temperatures. The single precipitate size population from the individual time-temperature heat treatments resulted in smoother resistivity trends with aging time than those noted for the bimodal distributions of precipitates. Specifically, the electrical response does not show the fluctuating behavior with aging time noted for cyclically heat treated Waspaloy.

The microstructural model designed to correlate the electrical response of Waspaloy due to precipitation (η') has been improved such that the resistivity of the matrix phase is not required to be parabolic with increases in the precipitate volume fraction. In addition, the model was further improved to include the effects of finite precipitate sizes and a volume distribution of the precipitates. These changes make η' a good descriptor of the true precipitate microstructure. In order to expand this model to accurately reflect gas turbine engine components, the evolving dislocation density must also be accounted for. Dislocations are

also effective conduction electron scatterers, and the dislocation density will change with thermomechanical exposure in the gas turbine engine. At this time, the η' model does not reflect this microstructural parameter; however, for the case of Waspaloy specimens heat treated without loading, the η' model shows an excellent fit to the measured electrical response.

CHAPTER 10

CONCLUSIONS AND FUTURE WORK

10.1 Conclusions

Small angle scattering (SAS) has proven to be an accurate method to obtain volume distributions of γ' phase in heat treated Waspaloy. Both ultra small angle X-ray scattering (USAXS) and small angle neutron scattering (SANS) have been shown as an effective means to characterize this microstructure; however, the type of radiation used (X-rays versus neutrons) has some impact on the details of the obtainable microstructural data. The USAXS data displayed a Debye scattering region for the γ' precipitates, whereas the SANS data displayed correlation peaks. These correlation peaks arise from interparticle scattering, which is more probable as the thickness of the sample increases. The SANS specimens were approximately 2mm thick, as compared to the 10-20μm thick USAXS specimens. This scattering region difference allows for the precipitate coordination number and correlation distance (center-to-center distance) to be obtained for the SANS measurements, in addition to the fitted volume distribution. The Debye regions in the USAXS data cannot be fit with these two microstructural parameters. The major difference between the USAXS and SANS data is that the USAXS measurements were more sensitive to the presence of a secondary precipitate size population formed upon cyclic heat treatment. The SANS data did not display this secondary population, making SANS ill-suited for characterizing the cyclically heat treated specimens. For specimens exposed to non-cyclic heat treatment, no secondary populations were formed. Since thicker specimens may be used for SANS measurements, this makes SANS measurements better-suited than USAXS measurements for the non-cyclically heat treated specimens, due to increased statistical significance.

The majority of the SAS specimens were given ex-situ heat treatments, followed by a brine quench. A study was conducted to ascertain the errors associated with this type of heat treatment by comparing ex-situ versus in-situ heat treatment for SANS specimens

aged for short aging times. It was found that the microstructural data was very similar for both cases, implying that the effects of quenching to room temperature were negligible for the heat treatment conditions used in these studies. The only significant difference in the data involved the temporal power law functions describing the increase in the precipitate radius with aging time. For the in-situ case, two distinct rate laws were evidenced from the SANS data, but for the ex-situ case, the two rate laws were less distinct and displayed slightly lower values. The larger number of data points for the in-situ case allowed for the smoother data trends. It is therefore important to measure a large number of aging times for the initial stages of aging, where the rate law is quickly evolving with time, so that smooth trends in the power law function can be obtained.

Four-point probe electrical resistivity testing has also shown sensitivity to the microstructural evolution of the precipitates in Waspaloy. The resistivity shows a fast increase to a maximum due to the increasing conduction electron scattering from the initially nucleated precipitates. As the precipitate mean free path increases due to growth and coarsening, the scattering power of the precipitate phase begins to decrease. Also, as the volume fraction of precipitates increases, precipitate forming solute is removed from the matrix phase, resulting in a less resistive system. After the initial resistivity maximum, there is a slower decrease resulting from both growth/coarsening and solute removal. When the precipitates reach their equilibrium volume fraction, the resistivity shows a plateau that occurs at similar aging times to the maximum in hardness.

The initial resistivity maximum can be modeled with a Johnson-Mehl-Avrami (JMA) type equation. These JMA fits showed an excellent agreement with the measured electrical response for Waspaloy specimens exposed to aging temperatures between 600°C and 650°C. From this fitting, an activation energy of 398 kJ/mol was calculated for the nucleation of γ' in Waspaloy. The height of the initial maximum has often been attributed to the volume fraction of the initially nucleated zones. The relative volume fraction and resistivity increased similarly with aging time; however, the relative volume fraction was less than the relative resistivity throughout all measured aging times - implying that the volume fraction dependence is not one-to-one. Modeling the resistivity maximum is useful towards

non-destructively characterizing the precipitate microstructure during the initial processing stages of gas turbine engine components.

Resistivity can also be used to track the precipitation process past the initial maximum, where the growth and coarsening regimes become dominant. For these studies both cyclic and non-cyclic heat treatment schedules were used. The specimens exposed to cyclic heat treatment showed a secondary precipitate size population in addition to the larger primary distribution. The primary precipitate radii increased progressively with both aging time and temperature, as would be expected. It was determined that the primary γ' precipitates were in the coarsening stage upon heat treatment at 800°C and 875°C. A mixed mode of growth and coarsening was noted upon heat treatment at 725°C. The secondary precipitate size population did not increase progressively with time and temperature. Instead the secondary precipitates fluctuated in and out of solution, with the secondary volume fraction being independent of the aging temperature. This fluctuating volume fraction resulted in corresponding fluctuations in the resistivity data at long aging times. It was determined that the cyclic heat treatment was the cause of the secondary precipitate population. Upon non-cyclic heat treatment, no secondary precipitate size population was evidenced, resulting in smoother resistivity trends with aging time. The single precipitate size population due to non-cyclic heat treatment showed a progressive increase in the radius with time and temperature, similarly to the primary population for cyclically heat treated specimens. Also in accordance with this primary population, the specimens non-cyclically heat treated at 800°C were determined to be in the coarsening regime, and the specimens heat treated at 725°C displayed a mixed mode of growth and coarsening.

A microstructural model (η'), based on microstructural parameters obtained from SAS measurements, was updated to relate the microstructural evolution during the growth and coarsening regimes to the non-destructive electrical response. The updated model accounts for conduction electron scattering from both precipitates and solute atoms as the microstructure evolves with heat treatment. The initial model only accounted for conduction electron scattering from precipitates, causing an inaccurate fit to the resistivity data at long aging times (where solute removal is significant). By including the effects of the matrix solute

content on the electrical response model, more accurate fits were obtained. The accuracy of the fitted data was also improved by removing the constraint that the resistivity of the matrix be parabolic with composition. The final η' model was further enhanced by fitting the entire volume distribution of precipitates to the electrical response - as opposed to just using the average size of the precipitates. This final model has shown excellent fits to the true electrical response due to γ' growth and coarsening in Waspaloy, implying that this model is valid for quantifying the microstructure's effects on the electrical resistivity. It is believed that some form of this model could be used to non-destructively monitor the precipitate phases in nickel-base superalloys. This would allow for gas turbine engine components to be non-destructively tested during service, perhaps leading to better lifetime prediction.

10.2 Suggested Future Work

The η' model does not account for the evolution in dislocation density with heat treatment. In order for this model to be used for in-service gas turbine engine components, this microstructural parameter must be accounted for. During service, these components will be exposed to large stresses, in addition to the thermal exposure described in this project. Specimens with long exposure times can also develop coherency strains at the precipitate matrix interface. Such coherency strains are not expected for Waspaloy, which has a near zero or negative lattice mismatch, but coherency strains would be expected for many of the other commercially available nickel-base superalloys. Both the thermomechanical treatment and the coherency strains should give rise to an increase in the dislocation density. This would in turn cause the electrical resistivity to increase. If the strain and dislocation density were obtained as a function of thermomechanical heat treatment, then this microstructural parameter could in turn be related to the electrical response. The addition of a strain term to the η' model would make this model sensitive to the major evolving microstructural parameters that would affect both the electrical resistivity and the mechanical properties of nickel-base superalloys.

For this project, the precipitates were assumed to be spherical in all cases. For Waspaloy, this is a good assumption, since the low lattice mismatch acts to prevent morphology changes. For newer superalloy compositions, the precipitates often progress to cuboids, arrays of cuboids, and even solid state dendrites. This change in morphology would require the η' model to be modified, as the surface area of the precipitates was assumed to be that of a sphere. A study should be performed to ascertain the effects of morphology changes on the electrical response, such that the η' model could apply to all of the expected γ' morphologies in superalloys with different compositions and volume fractions.

APPENDIX A

HARDNESS IN THE OVER-AGED REGIME

The mechanical response of nickel-base superalloys due to the evolving precipitate microstructure has been the subject of extensive studies. In fact, models already exist to describe the increase in hardness or strength in superalloys due to the most relevant microstructural information, such as precipitate size, mean free path, and volume fraction [1]. This appendix is meant to present a particular model for the mechanical properties of superalloys in the over-aged regime. The model presented in this appendix can be used to predict the decrease in hardness (or strength) of nickel-base superalloys due to coarsening in the over-aged regime and was calculated by Wilson [90] for a precipitation hardened iron alloy.

The equation for the extent of decrease in the hardness (H) as a function of aging time (t) is given by equation 25. In equation 25, ΔH, ΔH_0, and t_0 are the increase in hardness from the solution treated specimen, the hardness increase at the maximum in hardness, and the time to reach the hardness maximum respectively. The variable M is a constant, representing the slope of the left-hand side of equation 25 plotted against the change in time from the hardness maximum.

$$\left(\frac{1}{\Delta H}\right)^3 - \left(\frac{1}{\Delta H_0}\right)^3 = M(t - t_0) \tag{25}$$

The assumptions required for the derivation of equation 25, as given by Wilson [90], are as follows. Orowan bowing was assumed to be the primary mode of dislocation motion, and the precipitate phase was assumed to have reached its equilibrium volume fraction. Since equation 25 is only meant to model the mechanical behavior past the hardness peak, both of these assumptions are reasonable. The precipitates were also assumed to be spherical, which is not necessarily the case for all nickel-base superalloy specimens [37]; however, the precipitates formed for the Waspaloy specimens used in this project were predominantly

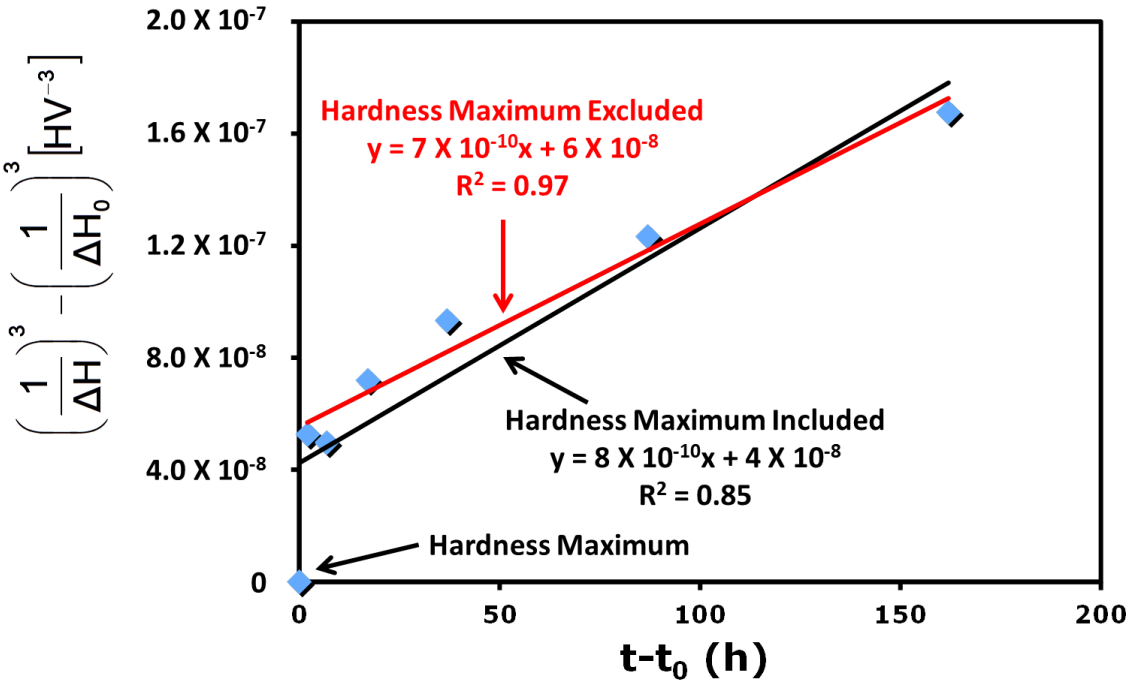

Figure 50: The decrease in hardness as a function of time for over-aged Waspaloy samples heat treated at 875°C. The data are fit via linear least squares regression including the hardness maximum and excluding the hardness maximum. It is clear that the linearity increases past the hardness maximum. [8]

spherical. Finally, the precipitate radii were assumed to obey a $t^{1/3}$ temporal power law, as would be expected due to diffusion controlled coarsening. This is again a reasonable assumption for times past the peak in hardness.

A plot of the left hand side of equation 25 versus the change in time from the peak is given by Figure 50. The data used in Figure 50 is from hardness measurements on Waspaloy specimens heat treated at 875°C for times past the peak in hardness. The hardness values as a function of the aging time were presented in Figure 25 in Chapter 6. It is apparent that the hardness value corresponding to the maximum does not form a linear trend with the rest of the over-aged data. Equation 25 forces this value to reside at the origin, which does not agree with the remainder of the data. As can be seen by Figure 50, not using the maximum in hardness results in a better linear fit to the data.

Past the hardness maximum, the data agrees with equation 25, as can be seen by the R^2 value corresponding to the linear fit changing from 0.85 to 0.97 past the peak in hardness. It

is possible that the Waspaloy specimens were not in the true steady state coarsening regime at the hardness maximum, which may account for the discrepancy in the data point's location. For aging times well past the peak in hardness, Figure 50 suggests that equation 25 may be used to model the decrease in the Vickers microhardness with aging time for Waspaloy specimens.

References

[1] Reed, R. C., *The Superalloys: Fundamentals and Applications*. Cambridge: Cambridge University Press, 2008.

[2] White, R. J., Fisher, S. B., Miller, K. M., and Swallow, G. A., "Resistometric Study of Aging in Nimonic Alloys (I). PE16," *Journal of Nuclear Materials*, vol. 52, no. 1, pp. 51–58, 1974.

[3] Rosen, G. I., Dirnfeld, S. F., Bamberger, M., and Prinz, B., "In-Situ Electrical Resistivity Measurements for Determining Formation Kinetics of the γ' Phase in Nickel-Based Wrought Superalloys," *Zeitschrift fuer Metallkunde*, vol. 85, no. 2, pp. 127–130, 1994.

[4] Roebuck, B., Cox, D., and Reed, R., "The Temperature Dependence of Volume Fraction in a Ni-Based Single Crystal Superalloy from Resistivity Measurements," *Scripta Materialia*, vol. 44, no. 6, pp. 917–921, 2001.

[5] Kelekanjeri, V. S. K. G. and Gerhardt, R. A., "Electrical Characterization of Aged Waspaloy Microstructures," *Advanced Materials Research*, vol. 15-17, pp. 876–881, 2007.

[6] Kelekanjeri, V. S. K. G. and Gerhardt, R. A., "Etch Pit and γ' Precipitate Evolution in Controlled Waspaloy Microstructures Aged at 725, 800 and 875°C," *Acta Materialia*, vol. 57, no. 2, pp. 616–627, 2009.

[7] Kelekanjeri, V. S. K. G., Moss, L. K., Gerhardt, R. A., and Ilavsky, J., "Quantification of the Coarsening Kinetics of γ' Precipitates in Waspaloy Microstructures with Different Prior Homogenizing Treatments," *Acta Materialia*, vol. 57, no. 16, pp. 4658–4670, 2009.

[8] Whelchel, R. L., Kelekanjeri, V. S. K. G., and Gerhardt, R. A., "Mechanical and Electrical Characterisation in Age Hardened Waspaloy Microstructures," *International Heat Treatment and Surface Engineering*, vol. 3, no. 1-2, pp. 35–39, 2009.

[9] Whelchel, R. L., Kelekanjeri, V. S. K. G., Gerhardt, R. A., and Ilavsky, J., "Effect of Aging Treatment on the Microstructure and Resistivity of a Nickel Base Superalloy," *Metallurgical and Materials Transactions A*, vol. 42, no. 5, pp. 1362–1372, 2011.

[10] Whelchel, R. L., Kelekanjeri, V. S. K. G., Gerhardt, R. A., Ilavsky, J., and Littrell, K. C., "Correlating Small Angle Scattering Spectra to Electrical Resistivity Changes in a Nickel-Base Superalloy," in *Materials Research Society Spring Meeting*, (San Francisco, CA), p. W10.5, 2010.

[11] Whelchel, R. L., Gerhardt, R. A., and Littrell, K. C., "Structure-Property Relationships in Waspaloy via Small Angle Scattering and Electrical Resistivity Measurements," in *7th International Symposium on Superalloy 718 and Derivatives*, (Pittsburgh, PA), p. 34715, 2010.

[12] Kasap, S. O., *Principles of Electronic Materials and Devices*. Boston: McGraw-Hill, 2nd ed., 2002.

[13] Zrnik, J., Strunz, P., Hornak, P., Vrchovinsky, V., and Wiedenmann, A., "Microstructural Changes in Long-Time Thermally Exposed Ni-Base Superalloy Studied by SANS," *Applied Physics A*, vol. 74, pp. S1155–S1157, 2002.

[14] Mukherji, D., Del Genovese, D., Strunz, P., Gilles, R., Wiedenmann, A., and Rosler, J., "Microstructural Characterisation of a Ni-Fe-Based Superalloy by In Situ Small-Angle Neutron Scattering Measurements," *Journal of Physics: Condensed Matter*, vol. 20, pp. 104220–104228, 2008.

[15] Mukherji, D., Gilles, R., Strunz, P., Lieske, S., Wiedenmann, A., and Wahi, R. P., "Measurement of γ' Precipitate Morphology by Small Angle Neutron Scattering," *Scripta Materialia*, vol. 41, no. 1, pp. 31–38, 1999.

[16] Ratel, N., Bruno, G., and Deme, B., "In Situ Small-Angle Neutron Scattering Investigation of the γ' Precipitation and Growth in the Nickel-Based Single-Crystal Alloy SC16," *Journal of Physics-Condensed Matter*, vol. 17, no. 43, pp. 7061–7075, 2005.

[17] Ratel, N., Deme, B., Bastle, P., and Caron, P., "In Situ SANS Investigation of the Kinetics of Rafting of γ' Precipitates in a Fourth-Generation Single-Crystal Nickel-Based Superalloy," *Scripta Materialia*, vol. 59, no. 11, pp. 1167–1170, 2008.

[18] Sundararaman, M., Chen, W., Wahi, R. P., Wiedenmann, A., Wagner, W., and Petry, W., "TEM and SANS Investigation of Age Hardened Nimonic PE16 after Cyclic Loading at Room-Temperature," *Acta Metallurgica Et Materialia*, vol. 40, no. 5, pp. 1023–1028, 1992.

[19] Strunz, P., Gilles, R., Mukherji, D., Hofmann, M., del Genovese, D., Roesler, J., Hoelzel, M., and Davydov, V., "Dependence of Small-Angle Neutron Scattering Contrast on the Difference in Thermal Expansions of Phases in Two-Phase Alloys," *Journal of Applied Crystallography*, vol. 42, pp. 981–989, 2009.

[20] Strunz, P., Mukherji, D., Gilles, R., Wiedenmann, A., and Fuess, H., "Determination of γ' Solution Temperature in Re-Rich Ni-Base Superalloy by Small-Angle Neutron Scattering," *Journal of Applied Crystallography*, vol. 34, pp. 541–548, 2001.

[21] Huang, E. W., Liaw, P. K., Porcar, L., Liu, Y., Liu, Y. L., Kai, J. J., and Chen, W. R., "Study of Nanoprecipitates in a Nickel-Based Superalloy using Small-Angle Neutron Scattering and Transmission Electron Microscopy," *Applied Physics Letters*, vol. 93, no. 16, pp. 161904–1 – 161904–3, 2008.

[22] Tian, B., Paris, O., Zickler, G. A., Lind, C., Wasle, G., and May, R. P., "SANS Investigation of Phase Separation in Hot-Deformed Nimonic 80a," *Scripta Materialia*, vol. 47, no. 1, pp. 25–30, 2002.

[23] Brass, A. M. and Chene, J., "SANS Analysis of γ' Precipitation in the γ Matrix of Ni Base Superalloy Single Crystals," *Scripta Materialia*, vol. 43, no. 10, pp. 913–918, 2000.

[24] Veron, M. and Bastie, P., "Strain Induced Directional Coarsening in Nickel Based Superalloys: Investigation on Kinetics using the Small Angle Neutron Scattering (SANS) Technique," *Acta Materialia*, vol. 45, no. 8, pp. 3277–3282, 1997.

[25] Rogante, M. and Lebedev, V. T., "Small Angle Neutron Scattering Comparative Investigation of Inconel 738 Samples Submitted to Different Ageing Treatments," *Materials & Design*, vol. 29, no. 5, pp. 1060–1065, 2008.

[26] Zhao, S. Q., Xie, X. S., Smith, G. D., and Patel, S. J., "Gamma Prime Coarsening and Age-Hardening Behaviors in a New Nickel Base Superalloy," *Materials Letters*, vol. 58, no. 11, pp. 1784–1787, 2004.

[27] Bley, F., Livet, F., Lyon, O., and Okuda, H., "An Anomalous Small-Angle X-ray Scattering Study on Phase Decomposition in a Model Superalloy NiCrAl," *Journal of Applied Crystallography*, vol. 30, pp. 914–917, 1997.

[28] Roe, R. J., *Methods of X-ray and Neutron Scattering in Polymer Science*. New York: Oxford University Press, 2000.

[29] Kriege, O. H. and Baris, J. M., "Chemical Partitioning of Elements in Gamma Prime Separated from Precipitation-Hardened, High-Temperature Nickel-Base Alloys," *ASM Transactions Quarterly*, vol. 62, no. 1, pp. 195–200, 1969.

[30] Kriege, O. H. and Sullivan, C. P., "Separation of Gamma Prime from Udimet 700," *ASM Transactions Quarterly*, vol. 61, no. 2, pp. 278–282, 1968.

[31] Porter, D. A. and Easterling, K. E., *Phase Transformations in Metals and Alloys*. New York: Van Nostrand Reinhold, 1981.

[32] Johnson, W. A. and Mehl, R. F., "Reaction Kinetics in Processes of Nucleation and Growth," *Transactions of the American Institute of Mining and Metallurgical Engineers*, vol. 135, pp. 416–442, 1939.

[33] Avrami, M., "Kinetics of Phase Change I - General Theory," *Journal of Chemical Physics*, vol. 7, no. 12, pp. 1103–1112, 1939.

[34] Lifshitz, I. M. and Slyozov, V. V., "The Kinetics of Precipitation from Supersaturated Solid Solutions," *Journal of Physics and Chemistry of Solids*, vol. 19, no. 1-2, pp. 35–50, 1961.

[35] Wagner, C., "Theorie der Alterung von Niederschlagen Durch Umlosen (Ostwald-Reifung)," *Z. Electrochem.*, vol. 65, pp. 581–591, 1961.

[36] Ardell, A. J. and Nicholson, R. B., "The Coarsening of γ' in Ni-Al Alloys," *Journal of the Physics and Chemistry of Solids*, vol. 27, no. 11-12, pp. 1793–1804, 1966.

[37] Ricks, R. A., Porter, A. J., and Ecob, R. C., "The Growth of γ' Precipitates in Nickel-Base Superalloys," *Acta Metallurgica*, vol. 31, no. 1, pp. 43–53, 1983.

[38] Gilles, R., Mukherji, D., Del Genovese, D., Strunz, P., Barbier, B., Kockelmann, W., Rosler, J., and Fuess, H., "Misfit Investigations of Nickel-Base Superalloys," *Materials Science Forum*, vol. 426-432, pp. 821–826, 2003.

[39] Royer, A., Jacques, A., Bastie, P., and Veron, M., "The Evolution of the Lattice Parameter Mismatch of Nickel Based Superalloys: An In Situ Study during Creep Deformation," *Materials Science and Engineering A*, vol. 319-321, pp. 800–804, 2001.

[40] Rastogi, P. K. and Ardell, A. J., "Coarsening Behavior of the γ' Precipitate in Nickel-Silicon Alloys," *Acta Metallurgica*, vol. 19, no. 4, pp. 321–330, 1971.

[41] Ardell, A. J., "An Application of Theory of Particle Coarsening: the γ' Precipitate in Ni-Al Alloys," *Acta Metallurgica*, vol. 16, no. 4, pp. 511–516, 1968.

[42] Ardell, A. J., Nicholson, R. B., and Eshelby, J. D., "On Modulated Structure of Aged Ni-Al Alloys," *Acta Metallurgica*, vol. 14, no. 10, pp. 1295–1309, 1966.

[43] Kim, H. T., Chun, S. S., Yao, X. X., Fang, Y., and Choi, J., "Gamma Prime (γ') Precipitating and Ageing Behaviours in Two Newly Developed Nickel-Base Superalloys," *Journal of Materials Science*, vol. 32, no. 18, pp. 4917–4923, 1997.

[44] Dwarapureddy, A. K., Balikci, E., Ibekwe, S., and Raman, A., "Activation Energy for Growth in Single Size Distribution and the Dissolution Features of γ' Precipitates in the Superalloy IN738LC," *Journal of Materials Science*, vol. 43, no. 6, pp. 1802–1810, 2008.

[45] Stevens, R. A. and Flewitt, P. E. J., "Effects of γ' Precipitate Coarsening during Isothermal Aging and Creep of the Nickel-Base Superalloy IN738," *Materials Science and Engineering*, vol. 37, no. 3, pp. 237–247, 1979.

[46] Baldan, A., "Review Progress in Ostwald Ripening Theories and their Applications to Nickel-Base Superalloys - Part I: Ostwald Ripening Theories," *Journal of Materials Science*, vol. 37, no. 11, pp. 2171–2202, 2002.

[47] Baldan, A., "Review Progress in Ostwald Ripening Theories and their Applications to the γ' Precipitates in Nickel-Base Superalloys - Part II: Nickel-Base Superalloys," *Journal of Materials Science*, vol. 37, no. 12, pp. 2379–2405, 2002.

[48] Ardell, A. J., "Effect of Volume Fraction on Particle Coarsening - Theoretical Considerations," *Acta Metallurgica*, vol. 20, no. 1, pp. 61–71, 1972.

[49] Voorhees, P. W. and Glicksman, M. E., "Solution to the Multi-Particle Diffusion Problem with Applications to Ostwald Ripening -I. Theory," *Acta Metallurgica*, vol. 32, no. 11, pp. 2001–2011, 1984.

[50] Voorhees, P. W. and Glicksman, M. E., "Solution to the Multi-Particle Diffusion Problem with Applications to Ostwald Ripening -II. Computer Simulations," *Acta Metallurgica*, vol. 32, no. 11, pp. 2013–2030, 1984.

[51] Thornton, K., Akaiwa, N., and Voorhees, P., "Large-Scale Simulations of Ostwald Ripening in Elastically Stressed Solids. I. Development of Microstructure," *Acta Materialia*, vol. 52, no. 5, pp. 1353 – 1364, 2004.

[52] Thornton, K., Akaiwa, N., and Voorhees, P., "Large-Scale Simulations of Ostwald Ripening in Elastically Stressed Solids. II. Coarsening Kinetics and Particle Size Distribution," *Acta Materialia*, vol. 52, no. 5, pp. 1365 – 1378, 2004.

[53] Panseri, C. and Federighi, T., "A Resistometric Study of Pre-Precipitation in Al-10% Zn," *Acta Metallurgica*, vol. 8, no. 4, pp. 217–238, 1960.

[54] Herman, H., Fine, M. E., and Cohen, J. B., "Formation and Reversion of Guinier-Preston Zones in Al-5.3 at.% Zn," *Acta Metallurgica*, vol. 11, no. 1, pp. 43–56, 1963.

[55] Wilkes, P., "Formation of Guinier-Preston Zones in Cu-Be Alloys," *Acta Metallurgica*, vol. 16, no. 2, pp. 153–158, 1968.

[56] Wilson, F. G. and Pickering, F. B., "A Study of Zone Formation in an Austenitic Steel Containing 4% Titanium," *Acta Metallurgica*, vol. 16, no. 1, pp. 115–131, 1968.

[57] Silcock, J., "Resistance Changes in Iron-Base Alloys forming Ni_3(Al, Ti) Precipitates," *Metal Science Journal*, vol. 5, pp. 182–190, 1971.

[58] Oettel, W., Radomsky, C., and Loffler, H., "Information Gain from Analytical Description of Isothermal Resistivity Curves," *Kristall Und Technik-Crystal Research and Technology*, vol. 15, no. 6, pp. 713–719, 1980.

[59] Lendvai, J., Ungar, T., Kovacs, I., and Groma, G., "Correlation between Resistivity Increment and Volume Fraction of GP Zones in an Al-3.2 wt% Zn-2.2 wt% Mg Alloy," *Philosophical Magazine*, vol. 33, no. 1, pp. 209–212, 1976.

[60] Ferragut, R., Somoza, A., and Torriani, I., "Pre-Precipitation Study in the 7012 Al-Zn-Mg-Cu Alloy by Electrical Resistivity," *Materials Science and Engineering A*, vol. 334, no. 1-2, pp. 1–5, 2002.

[61] Barucca, G., Ferragut, R., Lussana, D., Mengucci, P., Moia, F., and Riontino, G., "Phase Transformations in QE22 Mg Alloy," *Acta Materialia*, vol. 57, no. 15, pp. 4416–4425, 2009.

[62] Shinoda, R., Fawzy, A., Graiss, G., and Saad, G., "Effect of ϵ-Phase Dissolution on Electrical Resistivity of Torsionally Deformed Cu-6 wt% Sn Alloy," *Solid State Communications*, vol. 84, no. 3, pp. 335–339, 1992.

[63] Sato, S., Takahashi, Y., Sanada, T., Wagatsuma, K., and Suzuki, S., "Small-Angle X-ray Scattering Characterization of Precipitates in Cu-Ti Alloys," *Journal of Alloys and Compounds*, vol. 477, no. 1-2, pp. 846–850, 2009.

[64] Truong, C. T., Kabisch, O., Gille, W., and Schmidt, U., "Small Angle X-ray Scattering and Electrical Resistivity Measurements on an Al-2Li-5Mg-0.1Zr Alloy," *Materials Chemistry and Physics*, vol. 73, no. 2-3, pp. 268–273, 2002.

[65] Wen, W., Zhao, Y., and Morris, J. G., "The Effect of Mg Precipitation on the Mechanical Properties of 5XXX Aluminum Alloys," *Materials Science and Engineering A*, vol. 392, no. 1-2, pp. 136–144, 2005.

[66] Popovic, M. and Romhanji, E., "Characterization of Microstructural Changes in an Al-6.8 wt.% Mg Alloy by Electrical Resistivity Measurements," *Materials Science and Engineering A*, vol. 492, no. 1-2, pp. 460–467, 2008.

[67] Janecek, M., Slamova, M., and Hajek, M., "Structural Transformations in Continuously Cast Al-Mg Alloys," *Journal of Alloys and Compounds*, vol. 378, pp. 316–321, 2004.

[68] Vooijs, S., Davenport, B., and Van Der Zwaag, S., "Monitoring the Precipitation Reactions in a Cold Rolled Al-Mn-Mg-Cu Alloy using Thermoelectric Power and Resistivity Measurements," *Philosophical Magazine A*, vol. 81, no. 8, pp. 2059–2072, 2001.

[69] Tilak, R. V. and Morris, J. G., "Studies of the Effect of Thermomechanical Treatments on the Supersaturation Content of Strip-Cast Aluminum Alloy 3004," *Materials Science and Engineering*, vol. 73, no. 1-2, pp. 139–150, 1985.

[70] Marucco, A., "Phase Transformations during Long-Term Ageing of Ni-Fe-Cr Alloys in the Temperature Range 450-600°C," *Materials Science and Engineering A*, vol. A194, no. 2, pp. 225–233, 1995.

[71] Antolovich, S. D. and Jayaraman, N., "Effects of Environment and Structural Stability on the Low Cycle Fatigue Behaviour of Nickel-Base Superalloys," *High Temperature Technology*, vol. 2, pp. 3–13, 1984.

[72] Deschamps, A., Niewczas, M., Bley, F., Brechet, Y., Embury, J. D., Le, S. L., Livet, F., and Simon, J. P., "Low-Temperature Dynamic Precipitation in a Supersaturated Al-Zn-Mg Alloy and Related Strain Hardening," *Philosophical Magazine A*, vol. 79, no. 10, pp. 2485–2504, 1999.

[73] Potton, J. A., Daniell, G. J., and Rainford, B. D., "Particle-Size Distributions from SANS data using the Maximum-Entropy Method," *Journal of Applied Crystallography*, vol. 21, pp. 663–668, 1988.

[74] Ilavsky, J. and Jemian, P. R., "Irena: Tool Suite for Modeling and Analysis of Small Angle Scattering," *Journal of Applied Crystallography*, vol. 42, pp. 347–353, 2009.

[75] Jemian, P. R., Gerhardt, R. A., and Long, G. G., "Anomalous USAXS Investigations of Ni-based Superalloys," *The Annual Report of the Advanced Photon Source at Argonne National Laboratory*, 2002.

[76] Kelekanjeri, V. S. K. G., *Non-Destructive Electrical Characterization of Controlled Waspaloy Microstructures*. PhD thesis, Georgia Institute of Technology, 2007.

[77] "HFIR Sample Environment Equipment." http://neutrons.ornl.gov/instruments/HFIR/sample/equipment.shtml, April 2011.

[78] "Model 6221 AC and DC Current Source." http://www.keithley.com/products/dcac/currentsource/highperfor/?mn=6221, January 2011.

[79] Kelekanjeri, V. S. K. G. and Gerhardt, R. A., "A Closed-Form Solution for the Computation of Geometric Correction Factors for Four-Point Resistivity Measurements on Cylindrical Specimens," *Measurement Science & Technology*, vol. 19, no. 2, pp. 025701–025712, 2008.

[80] Littrell, K. C. and Melnichenko, Y., "General-Purpose Small-Angle Neutron Scattering Diffractometer." http://neutrons.ornl.gov/instruments/HFIR/CG2/, January 2011.

[81] Littrell, K. C. Personal Communication.

[82] "IGOR Pro - Overview." http://www.wavemetrics.com/products/igorpro/igorpro.htm, January 2011.

[83] Ilavsky, J., Jemian, P. R., Allen, A. J., Zhang, F., Levine, L. E., and Long, G. G., "Ultra-Small-Angle X-ray Scattering at the Advanced Photon Source," *Journal of Applied Crystallography*, vol. 42, pp. 469–479, 2009.

[84] Ilavsky, J., Allen, A. J., Long, G. G., and Jemian, P. R., "Effective Pinhole-Collimated Ultra-Small-Angle X-ray Scattering Instrument for Measuring Anisotropic Microstructures," *Review of Scientific Instruments*, vol. 73, no. 3, pp. 1660–1662, 2002.

[85] http://www.materialsdata.com/, January 2011.

[86] Schaffer, J. P., Saxena, A., Antolovich, S. D., Sanders, T. H., and Warner, S. B., *The Science and Design of Engineering Materials*. New York: McGraw-Hill, 1999.

[87] Chandrasekhar, S., "Stochastic Problems in Physics and Astronomy," *Reviews of Modern Physics*, vol. 15, no. 1, pp. 0001–0089, 1943.

[88] Fullman, R. L., "Measurement of Particle Sizes in Opaque Bodies," *Journal of Metals*, vol. 5, no. 3, pp. 447–452, 1953.

[89] Chalkley, H. W., Cornfield, J., and Park, H., "A Method for Estimating Volume-Surface Ratio," *Science*, vol. 110, pp. 295–297, 1949.

[90] Wilson, E. A., "Quantification of Age Hardening in an Fe-12Ni-6Mn Alloy," *Scripta Materialia*, vol. 36, pp. 1179–1185, 1997.